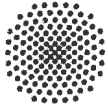# Icing on Unmanned Aerial Vehicles (UAVs)

Numerical simulation of the ice accretion on a propeller of a small fixed-wing UAV

Master's thesis
by
Nicolas Müller

Institute of Aerodynamics and Gas Dynamics
of the University of Stuttgart
&
Department of Engineering Cybernetics
of the Norwegian University of Science and Technology

Stuttgart, November 2020

Universität Stuttgart

Institut für Aerodynamik und Gasdynamik
Direktor: Prof. Dr.-Ing. Ewald Krämer

IAG

Masterarbeit
für Herrn Nicolas Müller
(durchgeführt an der NTNU)

Icing on Unmanned Aerial Vehicles (UAVs)

One of the main limitations of the operational envelope of UAVs today is the risk of atmospheric icing. In contrast to icing in general aviation, UAV icing is not well established and is an emerging research topic.

Ice accretes on the leading-edge airfoils, rotors and propellers where it introduces a severe flow disruption, see Figs.1&2. Studies have shown that ice on rotors and propellers can be responsible for substantial decrease in thrust while increase power requirements. The goal of this thesis is to simulate ice accretion and icing performance penalties on 3D UAV bodies and propellers. The study will use numerical methods (ANSYS FENSAP-ICE) as well as results from experiments. The thesis is to be conducted in English at NTNU in Trondheim, Norway.
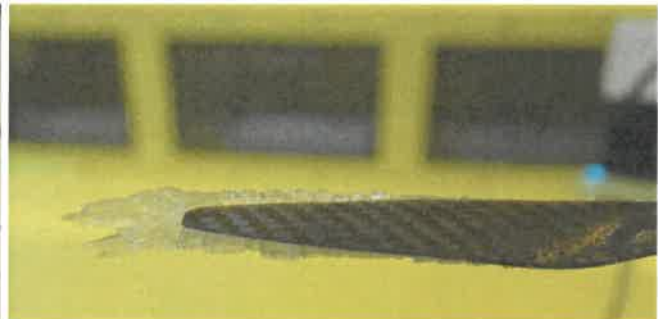
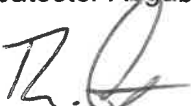Fig. 1: Rime ice on leading edge   Fig. 2: Runback icing on a UAV wing

Tasks:

- Literature search and familiarization on the topic of icing and propeller icing.
- Introduction to the numeric icing tool ANSYS FENSAP-ICE.
- Define a typical UAV propeller geometry.
- Mesh generation for the propeller with Pointwise and Fluent Meshing.
- Validation of performance degradation on a 3D UAV geometry with existing data.
- Find experimental data in the literature that is suitable for validation and compare to FENSAP-ICE.
- CFD simulation of aerodynamic performance penalties on the typical UAV rotor for three meteorological conditions.
- Discussion of results with respect of relevance for UAV operations and upcoming experimental tests.

Die Arbeit wird an der NTNU in Trondheim (Norwegen) durchgeführt.

Betreuer seitens NTNU:	Dipl.-Ing. Richard Hann
Betreuer seitens des IAGs:	Dr.-Ing. Thorsten Lutz
Ausgabetermin:	24.3.2020
Spätester Abgabetermin:	23.9.2020

Dr.-Ing. Thorsten Lutz

Erklärung

Hiermit versichere ich, dass ich diese Masterarbeit selbstständig mit Unterstützung des Betreuers / der Betreuer angefertigt und keine anderen als die angegebenen Quellen und Hilfsmittel verwendet habe. Die Arbeit oder wesentliche Bestandteile davon sind weder an dieser noch an einer anderen Bildungseinrichtung bereits zur Erlangung eines Abschlusses eingereicht worden. Ich erkläre weiterhin, bei der Erstellung der Arbeit die einschlägigen Bestimmungen zum Urheberschutz fremder Beiträge entsprechend den Regeln guter wissenschaftlicher Praxis[1] eingehalten zu haben. Soweit meine Arbeit fremde Beiträge (z.B. Bilder, Zeichnungen, Textpassagen etc.) enthält, habe ich diese Beiträge als solche gekennzeichnet (Zitat, Quellenangabe) und eventuell erforderlich gewordene Zustimmungen der Urheber zur Nutzung dieser Beiträge in meiner Arbeit eingeholt. Mir ist bekannt, dass ich im Falle einer schuldhaften Verletzung dieser Pflichten die daraus entstehenden Konsequenzen zu tragen habe.

_____

Ort, Datum, Unterschrift

Betreuer: **Dr.-Ing. Thorsten Lutz**
Externer Betreuer: **Dr.-Ing. Richard Hann**

_____

[1]Nachzulesen in den DFG-Empfehlungen zur „Sicherung guter wissenschaftlicher Praxis" bzw. in der Satzung der Universität Stuttgart zur „Sicherung der Integrität wissenschaftlicher Praxis und zum Umgang mit Fehlverhalten in der Wissenschaft".

Contents

List of Figures

List of Tables

List of symbols

Latin

A	$[m^2]$	Area
a	$[m/s]$	Speed of sound
β	[-]	Collection efficiency
c	[m]	Chord length
ν	$[m^2/s]$	Kinematic viscosity
C_D	[-]	Drag coefficient
C_L	[-]	Lift coefficient
C_P	[-]	Power coefficient
C_Q	[-]	Moment coefficient
D	$[N]$	Drag
d	[m]	Diameter
Fr	[-]	Froude number
g	$[m/s^2]$	Gravitational acceleration constant
J	[-]	Advance ratio
L	[m]	Lift
l	[m]	Characteristic length
LWC	$[g/m^3]$	Liquid Water Content
Ma	[-]	Mach number
MVD	$[m]$	Median Volume Diameter
n	$[1/s]$	Rotation rate
P	$[W]$	Power
p_0	$[N/m^3]$	static pressure
p_t	$[N/m^3]$	total pressure
Q	$[Nm]$	Moment
R	$[\mathrm{J/K\,mol}]$	Gas constant
Re	[-]	Reynolds number
T	$[N]$	Thrust
t	$[s]$	Time
t	$[K]$	Temperature
t_t	$[K]$	Total temperature
u_+	[-]	Dimensionless velocity
u_T	$[m/s]$	Friction velocity
v	$[m/s]$	Flow velocity
v_∞	$[m/s]$	Free stream velocity
V	$[m^3]$	Volume
x, y, z	[m]	Cartesian coordinates
y_+	[-]	Dimensionless wall distance

Greek

α	[-]	Mass Fraction
κ	[-]	Adiabatic index
η	[-]	Efficiency
ν	$[m^2/s]$	Kinematic viscosity
ρ	$[kg/m^3]$	Density

Acronyms

BVLS	Beyond visual line of sight
CFD	Computational fluid dynamics
IPS	Ice protection system
NTNU	Norwegian University of Science and Technology
SLD	Supercooled large droplet
UAV	Unmanned aerial vehicle

Abstract

Unmanned aerial vehicles (UAVs) are an emerging technology with a large variety of commercial and military applications. As the operational envelope of the UAVs expands, In-flight icing poses an ever growing risk for the safe operation of UAVs. In-flight icing occurs during the flight in supercooled clouds or freezing precipitation. A special hazard is the icing of the rotors or propellers of the UAV, as it may limit the UAVs ability to climb, its range and its controllability. For fixed-wing UAVs, the icing on the propeller limits its range, and may limit its ability to climb or maintain the current cruise altitude. For multi-rotor UAVs, the ice accretion may reduce the flight stability of the UAV, and lead to a loss of control over the aircraft.

While the ice accretion on aircraft has been analysed for many years, only limited research has been conducted to analyse the ice accretion on UAVs. In the last decade, the analysis of icing of UAVs has been researched in detail. While the icing on wings of UAVs has been analysed using experimental and computational methods, no prior research has been performed to calculate the ice accretion on propellers of UAVs. In this thesis, a overview over the existing icing experiments is given. Then, they are used to develop and validate the ice accretion process on the propeller of a UAV using numerical methods. For the propeller of a small UAV, three different icing conditions are analysed, and the effect of the icing conditions on the propeller are analysed. First the aerodynamic performance of a propeller is calculated, where a good accuracy for the thrust calculation has been found. Then the ice accretion calculation has been validated against an experiment for the ice accretion on the rotor of a helicopter. Finally the ice accretion and the performance penalties for a propeller of a small UAV have been calculated. For this analysis three different icing conditions were analysed.

The results indicate, that the ice morphology had a large influence on the aerodynamic properties of the rotor. All icing cases do increase the drag and therefore the power requirement of the rotor, which will limit the range of the UAV. While the performance penalties at temperatures closer to the freezing point are only small, the ice accretion can have a large impact on the thrust and the efficiency of a propeller. This paper highlights the need to implement proper procedures to avoid icing conditions in UAVs. If flying in icing conditions cannot be avoided, effective deicing or anti icing systems on the rotors of UAVs need to be implemented.

Kurzfassung

Unbemannte Luftfahrzeuge (Unmanned Aerial Vehicles, UAVs) sind eine aufstrebende Technologie mit einer Vielzahl von kommerziellen und militärischen Anwendungen. Da sich der Einsatzbereich der UAVs stetig vergrößert, stellt die Vereisung des UAV ein immer größer werdendes Risiko für den sicheren Betrieb von UAVs dar. Die Vereisung tritt bei dem Flug durch Wolken mit unterkühlten Tröpfchen oder gefrierenden Niederschlägen auf. Eine besondere Gefahr ist die Vereisung der Rotoren oder Propeller der UAV, da sie die Steigfähigkeit der UAVs, ihre Reichweite und ihre Steuerbarkeit einschränken kann. Bei Starrflügeldrohnen begrenzt die Vereisung des Propellers seine Reichweite und kann seine Fähigkeit zum Steigen oder zum Halten der aktuellen Reiseflughöhe einschränken. Bei mehrrotorigen UAVs kann der Eisansatz die Flugstabilität des UAVs verringern und zu einem Verlust der Kontrolle über das Flugzeug führen.

Während die Vereisung von bemannten Flugzeugen seit vielen Jahren untersucht wird, ist die Vereisung von UAVs erst in dem letzten Jahrzehnt in den Fokus der Forschung geraten. Bisherige Forschungsarbeiten haben sich auf die Vereisung der Flügel der UAVs konzentriert. Die Vereisung der Flügel von UAVs wurde bereits Mithilfe von Vereisungsexperimenten und Simulationen untersucht worden. Die Vereisung von Propellern wurde noch nicht simulativ untersucht. In dieser Arbeit wird ein Überblick über die bestehenden Vereisungsexperimente gegeben. Mithilfe dieser Experimente wird ein Prozess entwickelt, um die Vereisung von einem Propeller eines UAVs zu untersuchen. Zuerst wird die Leistung eines unvereisten Propellers untersucht. Anschließend wird die Vereisungssimulation mithilfe der Vereisung eines Rotors eines Hubschraubers untersucht. Mithilfe des hierbei entwickelten Prozesses wird die Vereisung eines Propellers eines kleinen UAVs berechnet. Die Vereisung dieses Propellers wird bei drei unterschiedlichen Bedingungen berehnet.

Die Ergebnisse zeigen, dass die Eismorphologie einen großen Einfluss auf die aerodynamischen Eigenschaften des Rotors hat. Alle Vereisungsfälle erhöhen den Luftwiderstand und damit den Leistungsbedarf des Rotors, was die Reichweite des UAV einschränkt.Auch der Schub des Propellers wird bei allen Bedingungen reduziert. Bei Temperaturen nahe dem Gefrietpunkt ist die Reduktion der Effizienz der Propellers klein, aber bei niedrigeren Temperaturen kann die Effizientz über 60% reduziert werden. Diese Arbeit unterstreicht die Notwendigkeit, geeignete Verfahren zur Vermeidung von Vereisungsbedingungen in UAVs zu implementieren. Wenn ein Flug unter Vereisungsbedingungen nicht vermieden werden kann, müssen wirksame Enteisungs- oder Vereisungsschutzsysteme an den Rotoren von UAVs implementiert werden.

1. Introduction

The development of newer and smaller scale electronics and control system has led to increased usage of small fixed-wing unmanned aerial vehicles with a wingspan of 2 to 4 meters to be used as research platforms. The small size allows the unmanned aerial vehicles UAVs to be used in an increasing number of harder to reach areas like the Arctic. During the flight, the UAVs need to deal with a number of severe weather conditions like icing. But icing conditions are not only limited to the arctic, but can happen in moderate climates such as example central Europe [1]. As the ice accretion on the aircraft poses a large thread to the safe operation of the aircraft, manned aircraft use different technologies to combat the thread of icing. Those systems include anti-icing systems that aim to prevent the ice accretion for example by continuously heating the surface of the aircraft. Others use de-icing systems to cyclically remove the ice that has been accumulated on the aircraft before the impact of the ice becomes a threat to the safe operation of the aircraft. Most of this systems use the engine of the aircraft to power the systems. On UAVs, the smaller combustion or electric engine usually does not produce enough heat to power this type of de-icing systems. In the beginning, the US-Airforce did not launch its UAVs, if icing conditions were present, and thus limiting the operational range of the UAVs [11].

In the last decade, a larger effort has been made to developed an better icing protection system for UAVs. One example for this is the IPS technology developed by UBIQ Aerospace, using an electro-thermal system for the deicing of the frame of a UAV. Ice on the surface of a propeller will limit the lift of the wing, as well as increasing the drag of the airfoil [12]. But not only the frame of the UAV is in danger of icing, but also the propulsion system. Most small UAVs use propellers to create the thrust, in contrast to the larger UAVs, which use jet engines. This part is in a great danger of icing, as ice creation here will severely limit the thrust the aircraft is able to produce. The reduction of the thrust will lead to the reduction of the range of the aircraft, or limit the climbing ability of the UAV, which could lead to an impact with the ground.

In the past, the focus of the ice accretion has been on manned aircraft, and only in the last years, extensive research on the ice accretion has been conducted. At the NTNU, the ice accretion on the wing of a small-medium sized UAV has been analysed using experimental and numerical methods by Hann et al. [2].

The conducted work has been focused on the development of icing protection systems for UAVs. The aim of this thesis is to simulate the ice accretion on the propeller of a small-medium UAV under different meteorological conditions using ANSYS FENSAP-ICE. To archive this goal, a number of steps was performed:

- Find experimental data
- Conduct a grid dependency study
- Validate the performance simulation
- Validate the ice accretion simulation
- Run the propeller in three different icing cases

- – Ice accretion

- – Performance calculation

- – Anti-icing simulation

Then the results of the ice accretion simulations are discussed, and a explanations for the phenomena is suggested.

2. Theoretical background

2.1. UAVs

The first UAVs were developed in the 1900 for military applications [13]. This has been the main focus of the development, and today most military forces use UAVs as part of their defense strategies. There is a wide range of different UAV types, where smallest micro-UAVs are used for the short term and agile acquisition of intelligence in a war-zone, long-range UAVs flying at high altitudes can provide a long time surveillance platform reaching any part of the globe. These long-rage UAVs can be of the size of small manned aircraft. In military missions, UAVs have been used for intelligence and surveillance missions, where their small size and the unmanned nature provide an advantage over manned aircraft. UAVs are also used in attack and combat support missions, with many nations developing the first fully autonomous combat UAVs [14].

Since the development of smaller microelectronics, UAVs were also used as small radio controlled aircraft for recreational purposes. The earliest versions used no remote control system. The development of remote controllers lead to the development of the remote controlled aircraft, which is still used today by enthusiast around the globe. The introduction of modern electric motors and control systems increased the capabilities to the point, where this type of UAVs became a useful tool for many commercial operators. These UAVs are commonly used in the construction and the agricultural sectors for surveillance and monitoring applications [15].

Until recently, most UAVs have been operated under visual line of sight operation. Here the controller is able to see the UAV and to control the UAV manually in case of a failure of the autopilot. In order to extend the range and scope of possible operations, many modern UAVs are operated under beyond visual line of sight operations. In this case, the operator is not able to directly see and control the UAVs. This necessitates a larger degree of automation in the UAV, as it needs to be able to autonomously follow the flight plan, without input from the operator. Due to modern advancements in the development of smaller and more powerful micro electronics, the use of an autonomous UAV beyond the line of sight of the operator has become accessible even to recreational model aircraft pilots or commercial operations.

With the introduction of the operation of UAVs beyond the visual line os sight (BVLOS) in the commercial market, the scope of operation of the UAVs increased. While previously only the military was interested in the operation of a UAV in difficult weather conditions, now commercial operators are providing services as well, during which the continuous operation of UAVs during all weather conditions is important. For this reason, UAVs need to cope even with severe weather conditions, in order to provide the services around the year.

2.2. Aircraft Aerodynamics

The main forces every aircraft in stationary flight experiences, as described by Sóbester et al. in [16], are lift, drag, weight and thrust. The lit is usually generated bathe wings or the rotors, which is equal to the weight of the aircraft. Furthermore the drag of the aircraft is balanced by the thrust of the propulsion system. The lift of an aircraft is usually generated at the wing. The shape of the airfoil accelerates the velocity of the air flowing over the top of the wing, which will according to the Equation 2.1 reduce the static pressure above the airfoil and create lift.

$$p_t = p_0 + \frac{1}{2}\,\rho\,v^2 \tag{2.1}$$

The properties of the air close to the wall are of specific importance for the aerodynamic properties of the aircraft. On the surface of the airfoil, the velocity relative to the airfoil is zero. This leads to the development of a boundary-layer between the wall and the airflow where the air has the free stream velocity. The boundary-layer is defined as the distance from the wall, where the velocity of the airflow is 99 % of the free stream velocity according to Schlichting [17]. The velocity profile in the boundary-layer follows different velocity profiles depending on the type of boundary-layer. To predict which type of boundary-layer is prevalent the Reynolds number Re can be used. It is calculated following Equation 2.2. For free-flow applications, one distinguished between the global Reynolds number, where the chord of the airfoil is choosen as the refencence length L is the chord of the airfoil. For the condition of the boundary-layer the local Reynolds number Re_X according to Equation 2.3 is important. Here X is the distance to the leading-edge of the airfoil. At a low Reynolds number, the boundary-layer is typically laminar. This type of flow consists of a very uniform flowfield, which leads to a low momentum transport through the boundary-layer and a low drag. If the Reynolds number increases, the boundary-layer transitions to a turbulent boundary-layer. This transition can occur due to a increased Reynolds number, or it can be induced due to a obstacle in the airflow. The position of the transition is also dependent on the pressure gradient along the airflow. A turbulent boundary-layer is inherently instationary, and leads to a increased drag of airfoil.

$$Re = \frac{u * l}{\nu} \tag{2.2}$$

$$Re_x = \frac{u * x}{\nu} \tag{2.3}$$

The aerodynamic performance of an aircraft is analysed using the nondimensional lift coefficient C_L and the drag coefficient C_D. They can be calculated from the Lift L and the Drag D of an aircraft using the Equations 2.4 and 2.5.

$$L = \frac{1}{2}\,\rho\,A\,C_L\,v^2 \tag{2.4}$$

$$D = \frac{1}{2}\,\rho\,A\,C_D\,v^2 \tag{2.5}$$

2.3. Propeller aerodynamics

If an airfoil is rotating, it is called a rotor. Rotors have a number of different applications, which will be presented here [18]. A propeller is a rotor that is used to generate thrust along an axis. Rotors can be found in different applications. Those include the propellers in aircraft, inside an aircraft engine, in wind turbines and more. If the rotor is used to compress the flow medium, it is called a compressor. If it transforms the energy of the fluid into mechanical energy, it is called a turbine. If it is used to create thrust in the air, while it advances through the air, it is called a propeller. In this thesis, the icing properties of propellers are analysed.

The thrust of an airplane can be produced by a propeller. A propeller operates similar to the wing of the aircraft, but the velocity of the airflow is generated by the rotation of the airfoil. This enables the propeller to generate thrust, even if the velocity of the aircraft is zero. The angle at which the flow hits the airfoil of the propeller is dependent on the velocity of the aircraft and the rotational velocity. The advance ratio J describes the ratio of the velocity generated be the rotation n along the diameter d of the propeller, to the aircraft velocity v_∞[19].

$$J = \frac{v_\infty}{n\,d} \tag{2.6}$$

The lift of the propeller will show a component in the direction of the rotational axis. This force is called the thrust T of the propeller. Because most propellers will be symmetrical along the axis of rotation, the forces radial to the axis of rotation will cancel with the same force generated by the other propeller blades. To compare propellers of different sizes and under different atmospheric conditions, the dimensionless thrust coefficient C_T is created. The thrust coefficient is dependent on the rotational speed n of the propeller, compared to the velocity of the aircraft. For this reason, the thrust coefficient is dependent on the advance ratio.

$$C_\mathrm{T} = \frac{T}{\rho\,n^2\,d^4} \tag{2.7}$$

Next to the thrust, the propeller will also produce a momentum Q against the rotation of the propeller. This momentum is caused by the drag of the propeller blades, as well as the induced drag, which the Blades produce when they spin. This momentum Q can be calculated by the coefficient C_Q according to Equation 2.8.

$$C_\mathrm{Q} = \frac{Q}{\rho\,n^2\,d^5} \tag{2.8}$$

To overcome this momentum, and maintain a constant rotation speed, a certain power is required. This power can be calculated from the momentum and the rotational speed. To compare different propellers, the power coefficient C_P is used according to Equation 2.9.

$$C_\mathrm{P} = \frac{P}{\rho\,n^3\,d^5} \tag{2.9}$$

If the advance ratio of the propeller is larger than one, the efficiency of the propeller can be calculated by comparing the power input to the propeller to the mechanical power the propeller will generate. This can be done by using the power coefficient, the thrust coefficient and the advance ratio in Equation 2.10.

$$\eta = \frac{T v_\infty}{P} = \frac{C_\mathrm{T}\,J}{C_\mathrm{P}} \tag{2.10}$$

A propeller is classified by its diameter, and the pitch of the propeller. The pitch of the propeller is the distance the propeller would travel in one rotation, if the air was a solid medium. This pitch is usually measured at 75% of the radius of the propeller.

2.4. Atmospheric icing

The icing on an aircraft can be subdivided according to the situation were the icing occurs. There is ground icing, which occurs while the aircraft is on the ground. This type of icing is not a large thread to UAVs, as they can be easily protected against it [20].

This thesis is focused on in-flight icing, as this is the main threat to UAVs according to Hann and Johansen [20]. In-flight icing occurs, when a UAV flies through a cloud which contains supercooled liquid droplets. These droplets contain water below the freezing temperature of water. The conditions where supercooled droplets are present in the atmosphere are called atmospheric icing conditions. Those icing conditions can occur around the year [21]. The frequency of days with ice accretion can be seen in Figure 2.1. That the icing is not only happening during the winter months can be seen in Figure 2.2. Here the frequency of days with atmospheric icing conditions is plotted against the date, and the height in 1000 feet (KFT).
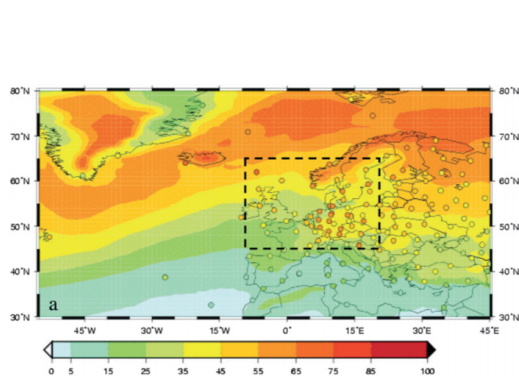
Figure 2.1.: Frequency of atmospheric icing conditions in Europe [1].
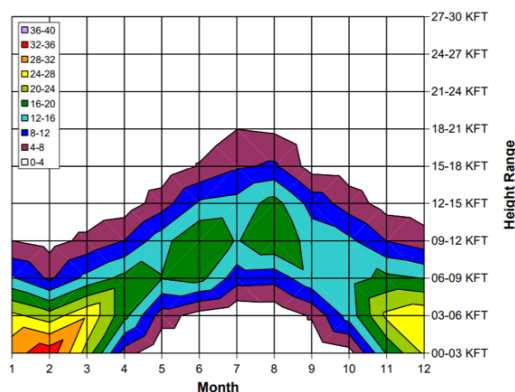
Figure 2.2.: Frequency of atmospheric icing conditions in Stockholm for different altitudes throughout the year [1].

The rate at which the ice accretion happens is dependent on a number of different environmental factors. These include the temperature, the liquid water content (LWC) and the droplet size. The size of the droplets is classified by the median volume diameter (MVD) [12]. The ice accretion rate is also dependent on the aircraft, especially on the aircraft speed an shape [2]. When the supercooled droplets impact the UAV, they will create water film on the surface, or freeze instantly. The process of water attaches to the surface is called impingement. The water in this film will now progress in one of three ways. It can freeze on the surface, it can move along the surface of the aircraft, or it can reenter the air stream. The ratio at which this the processes occur defines the shape of the ice [12]. This is mainly dependent on the temperature of the air, and the speed and size of the aircraft. The three most common ice shapes will be introduced below.

6
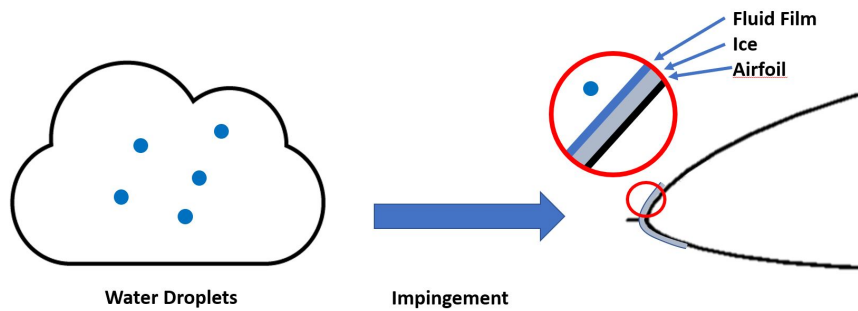
Figure 2.3.: Steps of the ice accretion on an aircraft.

2.4.1. Rime ice

When the temperature of the droplets is very low, the droplets freeze almost immediately after they impact the surface of the aircraft. This creates an ice shape, which will build into streamlined shapes along the leading-edge of the airfoil. This ice shape will usually have a low performance penalty for this type of icing. During the ice accretion small air pockets will be included into the ice shape, which leads to a characteristic white appearance of the ice. This can be seen in Figure 2.4. The resulting ice shape may be rough and show ice feathers [12].

2.4.2. Glaze ice

Glace ice forms when the temperatures are close to the freezing point of water. At this temperatures, the droplets do not freeze instantly. The water will stay longer in the liquid phase in the fluid film. This results in smoother ice shapes, as the water is able to move from the place of the impingement and create complex ice shapes on the surface. Due to the slow freezing process, the ice shape does not include air bubbles, which leads to a clear appearance of the ice. Therefore, the ice is often called clear ice. This can be seen in Figure 2.5. This aggravates the dangers of this type of ice in manned aviation, as it may not be registered during a visual inspection by the pilot [22]. The intricate ice shapes, which can include protruding ice horns, can lead to high performance penalties [12].

2.4.3. Mixed ice

In intermediate conditions between glaze and rime ice conditions. This process may be supported by the release of latent heat during the icing process. This ice shape can also grow into into complex shapes like horns, and is also likely to see large performance penalties [23].

2.4.4. Other icing conditions

Next to the classical in-flight ice shapes there are a number of different icing conditions. Freezing precipitation can lead to a much more severe icing penalties under certain conditions [24]. This
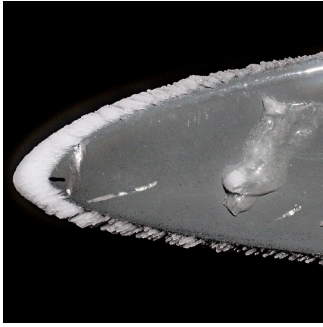
Figure 2.4.: Rime ice shape on a UAV wing [2].

Figure 2.5.: Glaze ice shape on a UAV wing [2].
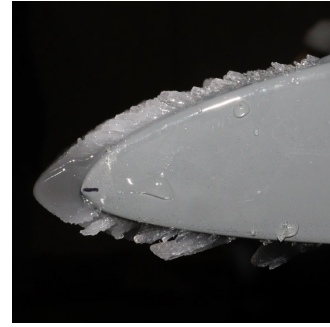
Figure 2.6.: Mixed ice shape on a UAV wing [2].

form of icing can be much more severe in its impact on aircraft [12]. This is due to the large size of the droplets. Compared to cloud droplet with a MVD of about 40-50 μm, the size of the droplets can range up to a 2 millimeters in diameter. For this reason it is called supercooled large droplet (SLD) icing. The ice accretion rate during SLD icing conditions can be very rapid, leading to a substantial performance penalty in a very short time. Another hazard for UAVs and aircraft are snow and ice. Because the high speeds of aircraft, ice and snow will usually not be able to stick to the surface of the aircraft, leading to a very low hazard. But it might pose a danger to very slow moving aircraft like multicopters [25].

2.4.5. Effects of icing

The main forces every aircraft in stationary flight experiences is lift, usually generated by the wings or the rotors. Furthermore the drag of the aircraft is countered by the thrust of the propulsion system. The ice accretion can affect all of those four main forces [26]. The largest influence is in the decrease of the aerodynamic performance penalties. The ice shape will lead to the introduction of disturbances into the airflow, which will lead to a decreased lift, and a increased drag of the airfoil. Additionally the mass of the ice will increase the mass of the aircraft [27], and the ice accretion on propellers will reduce the efficiency of the propulsion system [9]. The ice shapes on the wing can be separated into four groups according to Bragg et al. [12]. They are visible in Figure 2.7 This shapes in the descending order of their impact on the aerodynamic properties according to Bragg et al. are:

- spanwise-ridge ice
- horn ice
- streamwise ice
- ice roughness

The ice roughness is a thin layer of ice, that will increase the roughness of the surface. This increase in surface roughness can lead to a increased drag by the increased shear stress on the surface. Furthermore, the increased roughness can introduce turbulence and therefore lead to a faster transition from a laminar to a turbulent boundary-layer. This leads to an increase of the drag of the airfoil, and the longer turbulent boundary-layer can lead to a separation of the flow
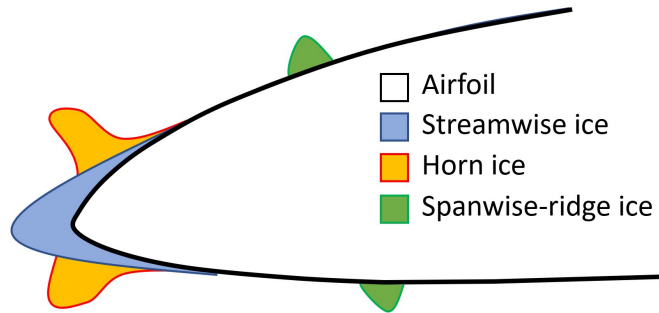
Figure 2.7.: Common ice shapes, adapted from [2].

from the surface, thus limiting the maximum lift and the stall angle of the airfoil. The horn ice is common under glaze ice conditions. It leads lo large recirculating zones behind the horns, and it is forcing a early laminar turbulent transition at the leading-edge of the airfoil. The spanwise ridge ice is a special icing condition, that happens if the leading-edge of the airfoil is protected by an ice protection system (IPS), and the ice is freezing behind the area protected by the IPS. This can be due to SLD conditions where the area of the IPS is insufficient for the extend of the icing. This can also happen when the IPS is melting the ice, and the water flows behind the IPS area to refreeze. This so called runback icing can also be dangerous for the control surfaces behind the IPS system, as the mechanics of the control system might be blocked by ice [12].

Szilder et al. have described the influence of the lower Reynolds numbers of a typical UAV compared to a manned aircraft [28]. By using a morphogenic ice accretion model, they found that lower Reynolds numbers lead to a increase in glaze ice, and a reduction of the rime ice.

The theoretical polar of a iced airfoil can be seen in Figure 2.8. It can be seen, that the maximum lift, has been reduced. The drag coefficient is also higher, compared to the clean airfoil.
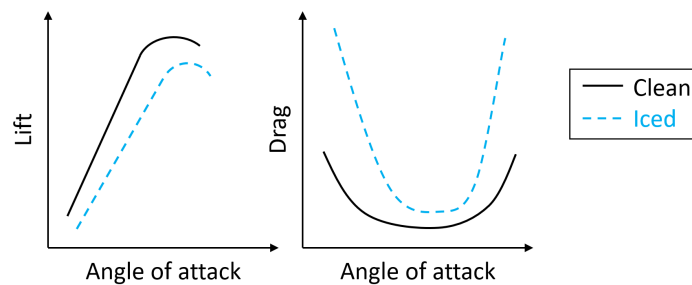
Figure 2.8.: Conceptual aerodynamic performance degradation adapted from [2].

2.5. Experimental data

The main focus of the icing research has been the manned aviation. So the focus of experimental campaigns has been on icing in higher Reynolds number conditions than what a typical UAV does experience [20]. Only a few years ago, the first larger scale experimental campaigns to analyze icing on UAVs has been conducted [20].

For icing on rotors, the main focus has been on the icing on propellers and rotors of helicopters. In the course of this thesis, a database of icing experiments on aircraft and rotorcraft has been generated, which will be presented in the following chapters. Icing experiments can be divided according to the the type of data they aim to generate. The categories are the impingement experiments, ice accretion experiments and the aerodynamic performance studies.

2.5.1. Impingement data

Impingement experiments are conducted at higher temperatures to prevent ice from forming, but rather aim to detect the amount of water that impinges the aircraft at different locations. To locate the amount of water, that impacts each region, special colored paper can be used to detect the water [29]. Most impingement data has been collected in the impingement on the wings of manned aircraft. No impingement study has been performed on the impingement on the propeller of a UAV.

2.5.2. Ice accretion data

Another type of icing experiment is an ice accretion study. Those experiments are conducted in an icing wind tunnel (IWT). A IWT is similar to a classical wind tunnel, with a cooling system to provide low air temperatures, and a spray system, which enables the injection of water droplets into the airflow before entering the testing chamber. Therefore, experiments at set temperatures, with a fixed LWC and MVD can be conducted. An example for a IWT is the Icing Research Tunnel at the Glenn Research Center. The final ice shape can be detected using manual tracings, or in more recent experiments 3D Scans of the ice are performed. The total mass of the ice on the test model can also be measured.

2.5.3. Ice performance penalties

Due to the additional provisions for the water droplet spray systems, an IWT commonly can not be used for the measurement of the aerodynamic influence of icing. To measure the performance degradation, an artificial ice shape is produced, and then attached to the test model in a wind tunnel to measure the performance loss by this ice shape. This ice shapes can be derived from experiments, or from icing simulations.

2.5.4. Database

A database including all literature with experimental data (impingement, ice accretion, performance penalties). was created. For this database, existing experiments have been collected. The experiments eligible for the database had to be either impingement measurement, ice accretion

studies or a study of the performance penalties. All experiment have to be either published. The experiments were classified according to the type of the study. Additionally the range of the used Reynolds numbers and Mach numbers was listed. For the ice accretion experiment the icing conditions are listed. The data created in the experiments is listed. Examples for the possible data types would be manual tracings or 3D scans. All experiments were separated into experiments that are quasi-2D or 3D experiments. In a quasi-2D experiment, the boundary conditions and the geometry are constant in one direction perpendicular to the airflow.

In total 71 publications with ice accretion have been collected and sorted into a database which has been published in [30] and can be seen in Appendix A. This database can be used for the validation of the numerical calculations. For this, the experiments are recreated using numerical methods, and the results are compared to the results from the experiments. Some of the experiments are highlighted in the following part.

The research into the ice accretion has been mainly focused on the ice accretion on wings. Especially the research at the Icing Research Tunnel at the NASA Glenn Research Center has been focused on the icing on the wings of aircraft. The first published works analyze the ice shapes on a NACA0012 airfoil in 1992 [31]. In future research, the ice accretion for a number of different airfoils and also engine inlets has been analysed. In the last few years, the research has branched out into the research on the icing on 3D geometries like swept wings and also the icing on a tail rotor of a helicopter.

The icing on the tail rotor was not used as a test case for the ice validation, as the airflow to the rotor is perpendicular to the axis of the rotor, and thus creating a different airflow around the rotor compared to a propeller.

Since 2017, a large number of ice accretion experiments have been conducted by a research group around Hu, Lio and Li at the Iowa State University Icing Research Wind-Tunnel (ISU-IRWT) with a number of different geometries including the inlet of a turbofan engine, a wind turbine blade [9], bride cables and a model of a UAV propeller. For this UAV propeller, icing experiments at multiple meteorological conditions have been performed, as well as an analysis of the wake properties of the propeller and experiments with different surfaces of the propeller [9]. Because the data available for the created ice shapes is limited to pictures, the experiments could not be used for the validation of the icing of the propeller.

Lately, a number of icing experiments for the evaluation of the ice accretion on the wings of a UAV have been performed by Hann at the Cranfield icing wind tunnel and the VTT Technical Research Centre of Finland. Those experiments show the ice accretion at low Reynolds numbers (Re=0.8-1.6×10^6) on a RG-15 and a S826 airfoil. The ice shapes from this experiments have been scanned in a 3D scanner, for the analysis of the performance. Those results are relevant for the icing of the propeller, as they represent the icing on the UAVs the propeller is commonly used for, and thus is influencing the meteorological conditions the propeller is used at.

At the Adverse Environment Rotor Test Stand (AERTS) different experiments on the ice accretion on scaled helicopter rotor blades have been performed starting in 2010. For this experiments, the propeller is set in a measurement chamber without an active propulsion of the airflow. The only source of the velocity of the air around the rotor is the induced velocity by the rotor. This combined with the shape of the test chamber makes the test chamber usefull for the analysis of the icing of a propeller while in the ground effect of the ground.

Lee and Boeren have analysed the effect of ice accretion on the aerodynamic properties of the Common Research Model (CRM) wing in [32]. Here the ice shapes were created in an IWT, and then simplified and applied to a wind tunnel model for the analysis in a dedicated aerodynamics

wind tunnel. Because the CRM is representative of a jet aircraft, the Reynolds numbers analysed are high (Re=1.6-11×10^6). Hann has analysed the performance loss of numerical created ice shapes for a UAV in the NTNU wind tunnel [2]. Here the Reynolds numbers are lower to fit with the use case for a small UAV wing. The tested Reynolds numbers vary from $0.9 \cdot 10^6$ to $1.4 \cdot 10^6$.

In this thesis, an experiment on the AERTS where the ice accretion investigated on a model of a helicopter blade using a NACA0012 airfoil was used for the validation of the ice accretion simulation. In the Chapter , the results of the ice accretion were compared to the results of the ice accretion study at the University of Iowa State university on the ice accretion on a propeller of a UAV. A shot overview over the two experiments is given in Table 2.1.

Title	Geometry	Year	Source
An experimental study on the transient ice accretion process over the blade surfaces of a rotating UAS propeller	UAV Propeller	2017	[9]
An experimental correlation between rotor test and wind tunnel ice shapes on NACA 0012 airfoils	Helicopter rotor	2017	[7]

Table 2.1.: Experimental data used in this thesis.

2.6. Numerical calculation

In this section, the methods for the calculation of the ice accretion are presented.

2.6.1. Fluid calculation

For the calculation of the flow of the air, computational fluid dynamics (CFD) are used. For this process, first the problem needs to be discretized in the time and spatial dimensions, and then a set of partial differential equations is solved to calculate the final flow field. For the time resolution, the time is divided into discrete time steps. For the spatial discretization, the computational region is divided into a mesh. The solution is calculated for every time step at every cell of the mesh, and the result of the calculation will define the solution of the calculation.

2.6.2. Navier-Stokes equations

To calculate the flow of the air in this thesis, the Naiver Stokes Equations 2.11, 2.12 and 2.13 are used. The Navier-Stokes equations are a set of partial differential equations. They contain the conservation of momentum, the conservation of mass and the conservation of energy. Due to the viscous term, they are of a second order, and the inertia terms makes the equation nonlinear. To solve this set of equations, a set of boundary conditions has to be imposed. This includes the introduction of a certain velocity at the inlets, the pressure at the outlets and the velocity of 0 at the walls of the propeller [33].

$$\frac{\partial \rho}{\partial t} + \frac{\partial (\rho u_i)}{\partial x_i} = 0 \tag{2.11}$$

$$\frac{\partial (\rho u_i)}{\partial t} + \frac{\partial [\rho u_i u_j]}{\partial x_j} = -\frac{\partial p}{\partial x_i} + \frac{\partial \tau_{ij}}{\partial x_j} + \rho f_i \tag{2.12}$$

$$\frac{\partial (\rho e)}{\partial t} + (\rho e + p)\frac{\partial u_i}{\partial x_i} = \frac{\partial (\tau_{ij} u_j)}{\partial x_i} + \rho f_i u_i + \frac{\partial (\dot{q}_i)}{\partial x_i} + r \tag{2.13}$$

2.6.3. Flow characteristics

The density of the air can change depending on the temperature and the pressure of the air. For this reason air is called a compressible medium. This comprehensibility has many impacts on the behavior of the airflow. It limits the speed a, at with which pressure changes can be distributed through the air. The speed at which a small pressure change can be transmitted trough the fluid is called the speed of sound. It is dependent on the isotropic coefficient κ, the universal gas constant R, and the temperature t. It can be calculated according to Equation 2.14 [34].

$$a = \sqrt{\kappa R t} \tag{2.14}$$

The quotient of the current airspeed to the speed of sound is the Mach number which is described in Equation 2.15. There is a distinction between the local and the global Mach number. The local Mach number describes the ratio of the local air velocity to the speed of sound, while the global mach number is used to describe the ratio of the velocity of the approaching air to the speed of sound.

$$Ma = \frac{v}{a} \tag{2.15}$$

The characteristics of the flow change with the Mach number. At a Mach number below 1, the flow is called a subsonic flow, and at a Mach number greater than one, the flow is supersonic. If the flow is decelerated from a supersonic to a subsonic flow, a shock wave is created. Shock waves are also present if a supersonic flow changes its direction and is decelerated.

With the increase of the Mach number, the total Temperature t_t of the air changes. The total temperature of the air is the temperature, the air would have, if it were to be decelerated to a standstill in an adiabatic fashion. The Mach number on the tip of a UAV propeller can reach up to 0.8[35].

$$t_{\mathrm{t}} = t * (1 + \frac{1}{2} \kappa \, Ma^2) \tag{2.16}$$

2.6.4. Turbulence models

The Navier-Stokes equations can be used to calculate the flow in the full computational domain. This type of calculations is called a direct numerical simulation (DNS). Those simulations resolve the full scale of the turbulence, from larger vortexes, to the smallest scales, at which the turbulence is dissipated into heat. This requires a large amount of computational power for even

the smallest problems, which is why this kind of simulations is currently not commonly used for practical applications of CFD [36].

In order to simplify the simulations and to reduce the requirements on the grid used in the simulation, turbulence models are used. A turbulence model splits the flow equations into a stationary and a fluctuation part. The assumption is that the average of the fluctuating parts is zero, allowing us to calculate the averaged flowfield. Because this leads to new factors in the Navier-Stokes equation, the new set of equation needs additional equations to be closed. These additional equations are empirical models, which have been developed. The new set of equations is called a Reynolds-averaged Navier-Stokes (RANS) equation. The complexity of the turbulence models varies. The lowest complexity lies in analytical models, which predict the turbulence values. Those models are rarely used outside of the calculation of simple cases, as they are unable to cope with complex geometries. They are only valid for the specific case they have been validated against.

To cope with complex geometry, transport equation models are used. They calculate a transport equation for one or two properties of the flowfield. This enables the models to cope with different flow phenomena at different positions on the flow field. By using a transport equation, they are able to take the history of the flowfield into account. A common example for a one Equation turbulence model is the Spalart Allmaras turbulence model. This turbulence uses a transport equation for an auxiliary property derived from the turbulent viscosity. This model is well know for working well with aerodynamic shapes. For this reason it has been commonly used in CFD calculations of aircrafts. The two equation turbulence models can be classified into the two most common categories. The k-ϵ Models use the kinematic eddy viscosity k and the dissipation ϵ. The k-ω turbulence models transport the specific rate of dissipation ω next to k. Although the best turbulence model is always very much case specific, in general the k-ϵ turbulence models are better at calculation the airflow in the free stream, while k-ω turbulence models perform better in the boundary-layer. Therefore the k-ω SST model was created. It includes a version of the k-ϵ which was transformed to use omega as a transport equation. It uses the wall distance as a parameter to switched between both models, using the k-ω turbulence model in the boundary-layer and a k-ϵ turbulence model in the free stream.

All RANS models assume that the turbulence is isotropic, which is not true in all flow situations. In order to deal with anisotropic turbulence, the Reynolds stress tensor model have been developed. They calculate the turbulence in all space directions, but they increase the complexity od the simulations.

In order to refine the calculations of large vortices, while keeping the computational cost to a moderate level, large eddy simulations (LES) have been developed. Here the larger vortices are resolved in the simulation, while the smaller scales of turbulence are calculated using a subgridscale turbulence model. In a further refinement of this is the detached eddy simulation. Here a LES implementation is used to calculate the free flow, while a unsteady implementation of a RANS turbulence model is used to calculate the flow close to a wall.

Boundary-layer

The boundary-layer play a very important role in the calculation of the flow. It is therefore necessary to ensure, that the resolution of the grid along the boundary-layer is sufficient for the chosen turbulence model. For this reason the wall distance of the first cell of the grid is very important. The wall distance of the first cell is calculated by its normalized wall distance y_+.

$$u_{\mathrm{T}} = \sqrt{\frac{\tau_{\mathrm{W}}}{\rho}} \tag{2.17}$$

$$y^+ = \frac{y\, u_{\mathrm{T}}}{v} \tag{2.18}$$

$$u^+ = \frac{u}{u_{\mathrm{T}}} \tag{2.19}$$

2.6.5. Droplet trajectories

For the calculation of the droplet trajectories, a multi-phase simulation is needed. The choice of the right multiphase model depends on the topology of the multiphase flow that is modelled. A dispersed multiphase flow characterized by finite particles which are dispersed in a continuous phase. For example, this describes the water droplets in the cloud before they impact the surface of the aircraft. In contrast, a stratified multiphase flow is a flow were the two phases are separated by interfaces. On this interfaces for example free surface effects like the surface tension are important. This will describe the fluid film on the surface of the aircraft. There are two main types of multi-phase models. In the Euler-Lagranian method, the trajectory of each particle is tracked using an Lagranian method, while the flow is calculated using a Eulerian approach. Here the full volume is classified as a continuum. This approach is limited to a small number of particles. In an eulerian multi-phase model, both phases are characterized as a continuum, and characterized by their mass fraction in each volume element. The mass and momentum conservation equation are separately solved for both phases. For the interaction between the two phases, the drag force between the two is calculated. The drag force can be calculated using the Equation 2.20.

$$D = \frac{1}{2}\, C_{\mathrm{D}}\, \rho\, S\, v^2 \tag{2.20}$$

The value for the drag coefficient C_{D} has to be evaluated for the specific test case. Especially with higher flow velocities, the drag force could deform the droplet, leading to a change in the C_{D}. Also the buoyancy effect between the two fluids has to be considered. The Froude number describes the ratio of the inertia to the gravity field following Equation 2.21.

$$Fr = \frac{u}{\sqrt{g\, \frac{\rho_{\mathrm{a}} - \rho_{\mathrm{a}}}{\rho_{\mathrm{w}}}\, l}} \tag{2.21}$$

For a multiphase flow of small water droplets immersed in Air, the set of equations for the calculation of the droplet trajectories can look can be reduced to Equations 2.22 and 2.23.

$$\frac{\delta\, \alpha}{\delta\, t} + \Delta\, (\alpha\, u_{\mathrm{d}}) = 0 \tag{2.22}$$

$$\frac{D\, u_{\mathrm{d}}}{D\, t} = \frac{C_{\mathrm{D}}\, Re}{24\, K}\, (u_{\mathrm{a}} - u_{\mathrm{d}}) + (1 - \frac{\rho_{\mathrm{a}}}{\rho_{\mathrm{w}}})\, \frac{1}{Fr^2}\, g + \frac{\rho_{\mathrm{a}}}{\rho_{\mathrm{w}}}\, \frac{D_{\mathrm{a}}\, u_{\mathrm{a}}}{D\, t} \tag{2.23}$$

15

2.6.6. Icing simulation

The final step is to calculate the ice accretion from the data. The Messinger model describes the ice accretion process with a series of partial differential equations[37]. The central part of the equation is the calculation of the fluid film. All the possible interactions of the fluid film in the Messinger model can be seen in Figure 2.9. The velocity u of the water film can be calculated by using the Newton approach for the velocity gradient perpendicular to the applied force in a viscous fluid using Equation 2.24 dependent on the distance from the surface y, and the shear stress τ from the air [38].

$$\tau_{yx} = \eta \, \frac{\delta u}{\delta y} \tag{2.24}$$
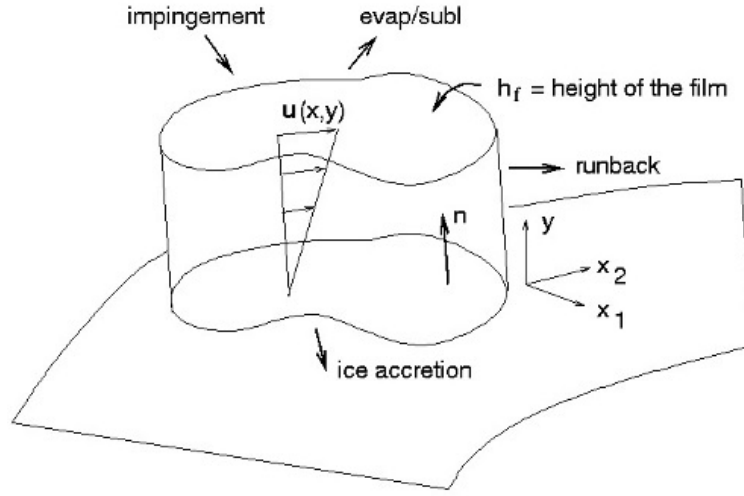
Figure 2.9.: Interactions of the fluid film during the ice accretion in the Messinger model [3].

Given that the velocity at the bottom of the fluid film is 0, the velocity at each point of the fluid film can be calculated. Here x and y describe the position on the surface of the airfoil, while z denotes the distance perpendicular to the airfoil.

$$u_{\mathrm{f}}(x, y) = \frac{y}{\mu_{\mathrm{w}}} \, \tau_{\mathrm{wall}}\,(x, y) \tag{2.25}$$

By integrating the equation 2.25 over the thickness of the fluid film h_{f}, the average speed of the fluid film can be calculated using equation 2.26.

$$\bar{u}_{\mathrm{f}}(x, y) = \int_0^{h_{\mathrm{f}}} \frac{y}{\mu_{\mathrm{w}}} \, \tau_{\mathrm{wall}}\,(x, y)\, dy = \frac{h_{\mathrm{f}}}{2\,\mu_{\mathrm{w}}} \, \tau_{\mathrm{wall}}\,(x, y) \tag{2.26}$$

This leads to the following system of partial equations for the ice accretion.

$$\rho_{\mathrm{w}} \left[\frac{\delta h_{\mathrm{f}}}{\delta t} + \nabla(\bar{u}_{\mathrm{f}}\, h_{\mathrm{f}}) \right] = v_\infty\, LWC\, \beta - \dot{m}_{\mathrm{evap}} - \dot{m}_{\mathrm{ice}} \tag{2.27}$$

$$\rho_{\mathrm{w}} \left[\frac{\delta h_{\mathrm{f}} \, C_{\mathrm{w}} \, \tilde{T}}{\delta t} + \nabla(\bar{u}_{\mathrm{f}} \, h_{\mathrm{f}} \, C_{\mathrm{w}} \, \tilde{T}) \right] = \left[C_{\mathrm{w}} \, \tilde{T} + \frac{\|u_{\mathrm{d}}\|^2}{2} \right] * U_{\infty} \, LWC \, \beta$$

$$- \, 0.5(L_{\mathrm{evap}} + L_{\mathrm{subl}}) \, \dot{m}_{\mathrm{evap}} + (L_{\mathrm{fusion}} - C_{\mathrm{ice}} \, \tilde{T}) \, \dot{m}_{\mathrm{ice}}$$

$$+ \, \epsilon \, \sigma \, (T_{\infty}^4 - T^4) + \dot{Q}_{\mathrm{h}} \quad (2.28)$$

Equation 2.27 calculates the conservation of mass of the fluid film, while equation 2.28 Calculates the energy conversation. the values on the right side of equation 2.27 denote the mass change by water impingement, evaporation and ice accretion. The terms on the right side of equation 2.28 denote the heat transfer by the impingement of supercooled droplets, the evaporation of water and the sublimation of ice, and the convective and radiative heat transfer respectively.

3. Data basis and methods

In this section the used method and the data basis for the thesis are presented.

3.1. Numerical model

For the numerical calculation of the icing, ANSYS FENSAP-ICE version 20.1 is used [3]. This provides a suite of different modules, to calculate the different aspects of the ice accretion process. ANSYS FENSAP-ICE consist of three different programs used for the icing simulation, which will all be presented in this part.

- FENSAP
- DROP3D
- ICE3D
- FLUENT Meshing

FENSAP is the fluid solver, DROP3D calculates the fluid particle trajectories, and ICE3D is the ice accretion solver. The simulation is an iterative process. In the beginning, FENSAP calculates the airflow. The interaction between the different programs can be seen in Figure 3.1 After FENSAP reaches a finished solution for the airflow in this step, DROP3D calculates the Droplets trajectories and ICE3D calculates the new ice shape. Afterwards the simulation is remeshed using Fluent meshing. This is necessary to enable FENSAP to calculate the flow taking into account the new ice shape. This loop is repeated for ten times in every icing simulation in this thesis.
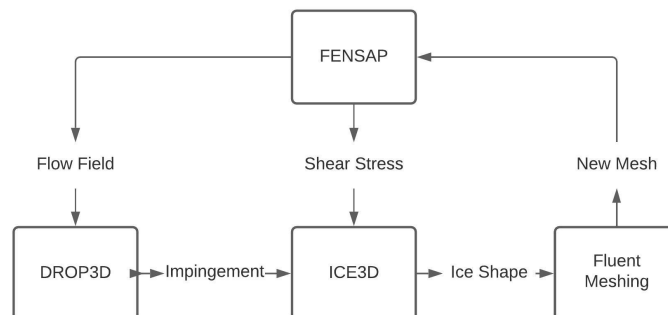

Figure 3.1.: Simulation process in ANSYS Fensap-ICE.

For the calculations of the performance degradation, the flowfield is calculated using FENSAP. It is first used to calculate the flowfield using the clean performance mesh of the simulation.

After the icing simulation, a new mesh is generated in Pointwise, and FENSAP is then used to calculate the aerodynamic performance of this new mesh.

3.1.1. FENSAP

FENSAP is a state-of-the-art CFD solver. It is used for the ice accretion results, as well as the standalone aerodynamics simulations. FENSAP is used to calculate a steady state airflow. It utilizes a weak Galerkin finite element method for the spatial resolution. FENSAP is used to calculate the flowfield by using the full Navier-Stokes equation to calculate a compressible airflow. The turbulence is modeled using RANS equations and a k-ω SST turbulence model for the performance calculations or a Spalart-Allmaras turbulence model for the icing simulations.

During the icing simulations, the flowfield calculated in FENSAP is used to calculate the droplet distribution, and the Shear stress values calculated by FENSAP are used to calculate the ice shape in ICE3D [3].

3.1.2. DROP3D

The droplet distribution is calculated using a Eulerian multiphase model using DROP3D. I takes the velocities of the flowfield and calculates the distribution [3]. The method was presented in Chapter 2.6.5. It calculates the impingement data that is vital for the calculation of the ice shape [38].

3.1.3. ICE3D

The ICE3D module performs the calculation of the ice accretion rate. It takes the impingement values from DROP3D and the friction forces from FENSAP. It uses the Messiger model introduced in Chapter 2.6.6.

ICE3D is also able to calculate the required loads of a icing protection system (IPS). For this estimation, it solves the equation for the heat flux in order to calculate the required load to keep the temperature of the propeller surface at 0°C. This would prevent any ice from forming. Here two different modes of IPS operation are distinguished. In the running wet scenario, the loads to keep the fluid film at 0°C are calculated, while in the fully evaporative simulation mode, the required loads for the evaporation of all the water that impacts the surface is calculated. The fully evaporative operation mode has the benefit, that no runback icing is possible [3].

3.1.4. Fluent meshing

After each cycle, a new volume mesh is created using Fluent meshing. For this, the ice shape calculated by ICE3D is extracted, and combined with the wind tunnel from the volume mesh [39]. To unite both geometries, a surface wrapping operation is performed. In this operation, beginning from a point which is known to be in the computational region, a mesh is calculated to cover the whole surface of the new geometry. The grid size of this mesh can be specified for each contacting surface. This new watertight mesh is used as a basis for the calculation of the new volume mesh. This new volume mesh has similar meshing settings to the initial mesh, in order to get similar

results. After the new volume mesh has been calculated, the flow solution is interpolated from the old mesh to the new mesh, in order to accelerate the convergence in future meshing steps.

3.1.5. Rotation

The propeller is rotating through the computational domain. This needs to be captured in the simulation, as it is very important for the flow field through the propeller. There are many ways to capture the rotation of a object. The first option, is to rotate the geometry and create a new mesh with the new position of the propeller. After the new mesh has been generated, the solution could be interpolated on the new mesh, and a new time-step could be calculated. This is very inefficient, as for every time-step a new mesh has to be calculated, this option is not used. In ANSYS FENSAP, the rotation is calculated, by using a rotating reference system. In this case, the mesh stays the same, throughout the simulation. The velocities are not calculated in reference to a stationary mesh, but the mesh does rotate around the assigned axis. All velocities are calculated in reference to this rotating mesh. For the post processing, the velocities transformed to a stationary mesh [3].

3.1.6. Interfaces

Because most propellers are rotational periodic, it is not necessary to calculate the full propeller. For the propeller with 2 blades, it is enough to calculate half of the propeller, and use a periodic interface condition to simulate the other half. In ANSYS FENSAP-ICE, conformal periodic interfaces are used. This means, that every node at the interface has a corresponding node at the other side of the Interface. All values are exchanged over the interface, as if the other side were a neighboring cell in the mesh. Only the velocity gets transformed. For this transformation, the velocity vector is rotated around the axis of rotation in the angel of the two interface boundary. In the case of the two bladed propeller, the rotation angle is 180°.

3.1.7. Post processing

The post processing is done in Tecplot 360 EX in the version 2019 R1. This program is used to calculate the forces of the propeller. For this the forces along the axis have to be calculated, as well as the moment along the axis of rotation. The first step is to calculate the normal vector $\bar{n}$ of the mesh at the surface of the propeller. The derivative of the normal vector in each spatial direction are n_X, n_Y and n_Z. The derivative of the shear stress vector in each dimension are given by ANSYS FENSAP, and are τ_X, τ_Y and τ_Z. The pressure p and the reference pressure p_Ref are taken from ANSYS FENSAP and the setup of the simulation. With this information, for each face the forces in each direction can be calculated with Equations 3.1, 3.2 and 3.3.

$$f_\mathrm{X} = \tau_\mathrm{X} - n_\mathrm{X} * (p - p_\mathrm{Ref}) \tag{3.1}$$

$$f_\mathrm{Y} = \tau_\mathrm{Y} - n_\mathrm{Y} * (p - p_\mathrm{Ref}) \tag{3.2}$$

$$f_\mathrm{Z} = \tau_\mathrm{Z} - n_\mathrm{Z} * (p - p_\mathrm{Ref}) \tag{3.3}$$

The thrust can be derived by integrating the force in the direction of the propeller axis over the surface of the propeller. Because only one blade of the propeller is calculated, the force needs to be multiplied by the amount of blades in the propeller.

The moment of the propeller can be calculated using the position of the face in a carthesian coordinate system in the center of the rotation. The coordinates are in this case p_X, p_Y and p_Z. The moments m_X, m_Y and m_Z can be calculated according to Equations 3.4, 3.5 and 3.6.

$$m_X = p_Y\,f_Z - p_Z\,f_Y \tag{3.4}$$

$$m_Y = p_Z\,f_X - p_X\,f_Z \tag{3.5}$$

$$m_Z = p_X\,f_Y - p_Y\,f_X \tag{3.6}$$

3.2. Geometries

3.2.1. DA4002

The first validation case is the DA4002 propeller created by Deters [5]. This propeller was chosen for the availability of good data. This propeller uses a Clark-Y airfoil. The trailing-edge of the airfoil has been modified using XFoil version 6.47 [40] to get a trailing-edge gap of 1 mm, with a blending distance of 80% of the chord length of the airfoil. The distribution of the twist and the chord of the propeller over the radius can bee seen in Figure 3.3. The propeller has a constant chord length of 180mm. To construct the shape of the propeller, The cross section of the propeller has been calculated at 14 cross sections. The central hub of the propeller has been simulated as a cylinder, with a free shape to connect the hub to the first layer of the propeller. This has been done using XFoil.
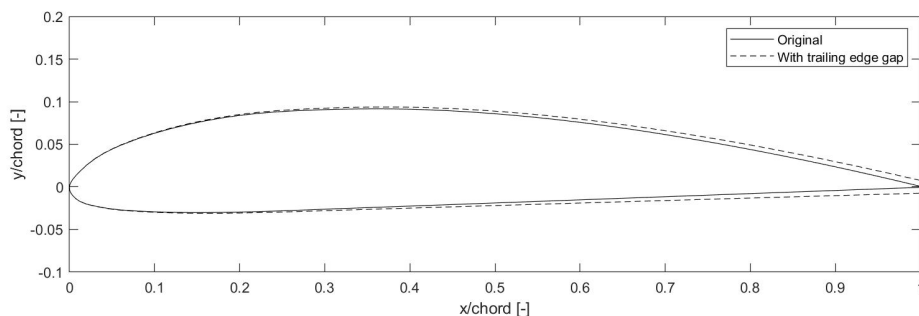
Figure 3.2.: ClarkY airfoil with and without trailing-edge gap[4].

To generate the geometry for the propeller, a Matlab script was generated, to generate a File with the position of the points on the airfoil at 13 cross sections of the propeller. This point cloud was imported into CATIA, and the Shape of the Propeller was created by connecting the cross sections. The hub of the propeller was approximated using a cylindrical shape. The final shape of the propeller in the simulation can be seen in Figure 3.4.

The radius of the simulation region is 5 times as wide as the radius of the propeller, and the distance between the propeller and the inlet and outlet is 2.5 times the radius of the propeller. This is done to ensure that the boundary conditions have a minimal influence on the aerodynamic coefficients of the propeller. Only half of the propeller is simulated, the other half is simulated

Figure 3.3.: Twist distribution of the DA4002 propeller [5].

Figure 3.4.: Geometry of the DA4002 propeller with cross sections.

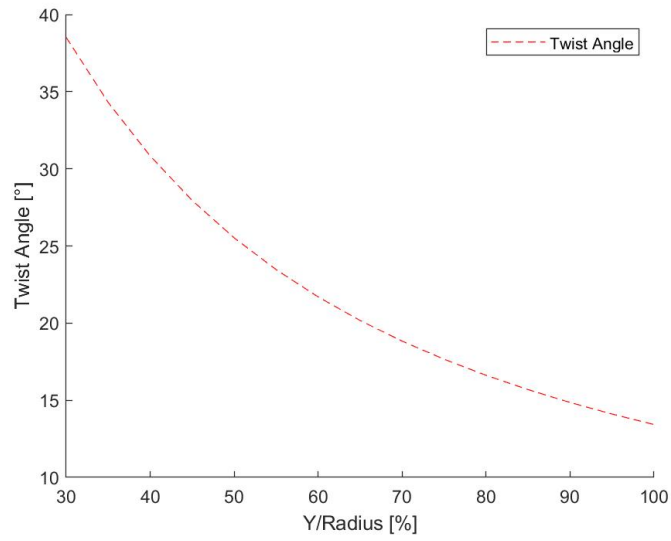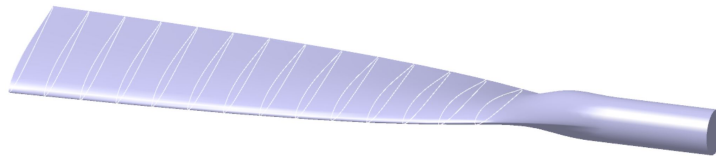using conformal periodic interfaces. This reduces the amount of cells in the simulation by half. The final configuration of the simulation can be seen in Figure 3.5.
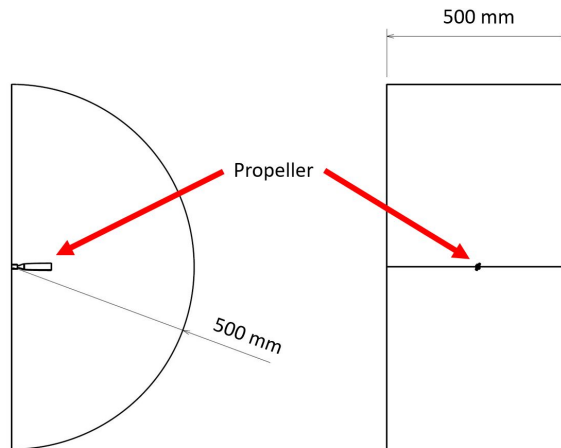
Figure 3.5.: DA4002 propeller in the wind tunnel.
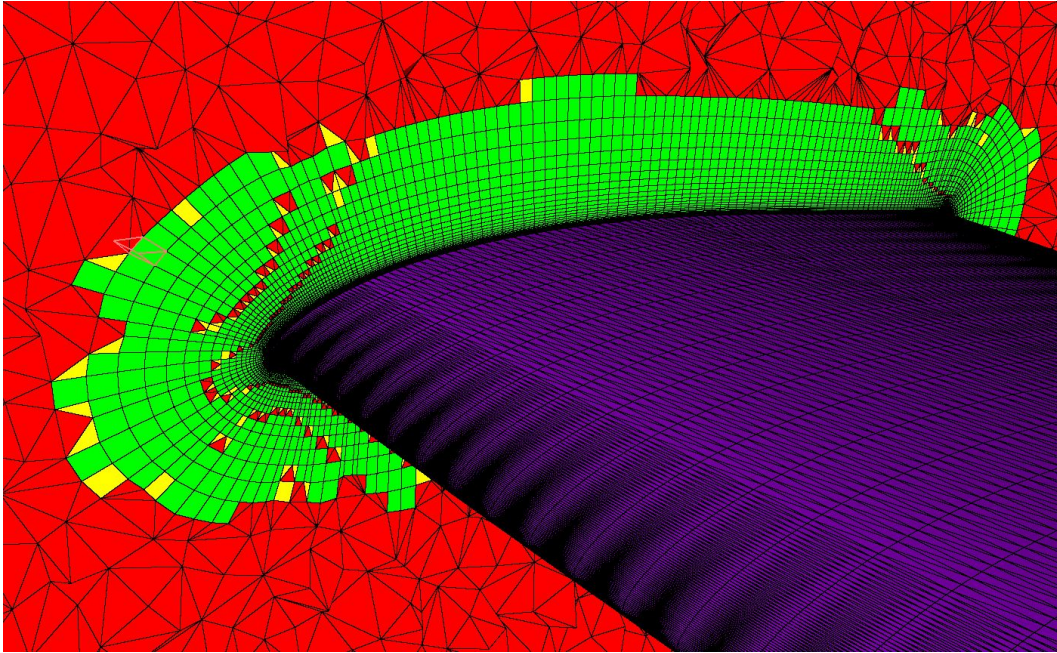
Figure 3.6.: Slice of the mesh of the DA4020 propeller.

Simulation Setup

To simulate the airflow, a hybrid volume mesh was created using Pointwise. All grids consist of a structured prism mesh over the surface of the Propeller, and an unstructured tetrahedral Mesh in the farfield. The surface mesh on the propeller is a diagonalized structured mesh. Only the mesh in the front of the tip and the hub is an unstructured triagonal mesh. To estimate the influence of the grid on the simulation, a grid influence study has been performed. For this reason three grids have been created, with different amounts of grid refinements. The grids have a different amount of chordwise cells over the propeller. The settings for the different grids can be seen in Table 3.1.

Parameter	Grid A	Grid B	Grid C
Spanwise cells	100	120	120
Chordwise cells	93	129	166
Prism Cells	$2,116,871$	$3,215,833$	$3,947,038$
Farfield Cells	$4,247,629$	$5,369,395$	$5,775,871$
Total Cells	$6,364,500$	$8,585,228$	$9,722,909$

Table 3.1.: Grid refinement study on the DA4002 mesh.

For all grids the amount of cells on the farfield of the simulation was kept the same. This is the reason, why the amount of cells is not growing linear with the amount of chordwise cells.

3.2.2. NACA0012

To validate the ice accretion on a rotor, the ice accretion on a helicopter rotor with a NACA0012 airfoil was analysed. The NACA0012 airfoil can be seen in Figure 3.7 The rotor has a constant chord of 266 mm and a radius of 2.74m. The rotor was tested in a cylindrical testing chamber with a radius of 3m. The airfoil of the rotor can be seen in Figure 3.7. The thickness of the trailing-edge was changed to a thickness of 1 mm in XFOIL.
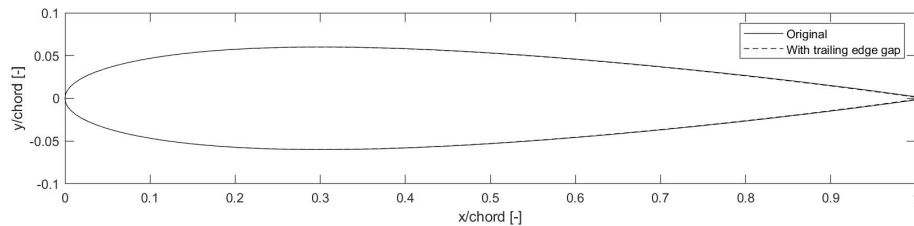

Figure 3.7.: Original NACA0012 airfoil [6] and with the trailing edge gap.

Simulation Setup

For this simulation, the rotor was set in a round test chamber with a rectangular testing section. The outer wall represents the fixed outer wall of the test chamber. This testing chamber is stationary. The real test stand is 3.5 meter high, but because the pitch of the blade at the test is zero, no velocity along the axis of rotation is to be expected, so the height of the computational domain in this simulation is 1 meter. The Setup of the orignal AERTS Facility can be seen in Figure 3.8. The walls at the top and the bottom, as well as the center of the simulation are calculated as no slip walls. The outer wall and the rotor are set as standard walls. The ice accretion is only calculated on the rotor. The setup of the simulation can be seen in Figure 3.9 and Figure 3.10. The hub of the Propeller is not calculated. A cylinder with no-slip walls is used as a stand in for the hub of the propeller. The reason for this setup is the reduced number of cells in the simulation. The amount of cells on the wall of the propeller is very important for the amount of cells in the mesh, as it has the smallest cell sizes and prism layers. To calculate the rotation of the fluid, the air needs to be kept stationary in the simulation chamber. For this reason, in front of the propeller is a outlet, and behind the propeller, there is a outlet. The velocity of the inlet is set to 0 m/s in an absolute coordinate system. Another system would be to calculate the full chamber and to use the sides and top an bottom of the simulation for the momentum transfer into the air. This was not done, as this would require the full experimental chamber to be calculated. this would have lead to a cell count too large for the remesher, due to virtual memory constraints on the computational cluster. Furthermore does the experiment chamber have stationary surfaces, which are not tangential to the rotational velocity of the propeller. This surfaces cannot be calculated using the used method for the calculation of the rotation.

For the icing simulation, the initial grid was created in Pointwise, and the volume is remeshed using ANSYS FLUENT. To enable the optimized mesh setup during the remeshing step, the
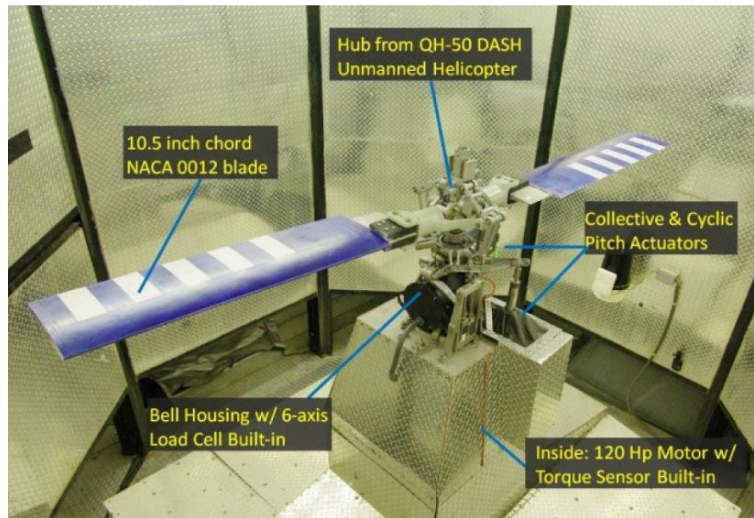
Figure 3.8.: AERTS facility with the rotor [7].
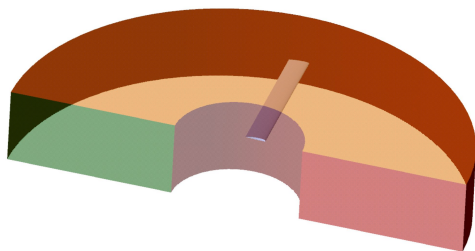
Figure 3.9.: Model of the NACA0012 in the simulation wind tunnel.
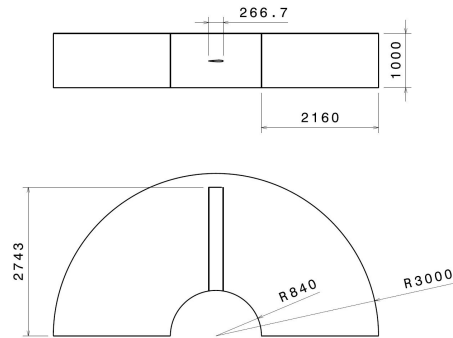
Figure 3.10.: Drawing of the simulation wind tunnel of the NACA0012 rotor.

surface of the propeller is split up into 6 boundaries. At the leading-edge of the rotor, two boundaries have been created, covering the first 10% of the chord of the airfoil. Because on the ice accretion is focused on this areas, the resolution for this regions is refined. A overview over the refinements on the mesh are given in Table 3.2.

3.2.3. PX-31 Falk propeller

Geometry

In this thesis, the propeller of a medium sized UAV was analyzed. The UAV for which this propeller is intended, is the Maritime Robotics PX-31 Falk. It has a wing span of 3.2 meters, a cruise velocity of 25 m/s and can carry a payload of up to 7 kg [10]. The performance data for the PX-31 can be seen in Table 3.3. The PX-31 Falk is intended for long-range and surveillance

Boundary	Boundary Condition	Max. Cell size [mm]
Leading-Edge Top	Wall	1
Leading-Edge Bottom	Wall	1
Top	Wall	15
Bottom	Wall	15
Trailing-Edge	Wall	1
Tip	Wall	1
Inlet	Velocity Inlet	75
Outlet	Pressure Outlet	75
Farfield Walls	No Slip Wall	75

Table 3.2.: Remeshing settings for the NACA0012 rotor.

missions. Those missions could include research in the Arctic, thus requiring the operation under adverse weather conditions including atmospheric icing.

Parameter	Value
Wing span	3.2m
Empty weight	15.0kg
Payload	7.0kg
Max. altitude	20000ft
Cruise speed	25m/s
Flight time	1.5-12h

Table 3.3.: Parameters of the PX-31 Falk [10].

The PX-31 Falk by Maritime Robotics is using a propeller by Mejzlik. Mejzlik has provided us with a model for a comparable propeller. The propeller for this UAV has a diameter of 0.533 m and a pitch of 0.254 m. The name of the propeller is the 21x10 EL. The shape of the propeller can be seen in Figure 3.11.

Figure 3.11.: 3D model of the Meijzlik 21x10 EL propeller.

266.5 mm

Figure 3.12.: Drawing of the Meijzlik 21x10 EL propeller.

To improve the mesh quality for the CFD calculations, the trailing-edge has been thickened to 0.5 mm using CATIA Version 5.19 [41]. The trailing-edge has been symmetrically extended, and at the blunt edge was blended during the last 80% of the chord of the propeller. In Figure 3.13 the airfoil of the propeller can be seen at 75% of the radius. The airfoil in the CFD Simulation is shown as a dashed line. To analyse the shape of the propeller, the chord and twist angle of the propeller has been calculated in 13 positions along the shape of the propeller. The twist and chord distribution can bee seen in Figure 3.14.
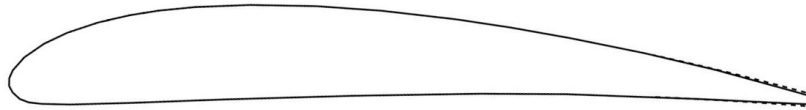
Figure 3.13.: Airfoil of the Meijzlik 21x10 EL propeller at 75% of the radius.

Because no performance data is available for this propeller, and no ice accretion experiments have been performed, another geometry had to be calculated to be used for the validation of the calculations.

Simulation Setup

The propeller was put into a cylindrical test chamber to calculate the performance and the ice accretion of the propeller. For both calculations only half of the propeller was simulated to reduce the amount of calculated cells. For the propeller of the PX-31 Falk, two different grids were produced. The first grid is the performance calculation grid. This grid was produced in
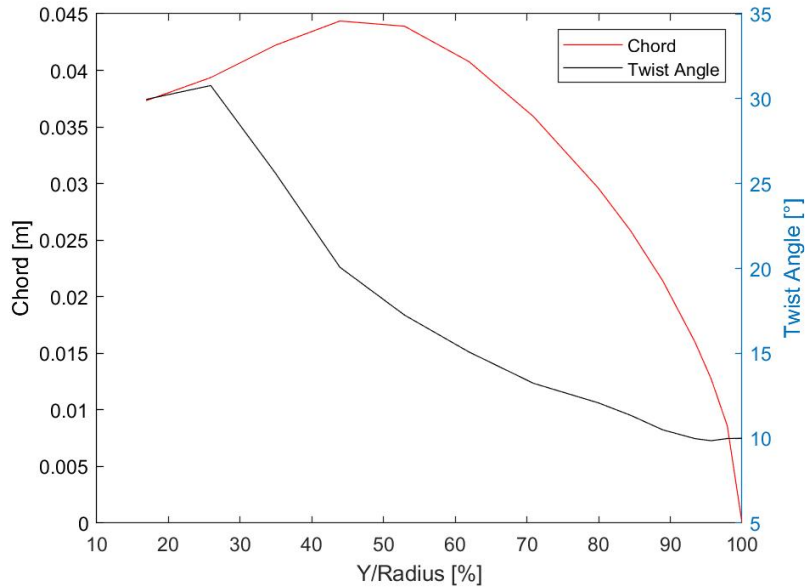
Figure 3.14.: Twist and chord distribution of the Meijzlik 21x10 EL propeller.

Pointwise. This grid is based on the grid setup developed in 3.2.1. The surface of the propeller is represented by a structured grid, that has been diagonalized to improve the interface between the prism layers and the outer tetrahedral mesh. The tip of the propeller is rounded. For this reason, the tip cannot be recreated in a structured mesh without creation cells with a low quality. For this reason, the structured grid ends at 98% of the radius of the propeller, and the last two percent are simulated using a structured mesh.

For the icing simulation, the simulation setup has also been changed, to use a cylinder at the center of the propeller. This was done for the calculation of the icing of the icing on the hub of the propeller. As the ice accretion on the hub of the propeller changes the shape of the propeller that has to be remeshed. Because of the periodicity condition between the two interfaces, this ice shape will be symmetrical. But during the wrapping operation in ANSYS FLUENT, the interfaces can become asymmetrical, what will prevent the proper setup of the periodic interface. For this reason a cylinder with a radius of 10% of the radius of the propeller was set at the center of the simulation domain. The hub of the propeller is attached to the cylinder, and thus does not touch the interface directly.

The simulation setup is similar to the setup of the NACA0012 rotor. The surface of the propeller is also divided into different boundaries. Because the propeller does not have a sharp edge at the tip of the propeller, the tip boundary covers the outer 2% of the radius of the propeller. The boundary at the leading-edge covers the first 20% of the chord. The length has been extended, because the stagnation point of the air on the airfoils changes with the radius of the propeller and the advance ratio of the propeller. The chord of the propeller changes, as well as the airfoil of the propeller. For this reason, the cell size has to decrease towards the tip of the propeller to allow for a proper resolving of the leading-edge. In the performance calculation mesh this happens atomically, as with a structured mesh the amount of chordwise cells stays constant. Because the ice accretion mesh is at the surface a isotropic mesh with triangular cells, the refinement of

the leading-edge of the outer 25 has been increased. in order to resolve this this area has been separated into its own boundaries. The boundary condition setup and the maximal cell sizes for the different boundaries can be seen in Table 3.4.

Boundary	Boundary Condition	Max. Cell size [mm]
Leading-Edge Top	Wall	0.5
Leading-Edge Bottom	Wall	0.5
Leading-Edge Top Tip	Wall	0.2
Leading-Edge Bottom Tip	Wall	0.2
Top	Wall	5
Bottom	Wall	5
Trailing-Edge	Wall	0.2
Tip	Wall	0.2
Outside	No Slip Wall	10
Center	No Slip Wall	10
Inlet	Velocity Inlet	10
Outlet	Pressure Outlet	10

Table 3.4.: Remeshing settings for the NACA0012 rotor.

3.3. Meteorological conditions
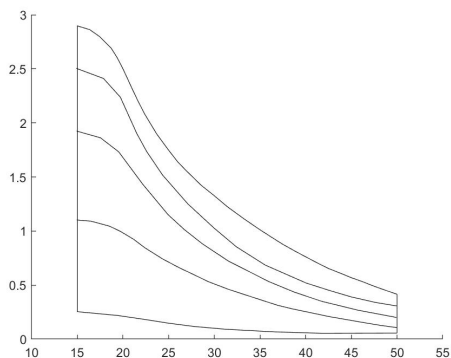
Figure 3.15.: Intermittent maximum envelope adapted from [8].
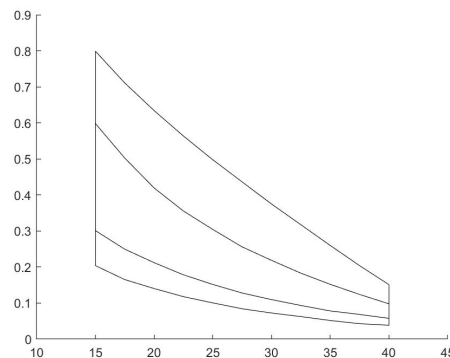
Figure 3.16.: Continuous maximum envelope adapted from [8].

The Federal Aviation Administration (FAA) defines two different icing envelopes for athmospheric in-cloud icing for manned aircraft in 14 CFR Part 25 appendix C [8].

The continuous maximum represents the icing conditions in a Stratiform cloud, with a extend of 17.4 nautical miles or 32.2 kilometers. This envelope is valid for flight altitudes from Sea level to 22 000 ft. The intermittent maximum represents the icing conditions in a Culmiform cloud. This cloud has an extend of 2.6nm and the envelope is valid at altitudes from 4 000 ft to 22 000

ft. In this thesis, the continuous maximum was chosen, because it covers lower altitudes, where a large percentage of the UAVs are operated. The meteorological conditions chosen in this thesis can be seen in Figure 3.17 and in Table 3.5. The MVD of 20 μm was chosen because Fajt et al. found in [42] the conditions at a MVD of 20 μm and a temperature of -2°C to be the worst-case for the icing of the wing of the PX-31 Falk. Therefore, three different temperatures at a MVD of 20 μm have been chosen for this thesis.
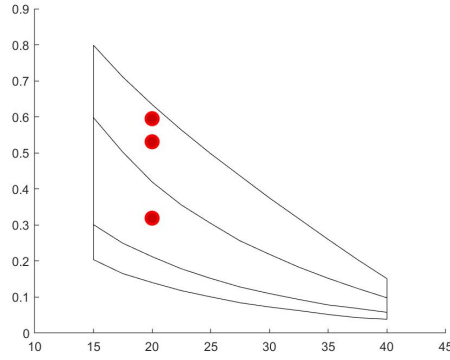
Figure 3.17.: Meteorological points in this thesis compared to the continuous in-flight icing envelope of the FAA [8].

Point	Temperature	MVD	LWC	Velocity	Duration
Point 1	-2 °C	20 μm	0.60 g/m^3	25 m/s	120 s
Point 2	-5 °C	20 μm	0.53 g/m^3	25 m/s	120 s
Point 3	-15 °C	20 μm	0.32 g/m^3	25 m/s	120 s

Table 3.5.: Icing conditions used in this thesis for the icing of the propeller of the PX-31 Falk.

4. Results

In this part, first the performance calculation and the ice accretion simulations are validated for the use for rotors on UAVs. Afterwards, the simulation methodology is applied to the calculation of a UAV propeller. The discussion of the results will be performed in Chapter 5.

4.1. Performance calculations

The first step is the calculation of the clean performance of a propeller. For this, the DA4002 propeller developed by Deters in [5] is used. This propeller was chosen because of the availability of the geometry and the experimental results data. Because this propeller has a much smaller diameter, the Reynolds number of the propeller is lower at 70.000, compared to the propeller of the PX-31 Falk with a Reynolds number of 200.000. This means that the viscous effects on the propeller are different. But because of the lack of experimental data for propellers in the target Reynolds number, the propeller was chosen nevertheless.

4.1.1. Grid dependency study

First a grid dependency study was performed on the DA4002 propeller. For this study, three different meshes where created, with 93, 129, and 166 cells along the chord of the propeller, as can be seen in Table 3.1. Those three simulations were performed using a advance ratio of 0.65. This is a typical advance ratio for the flight of UAVs. All other simulation parameters have been kept. The simulation parameters can be seen in Table 4.1. The laminar turbulent transition has been calculated for all simulations using X-Foil and the transition is forced for all simulations.

Parameter	Value
Reynolds Number Re	50,000
Rotation speed n	5000 rpm
Free stream velocity u_∞	12.35 m/s
Pressure p	101325 Pa
Temperature T	288.15 K
Advance Ratio J	0.65

Table 4.1.: Simulation parameters for the grid dependency study.

The results of the grid dependency study can be seen in Figures 4.1 and 4.2. As neither the thrust coefficient C_T not the power coefficient C_P are showing a monotone trend, no Richardson-Extrapolation was performed to estimate the exact result [43]. For the thrust coefficient, all grids lie within 0.6% of each other, with grid A showing the largest deviation. For the power coefficient,

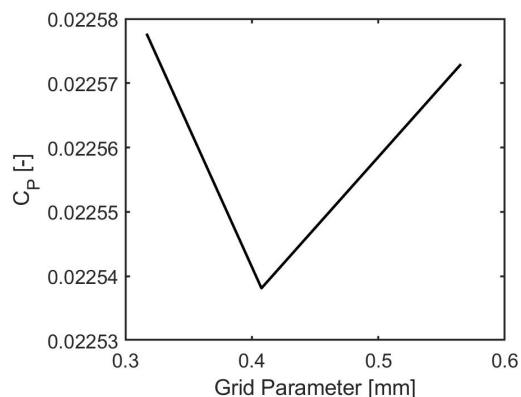all meshes lie within 0.2% of each other, with the grid B having the largest difference from each other.

Figure 4.1.: Power coefficient of the grid dependency study on the DA4002 propeller.
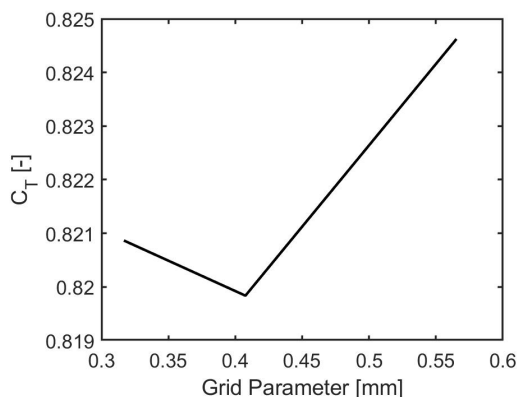

Figure 4.2.: Thrust coefficient of the grid dependency study on the DA4002 propeller.

Because the differences between all meshes are small, all meshes are seen as suitable in terms of accuracy. To decide for a mesh configuration, the simulation time was analysed. An overview over the simulation times is given in Table 4.2. Because this time is related to the number of cells in each simulation, the Grid A has the shortest simulation time. For this reason, the Grid A is used in the continuation of this thesis.

Grid	Time [h:m]
Grid A	3:24
Grid B	4:45
Grid C	5:16

Table 4.2.: Simulation times for the grid dependency study.

4.1.2. Performance analysis

In the next step, the performance of the calculation using the grid A was compared to the existing performance data gathered by Deters in [5]. An overview over the simulation parameters is given in Table 4.3. The simulated thrust of the grid A is 11.3% lower than the thrust of the experiment at a at a advance ratio of 0.65. One reason for the difference in the performance calculation could be the transition of the boundary layer from a laminar to a turbulent boundary layer. For the simulation, the transition point has been calculated for the expected flow at 75% of the radius using XFOIL with the e^n method using a critical n of 9. This transition point has been applied to the whole length of the propeller. In a real environment, the transition point changes over the radius of the propeller, and is dependent on the turbulence level. To evaluate the calculation of the performance of the propeller over a larger range, the performance has been calculated at three different advance ratios. In Figures 4.3 and 4.4, the Thrust and the power coefficient of the simulated propeller is compared to the experimental data gathered by Deters [5].

Parameter	Value
Reynolds Number Re	50,000
Rotation speed n	5000 rpm
Free stream velocity u_∞	5.7 - 13.3 m/s
Pressure p	101325 Pa
Temperature T	288.15 K
Advance Ratio J	0.3-0.7

Table 4.3.: Simulation parameters for the grid dependency study.
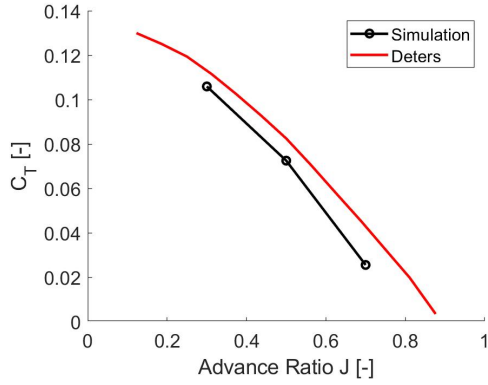

Figure 4.3.: Thrust polar of the DA4002 propeller compared to the experimental results by Deters [5].
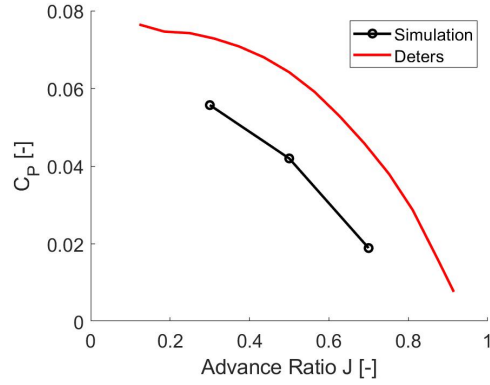
Figure 4.4.: Power polar of the DA4002 propeller compared to the experimental results by Deters [5].

The simulated thrust is constantly underestimating the thrust, compared to the experimental data. The power coefficient is also always underestimated. Both changes could be related to the reduced geometry of the hub of the propeller. In the real geometry, at the center of the propeller is a motor, the shaft of the propeller and the hub of the propeller. In the simulation, the hub is simulated using a cylindrical shape and the motor is not simulated at the simulation. In Figure 4.5, the turbulent viscosity is used to visualize the wake of the propeller, for the simulation of the Grid A at the advance ratio of 0.625. It is clear, the wake of the center of the hub of the propeller is visible. So changes here could be responsible for a part of the difference in performance. Because the hub is smaller than the propeller blades, it could facilitate the exchange of the air between the two sides of the propeller blades, and thus be responsible for the reduced thrust of the propeller.

Figure 4.5.: Visualization of the wake of the DA4002 propeller.

4.2. Ice accretion

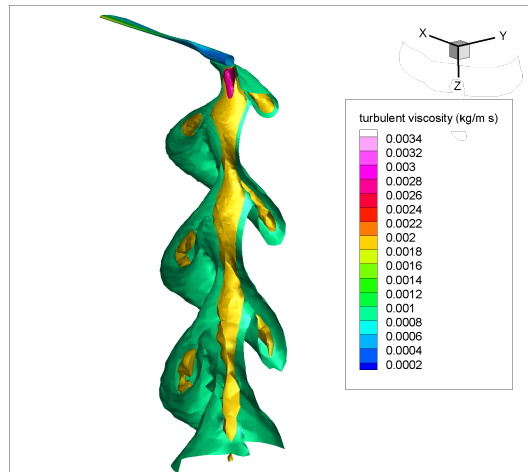For the validation of the ice accretion, the ice shape was calculated and compared to experimental results at two different icing conditions.

Because of the simulation of only one blade of the rotor, the effects of the wake of the rotor on the icing of the second propeller cannot be simulated. This simplification was necessary as the simulation of the full fluid domain would not be possible due to the memory constraints on the used computer. The settings for the simulation can be seen in Table 4.4.

Two cases are simulated, to test the simulation settings for two icing conditions. They represent typical glaze and rime ice shapes. For this reasons the Runs 3 and 4 were chosen to represent the glaze ice shapes. Two experimental runs were performed, to test the reputability of the experiments. The run 14 was chosen to represent a rime icing condition. The settings for the two simulations can be found in Table 4.5.

To compare the ice accretion of the experiment, the ice shapes at 95% of the radius have been compared.

The ice shape of the first case is represented well. For the case 1, the ice shape is a streamwise ice shape as it can be seen in Figure 4.6. The ice shape is indicative of rime ice, that freezes immediately onto hitting the surface of the airfoil. For this ice shape, the ice shape could be reproduced quite closely with the simulation. The general shape of the ice fits closely to the ice shape acquired in the experiments. The total extend of the ice seems to be close the experiment, which has a marginally larger icing extend at the leading edge of the airfoil. Therefore the simulation seems to be able to predict rime ice shapes. In case 2, the ice represents a mixed ice shape, where the central part is a glaze ice, with feathers outside. ANSYS FENSAP-ICE seems not to capture the ice shape. The most likely reason for this is an insufficient mesh size. The mesh size could be to large, to resolve all the feathers in the ice shape in this case. The large difference in the area of the predicted ice shape to the measured ice shape could also have other reasons. To validate the proper settings of the multi-shot simulation, the calculation was done in one step, to verify whether the interactions between the ice shape and the airflow had any

36

FENSAP	
Turbulence model	Spalart Allmaras
Boundary layer	Fully turbulent
CFL number	200
Max. number of timesteps	300
Artificial viscosity	Second order streamline upwind + cross-wind dissipation $1 \cdot 10^{-7}$
DROP3D	
Physical model	Droplets
Particle Type	Droplets
Droplet drag model	Water - default
Body forces	Rotation
Droplet distribution	Monodisperse
Boundary layer	Fully turbulent
CFL number	20
Max. number of timesteps	120
ICE3D	
Ice - Water model	Glaze Advanced
Roughness Output	Sand-grain from beading
Body forces	Rotation
Time step	Automatic
Multi-shots	10

Table 4.4.: Common parameters for the ice accretion study.

Simulation	Comparison Run	Temperature	Rotational Speed	MVD	Time
Run 1	AERTS 14	-15.4°C	412 rpm	28 μm	4.1 min
Run 2	AERTS 3/4	-8.3°C	492 rpm	26 μm	4 min

Table 4.5.: Settings for the ice accretion runs

influence on the ice accretion. The results of the calculation in one step can be seen in Figure 4.8. The results show, that the total ice mass stays similar, but the difference in the extend of the ice shape can be seen. The simulation with multiple iterations creates an ice shape that has a small size at the front of the airfoil, and more Ice has accumulated on the top and bottom of the airfoil, leading to a thicker ice shape after 1% of the chord-length of the clean airfoil. The change in the airflow around the rotor will influence the ice accretion process. Because this is not regarded in the single step simulation, the ice shape in the single step simulation is more streamlined.

The reasons for the large difference in the ice shape between the simulation and the experiment could be the difference in the geometry. In the simulation only the blade from 50% of the radius outward is represented. Because of the centrifugal forces of the rotation, water in the center
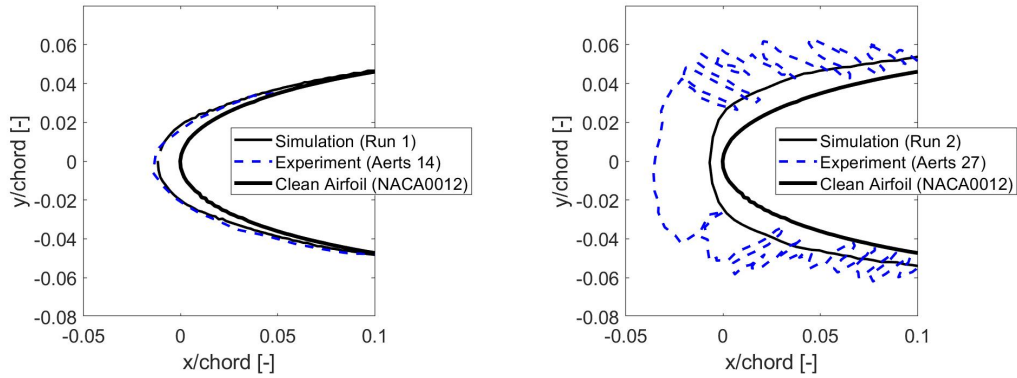
Figure 4.6.: Ice shape of ice accretion validation case 1.

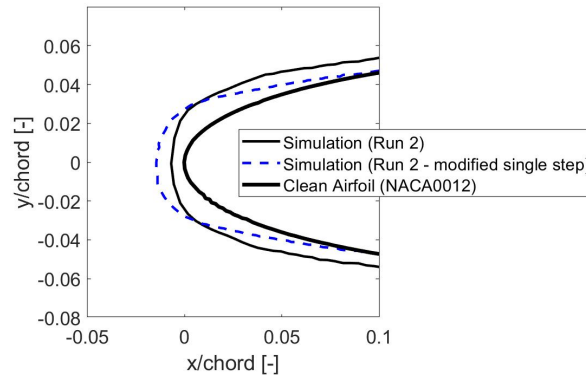**Figure 4.7.:** Ice shape of ice accretion validation case 2.

Figure 4.8.: Ice shape of ice accretion in the validation run 2 compared to a simulation with one icing step.

will flow outward before freezing. Therefore, the thickness of the ice in the outer parts of the rotor will increase. Another reason could be the feather shape of the ice outside the center. This cannot be represented in the simulation, because the chosen mesh resolution and the amount of icing steps is insufficient. The mesh on the surface of the NACA0012 rotor after 10 icing steps can be seen in Figure 4.9. Glaze ice is always more complicated to simulate correctly, as the heat transfer needs to be calculated in higher detail, compared to a rime ice shape [2] and [44]. In a future work the proper resolution could be achieved by only simulation the flow on a small slice of the rotor, and disregarding the rotation, in order to find the proper resolution for the ice shape. Because this mesh setup would be very dissimilar to the mesh of the propeller which is the main part of this thesis, this was not done as a part of this thesis.
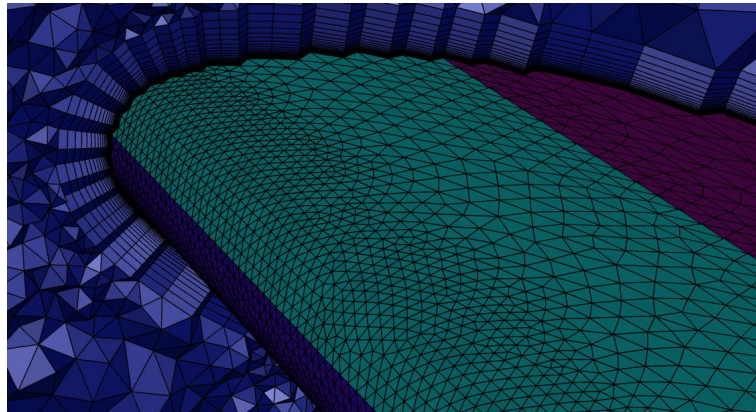
Figure 4.9.: Mesh of the iced NACA0012 Airfoil in simulation run 2.

4.3. Propeller of the PX-31 Falk

4.3.1. Ice accretion

The settings for the ice accretion studies can be seen in Tables 4.6 and 4.7 and 4.8. The results show that the temperature has a large influence on the ice shape of the propeller.

Temperature -2°C

The ice shape at a temperature can be seen in Figure 4.10. Ice accretion has only happened in the central part of the propeller. The tip of the propeller is almost ice-free. This is due to the increase of the stagnation temperature by the rotation of the propeller. At the simulated rotational speed of the propeller, the speed of the tip of the propeller is 139.6 m/s. This equates to a Mach number of 0.41. At this speed, the temperature of the air at the stagnation point rises to temperatures above 0°C This can be seen in Figure 4.11. Therefore no ice accretion at the leading-edge of the airfoil is observed close to the tip of the propeller. Behind the leading-edge, the friction between the propeller and the air is heating up the air and is preventing the ice accretion. Closer the the center of the propeller, friction heating is low, and therefore ice can accrete at the center of the propeller. The ice forms a span-wise horn, starting at 92% of the radius which is growing inwards. At less than 48% of the radius of the propeller, ice start to accrete at the top of the propeller. The ice shape is typical for a glaze ice shape. In Figure 4.10 the ice shapes can be seen in comparison to the clean airfoil. The contour of the geometry is given for the ice shape at 50%, 80% and 90% of the radius of the propeller. On the bottom left image, the detail of the ice shape in at the leading-edge of the propeller is given. The ice shape is colored in white, while the propeller is grey in the image. Additional contours and views can be seen in Figures B.1 and B.2.

Temperature -5 °C

The ice shape at a temperature of -5°C can be seen in Figure 4.12. A this temperature, the ice accretion happens along the whole propeller. For the same reasons as with the -2°case, the

FENSAP	
Turbulence model	Spalart Allmaras
Boundary layer	Fully turbulent
CFL number	350
Max. number of timesteps	500
Artificial viscosity	Second order streamline upwind + cross-wind dissipation $1 \cdot 10^{-7}$
DROP3D	
Physical model	Droplets
Particle Type	Droplets
Droplet drag model	Water - default
Body forces	Rotation
Droplet distribution	Monodisperse
Boundary layer	Fully turbulent
CFL number	20
Max. number of timesteps	120
ICE3D	
Ice - Water model	Glaze Advanced
Roughness Output	Sand-grain from beading
Body forces	Rotation
Time step	Automatic
Multi-shots	10

Table 4.6.: Setup parameter study for the simulation of the iced propeller performance.

Parameter	Value
Reynolds number Re	50,000
Rotation speed n	5000 rpm
Free stream velocity u_∞	25 m/s
Static pressure p	95 500 Pa
Temperature T	0° C
Advance Ratio J	0.65

Table 4.7.: Setup parameter study for the simulation of the iced propeller performance.

stagnation point of the propeller is mainly ice free from 75% of the radius outward. The ice once again shapes two span-wise horns. The horn at the top of the propeller starts at 87%of the radius and the horn at the bottom starts at 98% of the radius of the propeller. This is a typical ice shape for glaze ice. The ice shapes can be seen in Figure 4.12. Additional contours and views can be seen in Figures B.3 and B.4.

In Figure 4.13, the icing contour at 74% and 75% of the radius are compared. Here the difference

Run	Temperature	Rotational Speed	MVD	Time
Run 1	-2°C	5000 rpm	20 μm	120 s
Run 2	-5°C	5000 rpm	20 μm	120 s
Run 3	-15°C	5000 rpm	20 μm	120 s

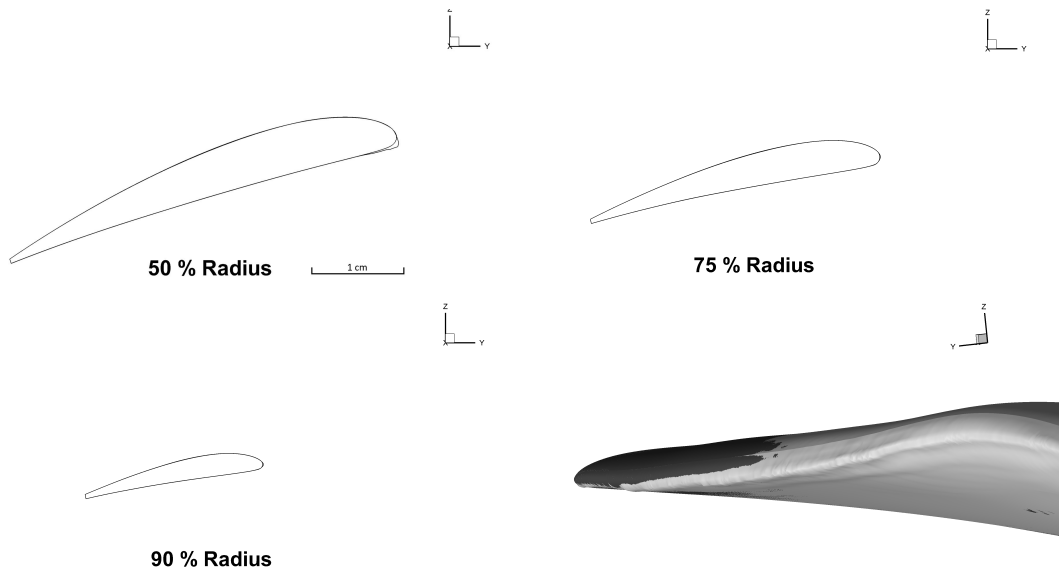**Table 4.8.:** Settings for the ice accretion runs.

Figure 4.10.: Ice shapes of the ice accretion Case 1 at -2°C on the propeller of the PX-31 Falk.
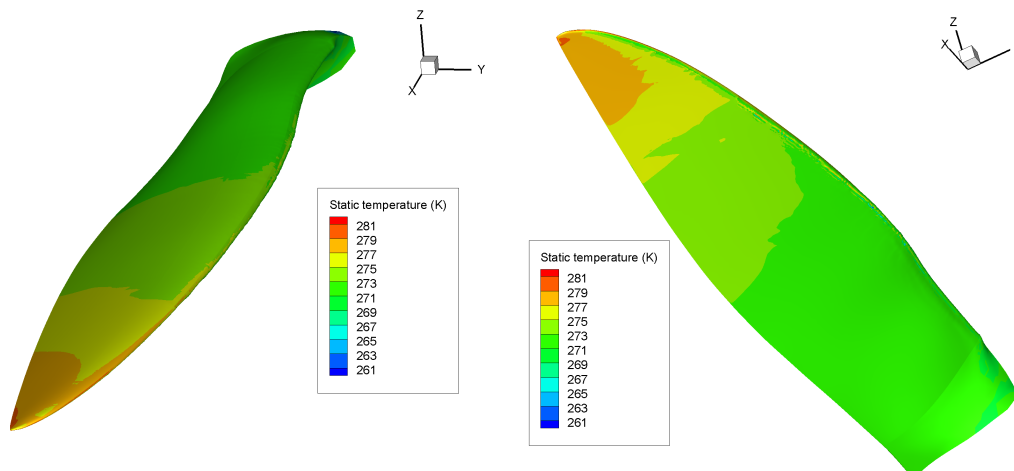

Figure 4.11.: Surface temperatures of the propeller of the PX-31 Falk in simulation Run 1 at -2°C.

small differences in the choice of the cut plane for the contours makes can be seen clearly. The
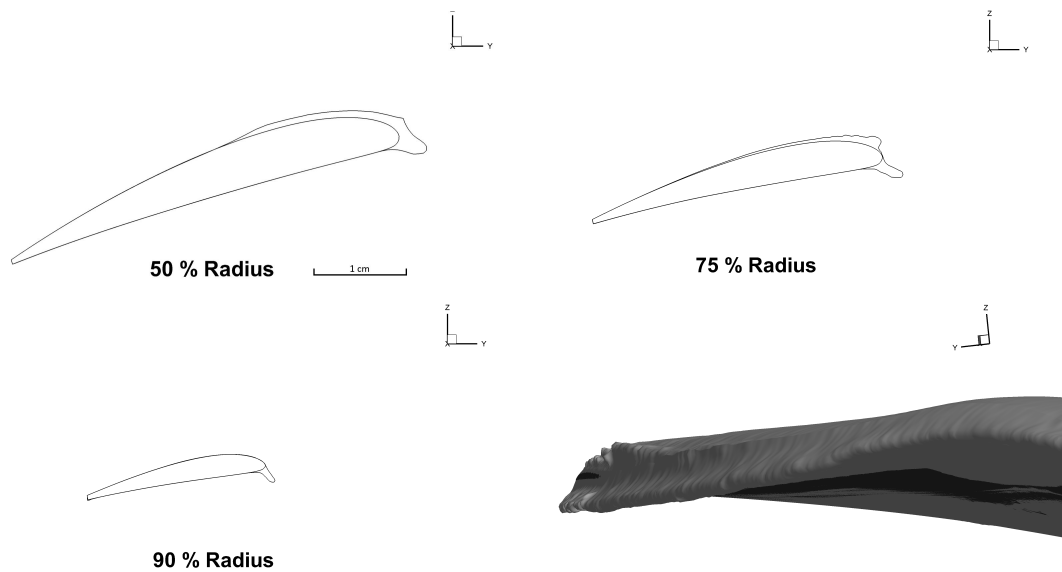
Figure 4.12.: Ice shapes of the ice accretion simulation run 2 at -5°C on the propeller of the PX-31 Falk.

Cut at 74% of the radius shows two horns, while the height of the spanwise horn at the top of the propeller is smaller at 76% of the radius.

Figure 4.13.: Ice shape at 74 % and 76% of the radius on the propeller of the PX-31 Falk in simulation run 2.

Temperature -15 °C

At a temperature of -15°C, the ice shape is very uniform, without the creation of horns. The ice shape can be seen in Figure 4.14 The full leading-edge of the propeller is covered in ice. This ice shape does represent a typical rime ice shape. The ice shape shows little change along the span of the propeller. The ice growth shows a great resemblance to the collection efficiency of the propeller. This happens, because most of the droplets freeze close to the point of impact with the propeller. The collection efficiency of the stagnation point is growing with the radius of the propeller and reaches a maximum at a radius of 91 %. The collection efficiency on the surface of

the propeller can be seen in Figure 4.15 The collection efficiency decreases, because the increased sweep angle of the propeller is decreasing the velocity of the air in the normal direction of the leading-edge of the propeller. The ice mass at -15°C is lower than the ice mass at -5 °C, because the LWC at -15 °C is lower, compared to the LWC at -5 °C. While at -15 °C , all water that hits the surface will freeze, a percentage of the impinging water at -5 °C 43% of the water will shed from the propeller, without freezing to the surface. Additional contours and views can be seen in Figures B.5 and B.6.
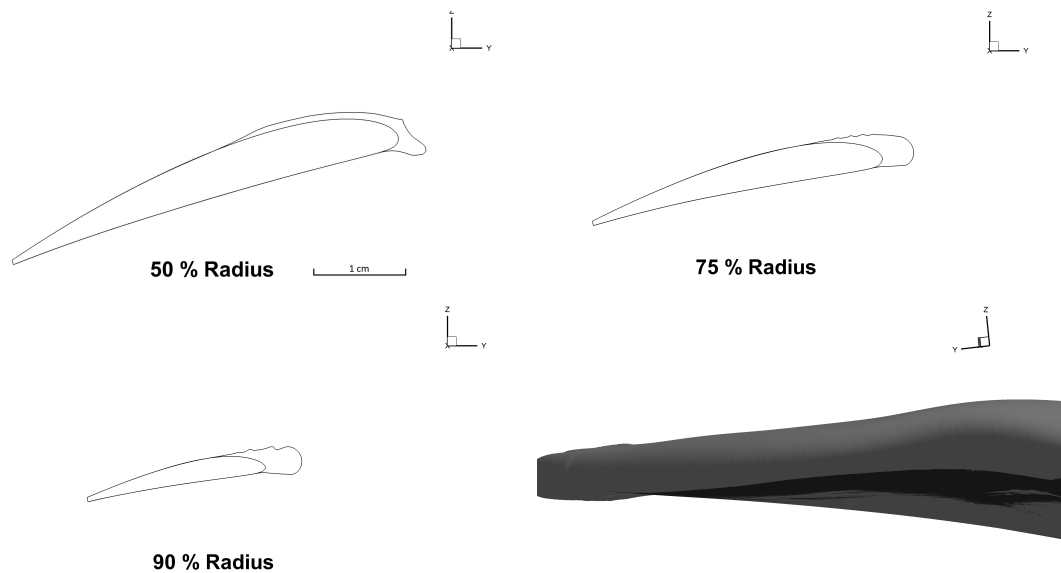

Figure 4.14.: Ice shapes of the ice accretion simulation run 3 at -15°C on the propeller of the PX-31 Falk.

Temperature	Ice mass [g]
-2 °C	16.5
-5°C	63.2
-15°C	62.8

Table 4.9.: Ice mass of the different ice accretion simulations.

4.3.2. Performance degradation

The performance of the propeller after the ice accretion was analyzed. For the final simulation, the aerodynamic properties of the iced propeller shapes were analysed. The final shape of the ice was taken, and remeshed in ANSYS Fluent. The aerodynamic performance of the propeller was analysed and compared to the simulation of the clean propeller. For the better comparison between the different icing conditions, all simulations have been conducted under the same conditions. This includes the temperature, which is set to 0°C. This means, that the different Reynolds numbers at the different temperatures at which the ice shapes have been formed are
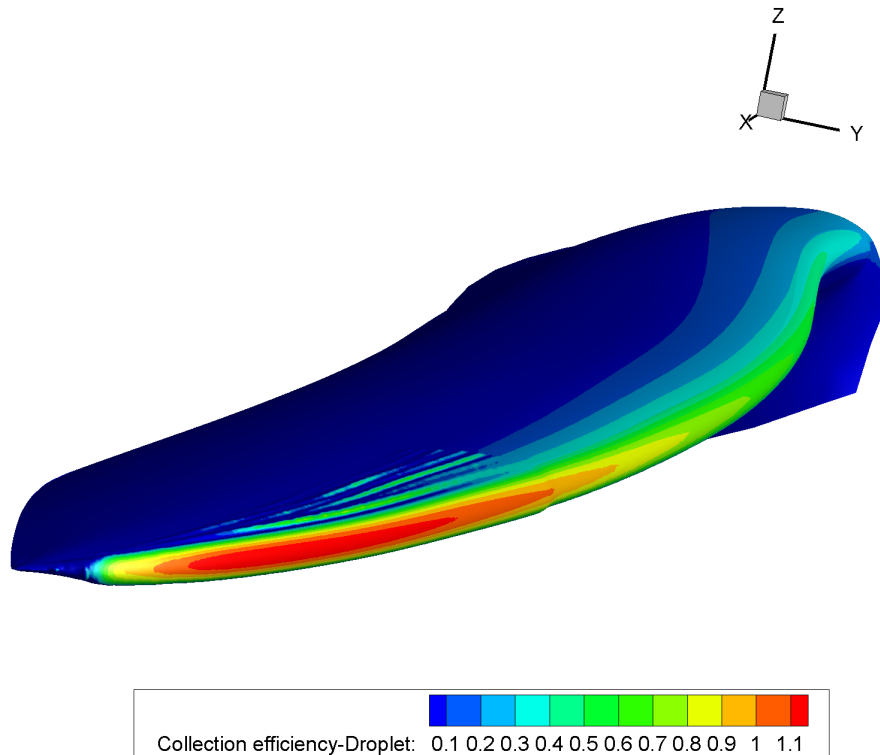
Figure 4.15.: Collection efficiency on the surface of the propeller in simulation run 3 at -15 °C

not regarded in the calculation of the aerodynamic properties. The simulation settings for this run can be seen in Tables 4.10 and 4.11.

FENSAP	
Turbulence model	Spalart Allmaras
Boundary layer	Fully Turbulent
CFL number	350
Max. number of timesteps	5000
Artificial viscosity	Second order streamline upwind + cross-wind dissipation $1 \cdot 10^{-7}$

Table 4.10.: Setup parameter study for the simulation of the iced propeller performance.

4.3.3. Clean propeller

First, the performance of the clean propeller was calculated. The values of the shear stress on the propeller can be seen in Figure 4.16. At the flight velocity of 25 m/s and a rotation rate of

Parameter	Value
Reynolds Number Re	50,000
Rotation speed n	5000 rpm
Free stream velocity u_∞	25 m/s
Static pressure p	95 500 Pa
Temperature T	0° C
Advance Ratio J	0.65

Table 4.11.: Simulation point for the performance calculation runs.

5000 rpm, the propeller produces 20.2 N of thrust, and requires 560 W of power from the motor.
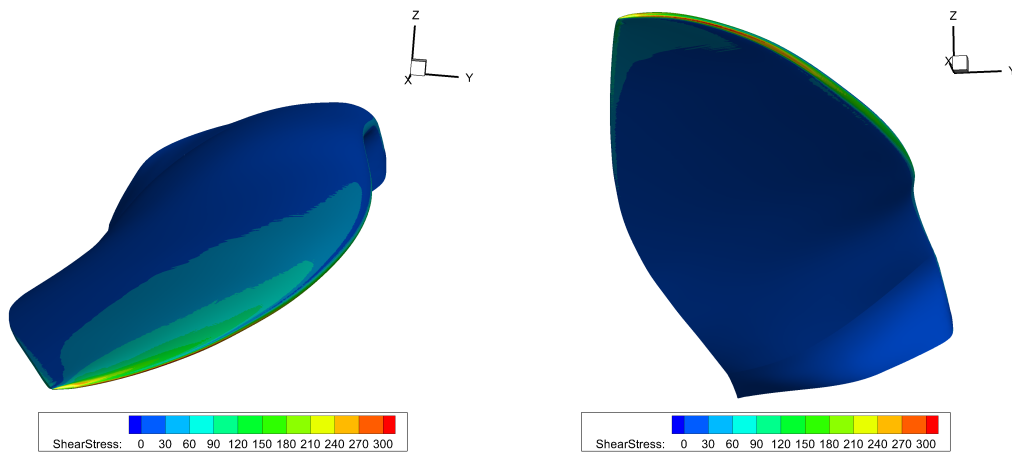

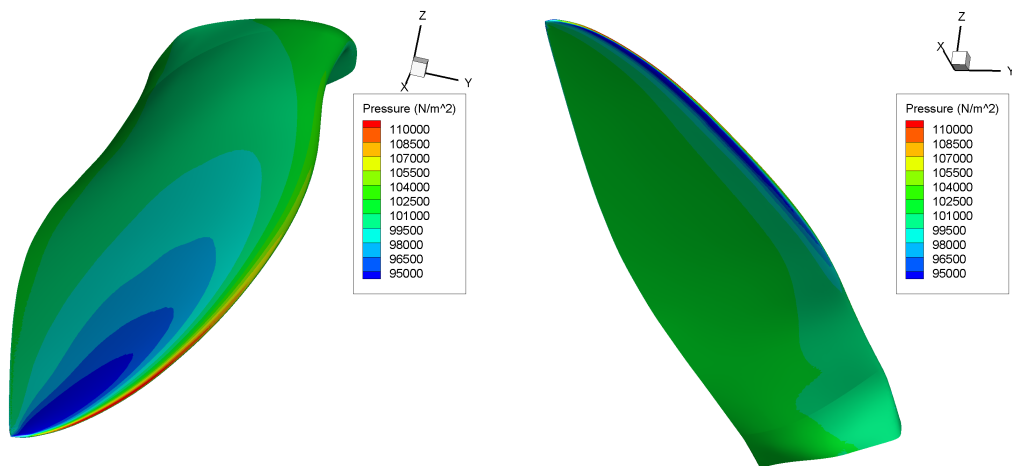**Figure 4.16.:** Shear stress on the clean propeller of the PX-31 Falk.

Figure 4.17.: Pressure on the clean propeller of the PX-31 Falk.

4.3.4. Temperature -2°C

At a temperature of -2°C, the least amount of ice has accumulated on the airfoil. This corresponds with the least amount of performance degradation compared to the clean configuration. This leads to a thrust reduction of 4.1% compared to the clean configuration. The power the engine has to provide to turn the propeller has increased by 9.1 %. The decrease in the thrust of the propeller is due to the reduced lift of the propeller. The lift is decreased by the accumulated ice, because the ice shapes disturb the airflow around the airfoil. This happens especially at the leading-edge of the airfoil. The flow around the airfoil can be seen in Figure 4.18. The ice shape created by the ice cause a large disturbance in the airflow and causes a large separation between the airflow and the propeller. While the separation at the center also occurs for the clean propeller, the large wake area in the middle of the propeller is created by the ice shape. The red surface is an iso-surface with a constant turbulent viscosity of 0.001 $N\,s/m^2$.
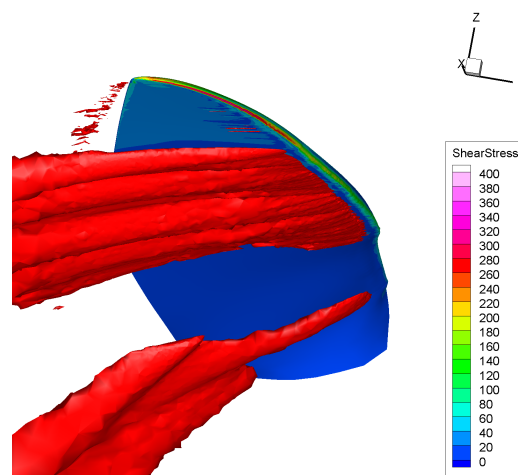
Figure 4.18.: Visualization of the wake of the propeller of the PX-31 Falk at -2 °C.

4.3.5. Temperature -5 °C

At this temperature, largest reduction in the performance of the propeller is observed. The thrust of the propeller is reduced by 46.7% and the power coefficient of the propeller is increased by 44.3%.This leads to a reduction in the efficiency of 62.9%, as calculated by Equation 2.10. This large decrease in the efficiency of the propellers is presumably caused by the large horns created in the ice shape. They disrupt the flow of the air and they decrease the thrust of the propeller. Because the angle of attack of the airflow at the propeller is dependent on the thrust of the propeller, because of the induced velocity of the propeller, a reduce in the thrust leads to a increase in the angle of attack of the propeller. Combined with the reduced stall angle of a iced propeller, this makes the propeller stall, which drastically reduces the thrust of the propeller. In Figure 4.19, the shear stress on the leading-edge of the propeller is shown, for the iced case, and the clean comparison case. It can be seen, that the ice is increasing the friction forces on the ice horns, and is thus decreasing the performance of the propeller. This comparison can be seen for all ice cases in Figures C.1, C.5, C.9 and C.13.
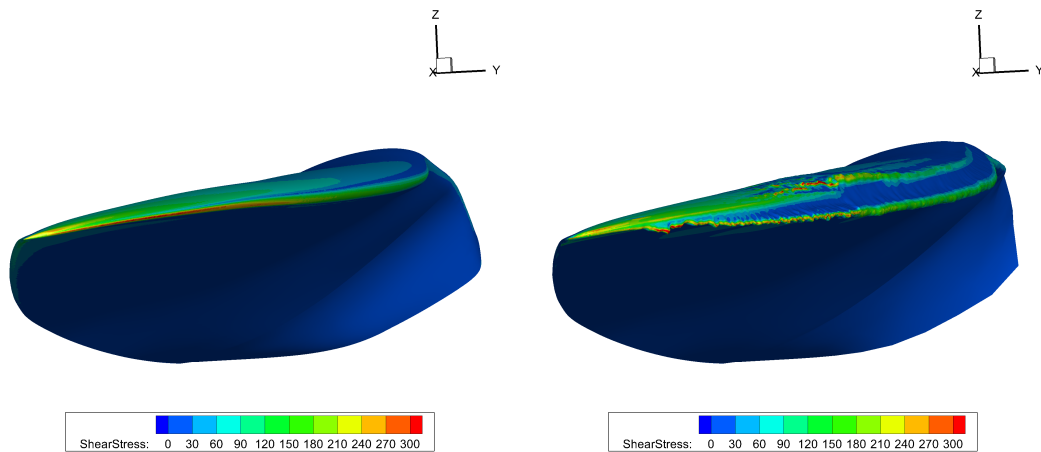
Figure 4.19.: Shear stress comparison between the clean propeller on the right and the propeller of icing Case 3.

4.3.6. Temperature -15 °C

At a temperature of -15°C, the ice has accumulated on the full length of the leading-edge of the propeller. The efficiency lost at this temperature is driven by the increase of the power coefficient by 29.5%, while the thrust has been reduced by 9.5%. The reason for this behavior is assumed to be the increase in the drag of the airfoil. The ice shape is streamlined, with very limited disturbances to disrupt the airflow over the propeller. For this reason, the thrust of the propeller is still similar to the clean propeller. The ice shape does however increase the area of the propeller substantially, and the airflow over the larger area does increase the drag of the propeller. Furthermore, the ice increases the thickness of the propeller, and increases the radius of the leading-edge of the propeller. Those two aspects contribute to an increase in the drag of the propeller. The larger area of the iced propeller shape does also have a positive influence on the thrust of the propeller.

4.3.7. Overview

The different temperatures had very different influences on the aerodynamic performance penalties of the propeller. The Table 4.12 given an overview over the different changes in the aerodynamic performances of the propeller. The Figure 4.20 given the plot of the changes of this values over the temperature. It is clear, that not only the total ice mass is relevant for the loss of efficiency, but also the shape of the ice.

Case	C_T change [%]	C_P change [%]	η change [%]
-2°C	-4.1	9.9	12.7
-5°C	-46.4	44.3	62.9
-15°C	-9.5	29.5	30.3

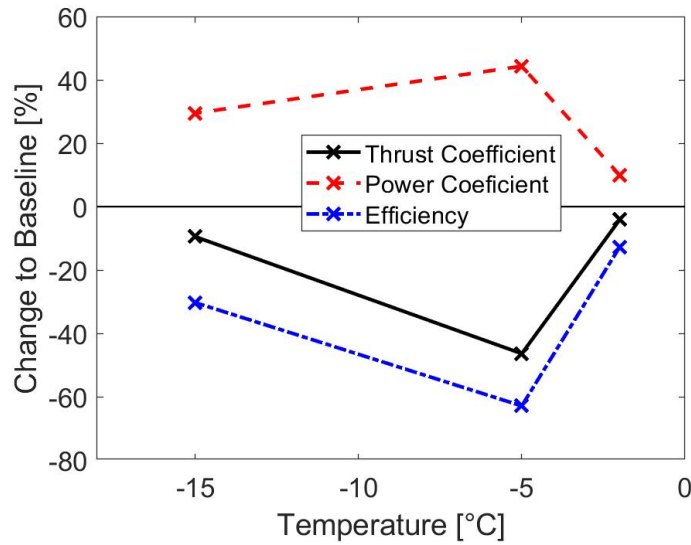**Table 4.12.:** Performance change compared to the baseline.

47

Figure 4.20.: Change of the aerodynamic performance of the propeller with for different temperatures.

4.4. Ice protection system loads

For the design of an ice protection system, the information about the required power is necessary. For this simulation, the conditions of the run with the lowest temperature was taken. The lower the ambient temperature, the higher the loads on the icing protection system, as is must heat the fluid-film to 0°C. For this reason, the case with the lowest temperature is the worst case scenario for the IPS. Two different conditions for the IPS System have been calculated. In the running wet condition, the temperature of the surface of the propeller is set to be 0 °C. The fluid hitting the surface may evaporate, or it may flow to the backside of the propeller, where it will shed back into the air. In the fully evaporative condition, the fluid needs to be evaporated within the impingement zone. This leads to a higher required heat flux by the IPS. Because the water will be evaporated within the impingement zone, the heated area is smaller. The power required by the IPS can be seen in Table 4.13. The required heat flux in fully evaporative conditions is 48% higher, while the maximum heat flux is 374% higher, compared to the running wet condition. The maximum heat flux is a key design criteria as it influences how much the layout of the heating zones. The distribution of the required heat flux can be seen in Figure 4.21. It is clear, that the IPS needs to be focused on the leading-edge of the propeller as here the maximum heat flux requirement is present. In the fully evaporative mode, only regions were water impinges the propeller need to be heated, while under running wet conditions the whole propeller needs to be heated, because the fluid will flow towards the back of the propeller. Without heating pads towards the back, the water will freeze there. The maximum load happens towards the tip of the propeller, as here the air velocities will be the highest. Because the extend of the maximum value for the heat flux is spatially limited, in real world situations, the maximum load provided by the IPS may be lower, as thermal conductivity of the surface will spread the heat flow. Furthermore, the leading-edge may be operated under running wet conditions, and the water will be evaporated further down the propeller.

Situation	Required power [W]	Maximum heat flux [kW/m^2]
Running wet	167.5	46.7
Fully evaporative	248.6	174.4

Table 4.13.: Results of the IPS load estimation from simulations at -15°C and a MVD of 20 μm.
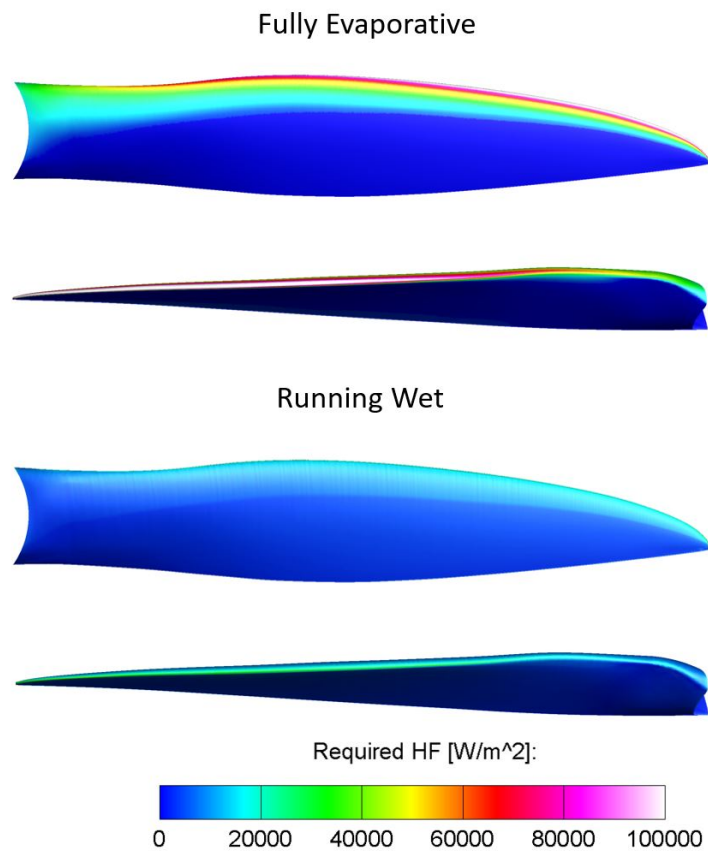
Fully Evaporative

Running Wet

Figure 4.21.: Results of the IPS calculations for the case 3 at -15 °C.

5. Discussion

In this section, the results of the previous sections are discussed and possible explanations for the phenomena are presented.

5.1. Ice accretion

The ice accretion on the propeller has been analysed in three different meteorological conditions, which produced three different ice shapes. At temperatures closer to the freezing point only minimal ice accretion and the creation of ice roughness has been observed. At lower temperatures, first a glaze ice shape with spanwise horns has been observed, and than at -15°C, the ice shape represented a stream-wise ice shape. Compared to an analysis of the icing of the wing of the PX-31 performed by Fajt et al. [42], the severity of the icing is different at the different temperatures. For the wing of the PX-31 Falk, 2 °C is the worst case icing temperature, while at -5 °C, the ice shape starts showing a stream-wise ice shape. The reason for the difference in the ice accretion between two different parts of the same aircraft is the increased friction of the propeller. The increased velocity of the airflow over the propeller compared to the wing increases the Mach number. The Mach number for the tip of this propeller is 0.4, while the Mach number of the wing is only 0.1. This increased Mach number leads to compressability effects playing a greater role for the airflow. For example the stagnation temperature increases with the increased Mach number of the propeller. For this reason, the temperature of the leading-edge of the propeller at -2°C is greater than 0 °C an thus no ice can form on the leading-edge of the propeller. Another reason is the friction heating of the air as is flows over the surface of the propeller. Therefore, the rotation speed of the propeller needs to be treated as a separate parameter in the ice accretion of a propeller. If the rotational speed of the propeller is reduced, the reduced Mach number would lead to a reduced stagnation temperature, and thus allow for the ice accretion even at higher temperatures. Another effect of the change in the rotational speed is the change in the Reynolds number. Decreased Reynolds numbers could lead to an increase in the heat transfer between the fluid film and the air, and thus increasing the glaze icing, compared to higher Reynolds numbers.

One effect that has been disregarded in the current analysis of the ice accretion is the ice shedding. This describes the process, where a part of the ice breaks of the main ice shape. This is a common phenomenon during the icing of propellers, as the high centrifugal forces and the vibrations caused by nonuniform ice accretion will increase the likelihood of ice shedding. For the analysis of the ice shedding, the adhesion forces of the ice on the surface and the cohesion forces inside the ice have to be calculated. Ice shedding can be dangerous, because the ice that is detaching from the propeller can hit the UAV, and cause damage to it. If the ice shedding does not happen symmetrically on all propeller blades, vibrations can be caused. This vibrations ca be caused by the mass imbalance between the propeller blades, or by the difference in the aerodynamic properties between the propeller blades, and the subsequent differences in the aerodynamic forces.
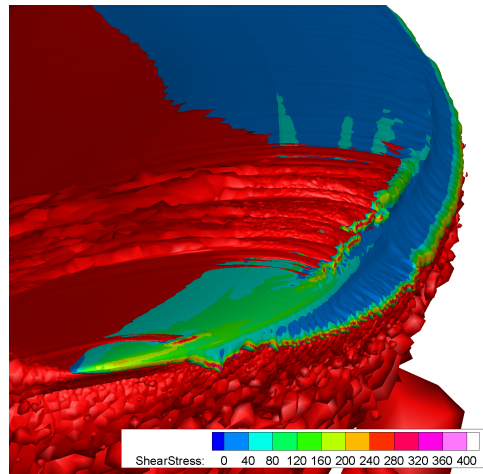
5.2. Performance simulation

Figure 5.1.: Detail image of the tip of the propeller at a temperature of -5°C.

Ice accretions have a large influence on the performance of the propeller. While the ice accretion and thus the performance degradation at a temperature of -2°C is comparatively low, the ice accretion at a temperature of -5°C is the largest, that has been found in the simulations. The most likely reason for this are the developed spanwise horns on the propeller. The influence of this horns is shown in Figure 5.1. Here an iso-surface of the turbulent viscosity is shown. This can be used, to differentiate between regions of low and high turbulence in the airflow. This can lead to an earlier detachment of the flow from the propeller, and thus reduce the aerodynamic performance of the propeller. It can be seen, that the spanwise horns on the bottom of the propeller lead to a detachment of the airflow over the propeller along the full length of the propeller. On the top, the horn shape is smaller, and thus the areas with high turbulent viscosity are smaller. If the shear-stress on the surface of the propeller is analysed, it can be seen, that the shear-stress on the surface of the propeller is significantly increased in the areas where ice is present. This increase in shear-stress will increase the drag of the airfoil, and thus decrease the thrust of the propeller as well as it will increase the required power to operate the propeller. The stream-wise ice shape that is present at -15°C has a smaller influence on the performance of the propeller. Here the main influence on the performance of the propeller is the increased drag of the airfoil, which leads to a reduced performance of the propeller. Because the mesh convergence study performed on the DA4002 propeller was not fully conclusive, and does not cover the iced propellers, a more detailed mesh convergence study needs to be performed in the future.

The ice accretion on the surface of the propeller has been analysed for a time frame of 120s. In reality, a UAV like the PX-31 Falk will need over 21 minutes to traverse even a stratiform cloud. This clouds are used as a reference of the continuous atmospheric icing envelope by the FAA [8]. So the maximum icing extend could be much larger, if the flight of the UAV through the icing conditions continues.

In a culmiform cloud used for the intermittent icing envelope, the LWC of the cloud is much larger, and therefore, the ice accretion could probably create a similar ice cover in significantly less than 120 s. A higher LWC is usually associated with ice shapes, that are more likely to be glaze ice shapes. Therefore, in most cases they will lead to an increase of the aerodynamic

performance penalties. In this thesis, a ice accretion time of 2 minutes was chosen, because the ice shapes already have a significant size, and the aerodynamic penalties are large. For many multi-rotor UAVs, a efficiency loss of 63% at the propeller might be enough, to reduce its flight capabilities beyond the minimum required for a stationary flight. Most fixed wing UAVs will also lose the ability to climb, or tho keep its altitude, especially, if the ice accretion on the rest of the UAV is taken into account.

5.3. Icing protection system

The calculation of the icing protection system loads presented in this work have not been validated against experiments, but the methodology used has been used to predict the required icing protection systems for the wings of UAVs by Hann et al. [2]. For this reason, they need to validated against the required icing protection system loads of a propeller in a future work. The results show, that to prevent the ice accretion on the propeller of an UAV, a very high maximum heat flux is required at the leading-edge of the propeller, especially towards the tip of the propeller. This heat flow could be created by electro-resitive heating elements in the leading-edge of the propeller. In this simulation the required heat flux was calculated without taking heat conductivity into account. To decrease the high maximal heat fluxes at the leading-edge, the propeller could be created from a material with a high thermal conductivity. Because the aim of the IPS is to heat the propeller to an uniform temperature, the effects of heat conduction can be used to distribute the heatflux from the heating element to the surface of the propeller.

For the development of an ice detection system, the increased power requirements of the propeller may be used. Any ice accretion on the surface of a propeller will lead to a direct increase of the required power to keep the rotational speed of the propeller constant. For most UAVs powered by electric motors [45], the power requested by the motor will already be monitored for the analysis of the remaining charge in the accumulator. The rotational speed of the propeller can either be monitored by an optical sensor, that reacts to a marking on the motor. Another option is to observe the voltage in the supply cables to the motor. Most modern UAVs will use brushless, electronically commutated synchronous motors. For this type of motor, the magnetic filed inside the motor is controlled by an external controller, and because the motor is synchronous, it will precisely follow this signal. Therefore, it can be used for the estimation of the rotational speed of the propeller. For UAVs powered by combustion motors, the ice accretion could be estimated by a correlation between the throttle setting and the propeller speed. Because the performance loss occurs at a rapid rate, an deicing system needs to be very fast in the detection and the removal of the ice.

To prevent the ice accretion, the knowledge of the severity at different temperatures and rotational velocities could be used. If an analysis would show a larger performance penalty for a low propeller speed at temperatures close to freezing, compared to a high speeds, the controller could increase the power to the propeller to prevent ice accretion. This could also be used at low temperatures, where a lower propeller speed might lead to a more favorable streamwise ice accretion, compared to a horn ice shapes at higher temperatures. To compensate for the different thrust, the controller could either change the speed of the UAV within the capabilities of the UAV, or initiate a climb or decent. This could be coupled with an advanced route-planning algorithm, to minimize the risk for the UAV flying in icing conditions, by leaving the cloud as soon as possible, with the least amount of icing related performance degradation.

Another mechanic a icing protection system, that an UAV could use to reduce the power re-

quirement, is the ice shedding. By operating the IPS intermittently, ice is allowed to accrete. After a certain amount of time, the IPS is activated. Now it only needs to melt enough ice on the surface of the propeller, until the centrifugal forces on the ice will lead to ice shedding. For such a system to operate effectively and securely, the ice growth on the surface of the propeller needs to be closely monitored.

5.4. Comparison with literature

There is only a very limited amount of experiments, that have been conducted, with which the results of the thesis can be compared. The ice accretions at the experiments on the ice accretion on a UAV propeller performed by Liu et al. [9], also showed a rapid ice growth at the leading-edge of the propeller, as it can be seen in Figure 5.2. The thrust coefficient did decrease in this cse, and the power coefficient did rise rapidly, as it can be seen in Figure 5.3. In the meteorological conditions that did not produce a glaze ice shape with spanwise horns, the reduction of the thrust coefficient was only small. This does fit to the findings of this work, as in this work also the thrust coefficient was seen to be reduced in the test case at -5 °C, while the power coefficient was rising in all cases.
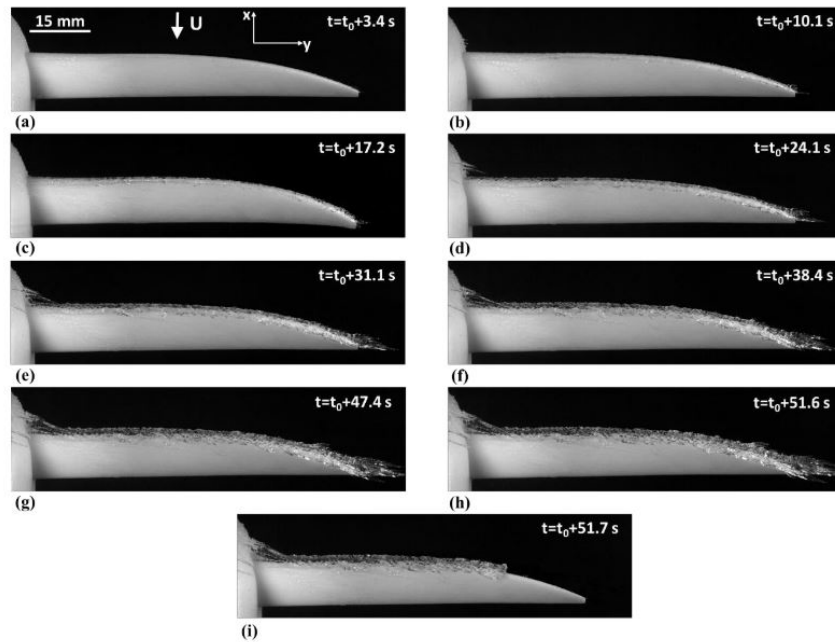

Figure 5.2.: Images of the ice accretion process on the rotating propeller blade at n = 3000 rpm with the freestream velocity, v = 16 m/s, LWC = 2.0 g/m^3 and t = -5 °C [9].
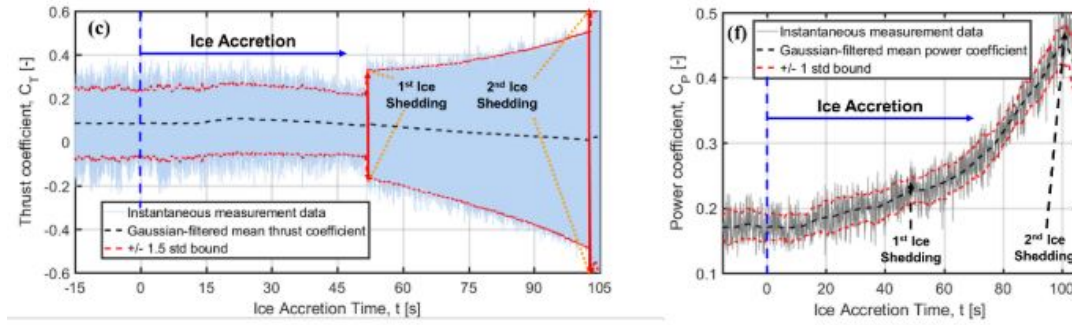
Figure 5.3.: Dynamic thrust and power coefficient of the propeller, v = 16 m/s, LWC = 2.0 g/m^3 and t = -5 °C [9].

5.5. Uncertainties

As described in the previous chapters, there is very little experimental data available for the validation of the simulation models. Therefore, the aerodynamic performance has been calculated using a test case with a much lower Reynolds number. The ice accretion on the other hand has been validated using a experiment with a much larger Reynolds number. Because the Reynolds number is different, the impact of the viscous forces can not be correctly verified. Furthermore, the mesh close to the wall of the simulations will be different. Because the height of the first prism cell is fixed by the maximum y_+ value, the height of the first cell is different. Furthermore the performance calculation of the iced calculation could not be validated. Here experiments for the performance of propellers with ice shapes need to be executed to validate the ice shapes.

In the cases analysed in this thesis, all droplets in the fluid had the same diameter. In most real cases, the droplets will have a range of different sizes, which could influence the shape of the ice. To analyze the influence of this setting, either further simulations with a droplet size distribution or experiments with a dispersed droplet distribution will need to be performed.

The ice accretion was only calculated using one advance ratio. In a real environment one would expect the rotational speed of the propeller to change and therefore, the advance ratio to change. This will be due to the reduced thrust created by the propeller and therefore the controller would increase the power to the propeller to keep the speed of the aircraft steady.

Only the propeller has been evaluated. Ignoring the influence of the fuselage can make a large difference. It is common for the propeller of a UAV to be in the so called pusher configuration, where the propeller is mounted behind the fuselage. In those cases, the fuselage will have a large influence on the ice accretion of the propeller. The smooth airflow before the propeller is disturbed, as the propeller operates for a large part inside the boundary layer of the propeller. Furthermore the droplet distribution will no longer be uniform behind the fuselage. Here a steady approximation will no longer be valid, as the flow conditions will be dependent on the angle of the propeller in its rotation. These uncertainties show that to increase the confidence in the simulations, more experimental data is necessary to validate the used simulation models.

5.6. Relevance

The analysis of the ice accretion of the propeller in different meteorological conditions is important for the development of icing protection systems for UAVs. For the wings of UAVs, a promising concept has been developed using an electro-thermal approach. This system is able to autonomously detect and remove ice on the wing of the UAV by operating intermittently to detect the ice accretion on the UAV. This work provides the groundwork to apply this system to the propeller of the UAV.

The identification of the -5°C / MVD 20 μm worst case icing condition for the propeller of the PX-31 Falk is important for the development of the IPS. This allows the future simulations and experiments to focus on the right simulation conditions. As it was outlined by Hann et al. in [20], the correct simulation point is one of the challenges in the development of IPS Systems for UAVs.

6. Conclusion

In this thesis, a process for the calculation of the ice accretion of the propeller of a small-medium UAV was developed. CFD simulations were used to calculate the ice accretion and the performance penalties of a propeller. The propeller in this thesis is a Mejzlik 21X10 EL propeller, used on the Maritime Robotics PX-31 Falk, a fixed-wing UAV with a wingspan of 3.2m.

Foremost, an overview over the existing icing experiments performed was conducted. During this, a database of 71 icing experiments was created. In this database, the icing experiments are divided into icing experiments that capture the impingement of the water on the surface, experiments that create the shape of the ice, and experiments for the performance degradation of the iced airfoil. Most of those experiments are focused on manned aircraft, and are done at Reynolds numbers above the typical Reynolds numbers of an UAV.

For the simulation of the ice accretion on a propeller, a process was developed using ANSYS FENSAP-ICE. This tool consist of different modules. The flow solver FENSAP is used to calculate the flowfield, utilizing the Galerkin method to solve the full Navier-Stokes equations on a finite elements grid. The module DROP3D uses an Eulerian approach to calculate the droplet distribution and the droplet impingement on the walls. ICE3D utilizes the Messinger method to calculate the flow of the fluid film on the surface of the propeller and calculate the ice accretion. ANSYS FLUENT meshing is used than to create a new mesh, which is once again used to perform the flow calculation using ANSYS FENSAP. The total icing time is split into ten cycles, and for each one a new flowfield is calculated.

The calculation of the aerodynamic performance is validated by simulation of the flow around the DA4002 propeller. By performing a grid dependency study, the mesh for the simulation was evaluated. The optimal mesh was determined by the negligible difference between the aerodynamic values between the meshes. The mesh with the minimum simulation time was chosen, as it is the most cost and time efficient of all the meshes. For the validation of the performance, the values calculated by the mesh were compared to experimental performance data.

To validate the ice accretion, the ice accretion of a scaled version of a helicopter rotor blade with a NACA0012 was calculated. Here the ice accretion was calculated for two different meteorological conditions, which correspond to two experiments in an icing wind tunnel.

Finally, the simulations were combined to calculate the ice accretion on the propeller for the PX-31 Falk UAV. The icing was calculated at three points, which includes the point for the worst-case scenario for the icing of the wing of the PX-31 Falk. It was found that at -2°C, only a very small amount of ice accretion was registered, which was only on the middle and central part of the propeller. At -5°C, the icing on the propeller was found to represent a graze ice shape with two span-wise horns on the top and bottom of the propeller, with the horn on top of the propeller being the longer of the two. The ice shape at a temperature of -15°C is indicative of a typical rime ice shape, as the ice shape is very streamlined, and does not show horns. The ice mass at this temperature is larger, compared to the ice at -2°C.

On the final ice shapes, a performance analysis was performed, to find the performance degradation of the two propellers. The ice shape created at -2°C has the least impact on the icing of the propeller, as the efficiency has only been reduced by 12.7% compared to the clean propeller configuration. The efficiency of the propeller was reduced by 62.8%, compared to the clean propeller, with the ice shape created at -5°C. This reduction is mainly due to the reduction in thrust of 46.2% compared to the clean propeller. The reason for this large reduction in the thrust is that the span-wise horns hinder the clean flow of the air over the propeller. This leads to a separation of the flow and therefore the loss in thrust. At -15°C, the loss of efficiency is only 30% although the mass of the ice is much larger. This is due to the fact that the ice shape is much more streamlined and therefore the ice does not disrupt the flow of the air over the propeller as much as the horns do.

Using the simulation at -15°C, the required power of an electro-thermal anti-icing system was estimated. The total power required to prevent the ice accretion was found to be at a 170 W for the propeller, if the system is designed to prevent the ice from accumulating. If the system design aims to evaporate the water from the propeller, the required power increases to 249 W. The heaters in the propeller should be focused on the leading edge of the propeller, and the required heat flux increases with the radius of the propeller.

A large challenge during the development of the process to calculate the ice accretion on a propeller has been the small amount of ice accretion experiments performed on propellers at a similar Reynolds number. For this reason, the next step in the development of a process to calculate the icing of a UAV is the validation of the results by performing ice accretion experiments on a propeller in an icing wind tunnel, and execute tests to estimate the performance penalties of the ice on the propeller. This data can be used to refine the mesh and simulation settings of the process. This will lead to an increase in the credibility of the results of the ice accretion results. Especially the use of a fully turbulent boundary layer over the ice needs to be validated for the use at such low Reynolds numbers.

The knowledge of the required heat loads and the severeness of the icing at different situations can be used to develop an icing protection system for UAVs. This system could use electro-resistive heaters to prevent the ice from accumulating on the propeller. Using such an icing protection system would allow the operation of small UAVs under atmospheric icing conditions, further extending the operational envelope of UAVs. Knowledge of the severeness of different icing conditions can be used to automatically operate an intermittent icing protection system, whenever the icing conditions necessitate it. And for UAVs without a icing protection system, the data can be used in the route-planing of the autopilot, to avoid areas, where the icing would be a threat to the UAV. The developed process could also be applied to the calculation of the icing on the propellers of multi-rotor UAVs, for which the thrust of the propellers is directly responsible for the lift of the UAV. This makes the multi-rotor UAVs more vulnerable to icing on the propeller, as any loss in lift could lead to immediate loss of control of the UAV.

The next step in the simulation of the ice accretion on a propeller of a UAV are the creation of additional experimental data. This will allow the simulation to be validated against experiments, that are closer to the propeller of a UAV in terms of Reynolds number, as well as in the general shape. The ice accretion could be analysed under more different conditions, to find the influence of the rotational speed of the propeller on the ice accretion. With this data, a ice protection system for the propeller of a UAV could be designed.

Acknowledgements

Bibliography

[1] B. C. Bernstein and C. Le Bot, "An Inferred Climatology of Icing Conditions Aloft, Including Supercooled Large Drops. Part II: Europe, Asia, and the Globe," *Journal of Applied Meteorology and Climatology*, vol. 48, pp. 1503–1526, 08 2009.

[2] R. Hann, *Atmospheric Ice Accretions, Aerodynamic Icing Penalties, and Ice Protection Systems on Unmanned Aerial Vehicles.* PhD thesis, Norwegian University of Science and Technology, 2020.

[3] ANSYS Inc., "Ansys fensap-ice user manual, release 20.1," 2020.

[4] Airfoil Tools, "Clark y airfoil - clark y airfoil seen on 2020-10-09," 2020. `http://airfoiltools.com/airfoil/details?airfoil=clarky-il"`.

[5] R. Deters, *Performance and Slipstream Characteristics of Small-scale Propellers at Low Reynolds Numbers.* University of Illinois at Urbana-Champaign, 2014.

[6] Airfoil Tools, "NACA 0012 AIRFOILS (n0012-il) Seen on 2020-10-09," 2020. `http://airfoiltools.com/airfoil/details?airfoil=n0012-il"`.

[7] Y. Han, J. L. Palacios, and E. C. Smith, "An experimental correlation between rotor test and wind tunnel ice shapes on NACA 0012 airfoils," *SAE Technical Papers*, 2011.

[8] Federal Aviation Administration (FAA), "Part i – atmospheric icing conditions," *Title 14 CFR Part 25 Appendix C, Doc. No. 4080, 29 FR 17955, Amdt. 25-140, 79 FR 65528*, 2014.

[9] Y. Liu, L. Li, Z. Ning, W. Tian, and H. Hu, "An experimental study on the transient ice accretion process over the blade surfaces of a rotating UAS propeller," *AIAA SciTech Forum - 55th AIAA Aerospace Sciences Meeting*, no. January, 2017.

[10] Maritime Robotics, "PX-31 Unmanned Aircraft System [UAS] Seen on 9.10.202020," `https://pdf.aeroexpo.online/pdf/maritime-robotics/px-31-brochure/181323-12497.html`.

[11] C. C. R. P. Lindamae and J. Martel, "Army aircraft icing," *Technical Report ERDC/CRREL TR-02-13*, September 2002.

[12] M. Bragg, A. Broeren, and L. Stirling, "Ice-airfoil aerodynamics," *Progress in Aerospace Sciences - PROG AEROSP SCI*, vol. 41, pp. 323–362, July 2005.

[13] R. A. Siquig:, "Impact of icing on unmanned aerial vehicel (uav) operations.," *Technical Report AD-A231 191*, 1990.

[14] T. A. Berntsen and G. L. Dyndal, "Autonomous military drones: no longer science fiction," July 2017. `https://www.nato.int/docu/review/articles/2017/07/28/autonomous-military-drones-no-longer-science-fiction/index.html"`.

[15] H. Shakhatreh, A. H. Sawalmeh, A. Al-Fuqaha, Z. Dou, E. Almaita, I. Khalil, N. S. Othman, A. Khreishah, and M. Guizani, "Unmanned aerial vehicles (uavs): A survey on civil

applications and key research challenges," *IEEE Access*, vol. 7, pp. 48572–48634, 2019.

[16] A. Sóbester and A. Forrester, *Airfoil Engineering: Fundamentals*, ch. 5, pp. 91–102. John Wiley and Sons, Ltd, 2014.

[17] G. K. Schlichting H., *Fundamentals of Boundary–Layer Theory*. Springer, Berlin, Heidelberg, 2017.

[18] W. Johnson, *Helicopter theory*. Courier Corporation, 2012.

[19] B. McCormick, *Aerodynamics, Aeronautics, and Flight Mechanics*, vol. 2nd Edition. Wiley, 1995.

[20] R. Hann and T. A. Johansen, "Unsettled topics in unmanned aerial vehicle icing," *SAE Edge Report*, April 2020.

[21] B. C. Bernstein, C. A. Wolff, and F. McDonough, "An Inferred Climatology of Icing Conditions Aloft, Including Supercooled Large Drops. Part I: Canada and the Continental United States," *Journal of Applied Meteorology and Climatology*, vol. 46, pp. 1857–1878, 11 2007.

[22] M.-P. M.K.Politovich, *Aircraft Icing*. Encyclopedia of Atmospheric Sciences, 2015.

[23] Z. Janjua, B. Turnbull, S. Hibberd, and K.-S. Choi, "Mixed ice accretion on aircraft wings," *Physics of Fluids*, vol. 30, January 2018.

[24] B. Bernstein, T. Ratvasky, D. Miller, and F. Mcdonough, "Freezing rain as an in-flight icing hazard," *NASA/TM—2000-210058*, 07 2000.

[25] M. Fengler, *Study of Propeller Icing Hazard in Mini-UAV Aviation*, 2017.

[26] R. W. Gent, N. P. Dart, and J. T. Cansdale, "Aircraft Icing," *Journal of Glaciology*, vol. 1, no. 2, pp. 68–69, 2000.

[27] N. Fajt, R. Hann, and T. Lutz, "The Influence of Meteorological Conditions on the Icing Performance Penalties on a UAV Airfoil," *8th European Conference for Aeronautics and Space Sciences (EUCASS)*, July 2019.

[28] K. Szilder and S. McIlwain, "In-flight icing of UAVs - The influence of reynolds number on the ice accretion process," *SAE Technical Papers*, 2011.

[29] M. Papadakis, U. S. N. Aeronautics, S. Administration, L. R. Center, and F. A. A. T. C. (U.S.), "An experimental method for measuring water droplet impingement efficiency on two- and three-dimensional bodies," *NASA Contractor Report 4257 DOT/FAA/CT–87/22*, 1989.

[30] R. Hann and N. Müller, "Icing validation database," 2020. `https://doi.org/10.18710/5XYALW`.

[31] J. Shin and T. Bond, "Experimental and computational ice shapes and resulting drag increase for a naca 0012 airfoil," 1992.

[32] A. P. Broeren, S. Lee, B. Woodard, C. W. Lum, and T. G. Smith, *Independent Effects of Reynolds and Mach Numbers on the Aerodynamics of an Iced Swept Wing*.

[33] C.-D. Munz and T. Westermann, *Numerische Behandlung gewöhnlicher und partieller Differenzialgleichungen ein interaktives Lehrbuch für Ingenieure*. Springer Vieweg, 2012.

[34] B. Weigand, K. Jürgen, and J. v. Wolfersdorf, *Thermodynamik kompakt*. Springer Vieweg, 2016.

[35] J. S. Monk, "A propeller design and analysis capability evaluation for high altitude application," University of the Witwatersrand, 2011.

[36] D. C. Wilcox *et al.*, *Turbulence modeling for CFD*, vol. 2. DCW industries La Canada, CA, 1998.

[37] W. Kong and H. Liu, "An ice accretion model for aircraft icing based on supercooled icing: Theory and application," *50th AIAA Aerospace Sciences Meeting Including the New Horizons Forum and Aerospace Exposition*, no. January, 2012.

[38] H. Beaugendre, F. Morency, and W. G. Habashi, "Fensap-ice's three-dimensional in-flight ice accretion module: Ice3d," *Journal of Aircraft*, vol. 40, no. 2, pp. 239–247, 2003.

[39] O. Isik, S. David, B. Guido S., and J. Chen, "Multi-shot icing simulations with automatic re-meshing," *SAE Technical Paper*, vol. 2019-01-1956, June 2019.

[40] M. Drela, "Xfoil: An analysis and design system for low reynolds number airfoils.," *MIT Dept. of Aeronautics and Astronautics,*, 1989.

[41] Dassault Systèmes, "Catia documentation version 5 release 19," 2008.

[42] N. Fajt, R. Hann, and L. T., "The influence of meteorological conditions on the icing performance penalties on a uav airfoil," *8th European Conference for Aeronautics and Aerospace Sciences (EUCASS)*, 2019.

[43] S. Rüdiger, *CFD-Modellierung: Grundlagen und Anwendungen bei Strömungsprozessen.* Springer Vieweg, 2013.

[44] NATO RTO Technical Report 38, "Ice accretion simulation evaluation test," *RTO-TR-038 AC/323(AVT-006)TP/26*, 2001.

[45] E. M. Coates, A. Wenz, K. Gryte, and T. A. Johansen, "Propulsion system modeling for small fixed-wing UAVs," *2019 International Conference on Unmanned Aircraft Systems, ICUAS 2019*, pp. 748–757, 2019.

A

A. Validation Database

Title	Year	2D/3D	Reynolds number
NTNU low-speed IWT tests	2019	2D	1
Ice accretions and icing effects for modern airfoils	2000	2D	3-10
Technical Report 38,"Ice Accretion Simulation Evaluation Test,	2001	2D	3-6
Experimental investigation of water droplet impingement on airfoils, finite wings, and an S-Duct engine inlet	2002	2D/3D	1.6
An Experimental Correlation between Rotor Test and Wind Tunnel Ice Shapes on NACA 0012 Airfoils	2011	3D	1
Ice-Accretion Test Results for Three Large-Scale Swept-Wing Models in the NASA Icing Research Tunnel	2016	3D	0.34-0.41
Effects of thermal conductivity of airframe substrate on the dynamic ice accretion process pertinent to UAS inflight icing phenomena	2018	2D	0.4
An experimental study on the aerodynamic performance degradation of a UAS propeller model induced by ice accretion process	2018	3D	0.03
Effect of Variable LWC on Ice Shape in the NASA-GRC IRT	2003	2D	n/a
The Icing of an Unheated, Nonrotating Cylinder. Part II. Icing Wind Tunnel Experimentsm Low Temperature Laboratory	1983	2D	0.06-0.2
An experimental study on the dynamic ice accretion processes on bridge cables with different surface modifications	2019	2D	0.125-0.15
An experimental study on the aerodynamic performance degradation of a wind turbine blade model induced by ice accretion process	2018	2D	0.42
An Experimental Study to Evaluate Hydro-/Ice-Phobic Coatings for Icing Mitigation over Rotating Aero-engine Fan Blades	2019	3D	n/a
An Experimental Study of the Dynamic Ice Accreting Process over a Rotating Aero-engine Fan Model	2018	3D	0.1

Table A.2.: Icing validation database part 1.

Title	Year	2D/3D	Reynolds number
An Experimental Study on the Dynamic Ice Accretion Processes on Bridge Cables with Different Surface Modifications	2019	2D	n/a
An experimental investigation of dynamic ice accretion process on a wind turbine airfoil model considering various icing conditions	2018	2D	0.4
An experimental investigation on the dynamic glaze ice accretion process over a wind turbine airfoil surface	2019	2D	0.3
An Experimental Study of Dynamic Ice Accretion Process on Aero-engine Spinners	2017	3D	0.3
An experimental study on a hot-air-based anti-/de-icing system for aero-engine inlet guide vanes	2019	2D	0.3
An Experimental Study on the Effects of the Layout of DBD Plasma Actuators on Its Anti-/De-Icing Performance for Aircraft Icing Mitigation	2019	2D	n/a
Dynamic ice accretion process and its effects on the aerodynamic drag characteristics of a power transmission cable model	2020	2D	0.5
Quantification of the 3D shapes of the ice structures accreted on a wind turbine airfoil mode	2019	2D	0.3
An Experimental Study on the Transient Ice Accretion Process over the Blade Surfaces of a Rotating UAS Propeller	2017	3D	0.05
Experimental and Computational Ice Shapes and Resulting Drag Increase for a NACA 0012 Airfoil	1992	2D	2-3
30th Aerospace Sciences Meeting and Exhibit	1992	2D	2-3
Scaled ice accretion experiments on a rotating wind turbine blade	2011	3D	0.9-1.2
Icing Wind Tunnel Test of a Full Scale Heated Tail Rotor Model	2014	3D	n/a
The Influence of SLD Drop Size Distributions on Ice Accretion in the NASA Icing Research Tunnel	2019	2D	6-15
An overview of a model rotor icing test in the NASA Lewis Icing Research Tunnel	1994	3D	1.5
Spring Rotor Blade Tests in Icing Wind Tunnel	2009	3D	0.77-5.9
Large and Small Droplet Impingement data on Airfoils and Two Simulated Ice Shapes	2000	2D	1.6
Experimental ice shape and performance characteristics for a multi- element airfoil in the NASA lewis icing research tunnel	1991	2D	1.25

Table A.4.: Icing validation database part 2.

Title	Year	2D/3D	Reynolds number
Icing Analysis and Test of's Business Jet Engine Inlet Duct	2000	3D	n/a
Project „SOPHIA-2" – Final Report	2019	3D	n/a
The Experimental Investigation of a Rotor Icing Model with Shedding	2010	3D	0.6-0.9
Validation Ice Crystal Icing Engine Test in the Propulsion Systems Laboratory at NASA Glenn Research Center	2015	3D	n/a
Experimental Study on Icing and Anti-Icing Characteristics of Engine Inlet Guide Vanes	2015	3D	n/a
Experiment Investigation of Hot-air Anti-icing Structure of Engine Inlet Vane	2016	2D	?
Collection Efficiency and Ice Accretion Characteristics of Two Full Scale and One 1/4 Scale Business Jet Horizontal Tails	2005	3D	5
Ice Accretions and Full-Scale Iced Aerodynamic Performance Data for a Two-Dimensional NACA 23012 Airfoil	2016	2D	4.6
Validation of 3-D Ice Accretion Measurement Methodology for Experimental Aerodynamic Simulation	2015	2D	1.8
Ice Accretions on a Swept GLC-305 Airfoil	2002	3D	2
Modern Airfoil Ice Accretions	1997	2D	3.5
A Database of Supercooled Large Droplet Ice Accretions	2007	2D	2.5-13
Experimental Investigation of Ice Accretion Effects on a Swept Wing	2005	3D	1-4
An Integrated Approach to Swept Wing Icing Simulation		3D	1.8-15.9
Summary of Ice Shape Geometric Fidelity Studies on an Iced Swept Wing	2018	3D	1.8-15.9
Water droplet impingement on airfoils and aircraft engine inlets for icing analysis	1991	2D/3D	n/a
Experimental Water Droplet Impingement Data on Airfoils, Simulated Ice Shapes, an Engine Inlet and a Finite Wing	1994	2D/3D	4.5
Experimental Study of Supercooled Large Droplet Impingement Effects	2003	n/a	n/a
Large and Small Droplet Impingement Data on Airfoils and Two Simulated Ice Shapes	2007	2D	1.6
Water Droplet Impingement on Simulated Glaze, Mixed, and Rime Ice Accretions	2007	2D	1.6

Table A.5.: Icing validation database part 3.

Title	Year	2D/3D	Reynolds number
Validation Results for LEWICE 3.0	2005	2D	1.6
An Experimental and Numerical Study of Icing Effects on the Performance and Controllability of a Twin Engine Aircraft	1998	2D	10
Ice Protection System	2001	2D	2.5-5.0
Ice Roughness and Thickness Evolution on a Swept NACA 0012 Airfoil	2017	2D	4
Improvement of the ONERA 3D Icing Code, Comparison with 3D Experimental Shapes	1993	3D	1-6.5
Independent Effects of Reynolds and Mach Numbers on the Aerodynamics of an Iced Swept Wing	2018	3D	1.6-11.9
A Wind Tunnel Study of Icing Effects on a Business Jet Airfoil	2003	2D	3.5-10.5
Comparison of Iced Aerodynamic Measurements on Swept Wing from Two Wind Tunnels	2018	3D	1.6-2.7
Super Cooled Large Droplet Analysis of Several Geometries Using LEWICE3D Version 3	2011	3D	5
Icing Simulation Research Supporting the Ice-Accretion Testing of Large-Scale Swept-Wing Models	2018	3D	2.5-6.5
Lewice Modelling of Swept Wing Ice Accretions	2003	3D	2.5-4.3
Implementation and Validation of 3-D Ice Accretion Measurement Methodology	2014	2D/3D	2.6-6.0
Ice Shapes on a Tail Rotor	2014	3D	0.26-0.65
Icing Analysis of a Swept NACA 0012 Wing Using LEWICE3D Version 3. 48	2014	3D	2.6-6.0
Collection Efficiency and Ice Accretion Calculations for a Sphere, a Swept MS(1)-317 Wing, a Swept NACA-0012 Wing Tip, an Axisymmetric Inlet, and a Boeing 737-300 Inlet	1995	3D	0.75-5
An Experimental Method for Measuring Water Droplet Impingement Efficiency on Two- and Three-Dimensional Bodies	1989	2D/3D	0.4-5
Improvement of the ONERA 3D Icing Code, Comparison with 3D Experimental Shapes	1993	3D	7.7
Wind Turbine Performance under Icing Conditions	2008	2D	0.26-0.733
An experimental study on the anti-icing performance of superhydrophobic surface on a rotating UAS propeller	2017	3D	0.05

Table A.7.: Icing validation database part 4.

F

B. Ice accretion cases

B.1. Case 1
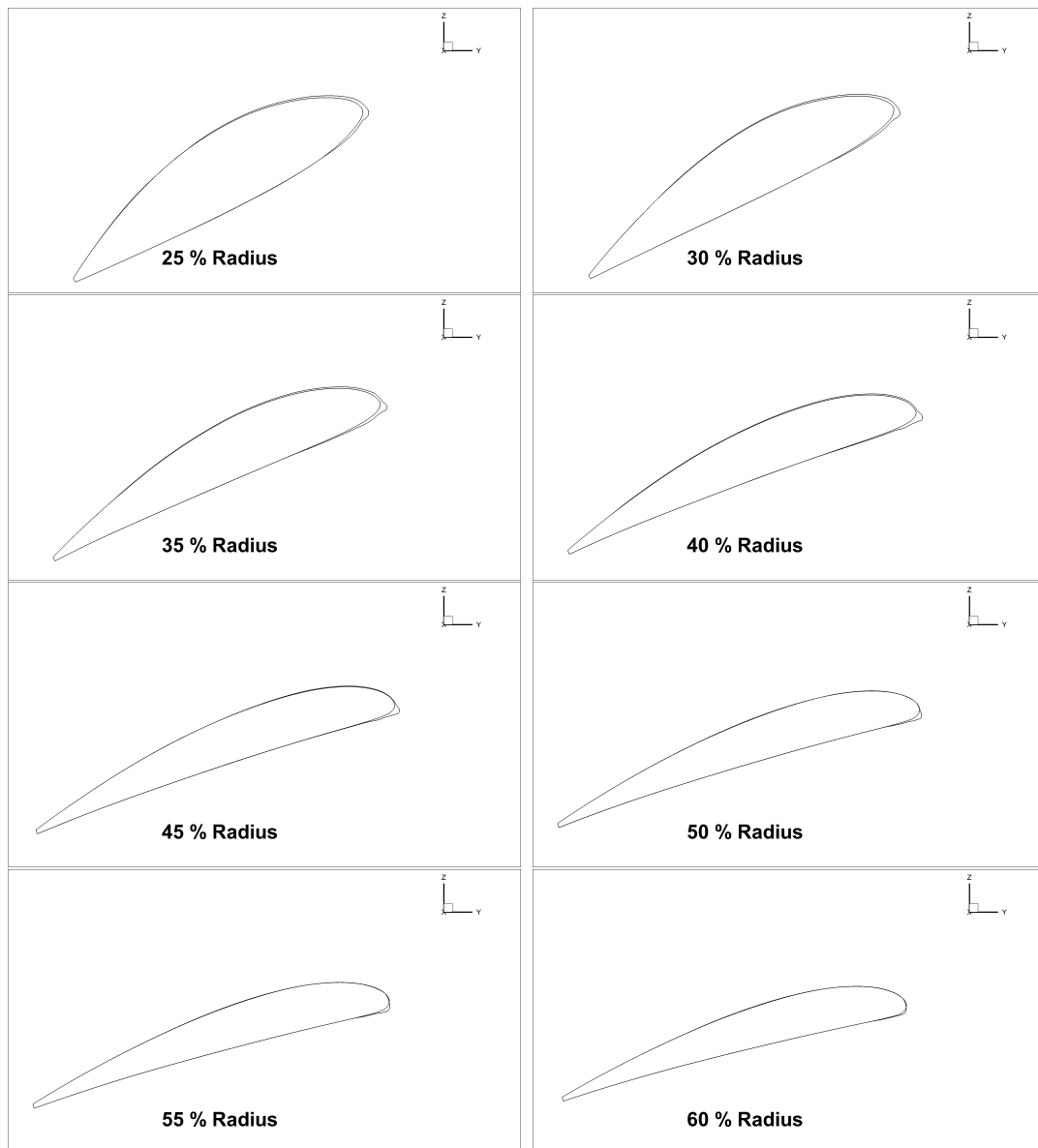
Figure B.1.: Ice Shapes at -2°C up to 60% of the radius.

75 % Radius

80 % Radius

85 % Radius
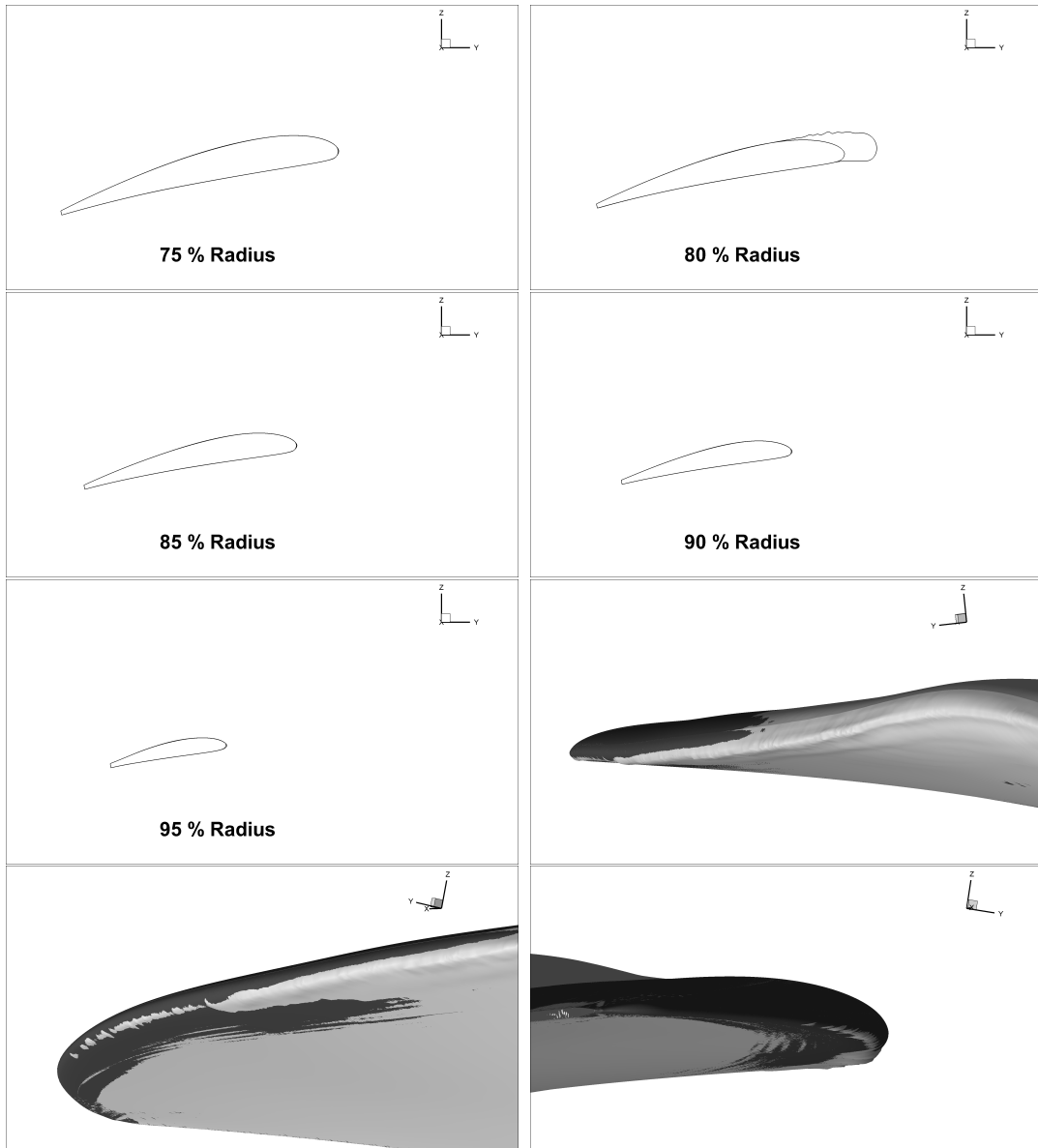
90 % Radius

95 % Radius

Figure B.2.: Ice shapes at -2°C from 65 % of the radius.

H

B.2. Case 2
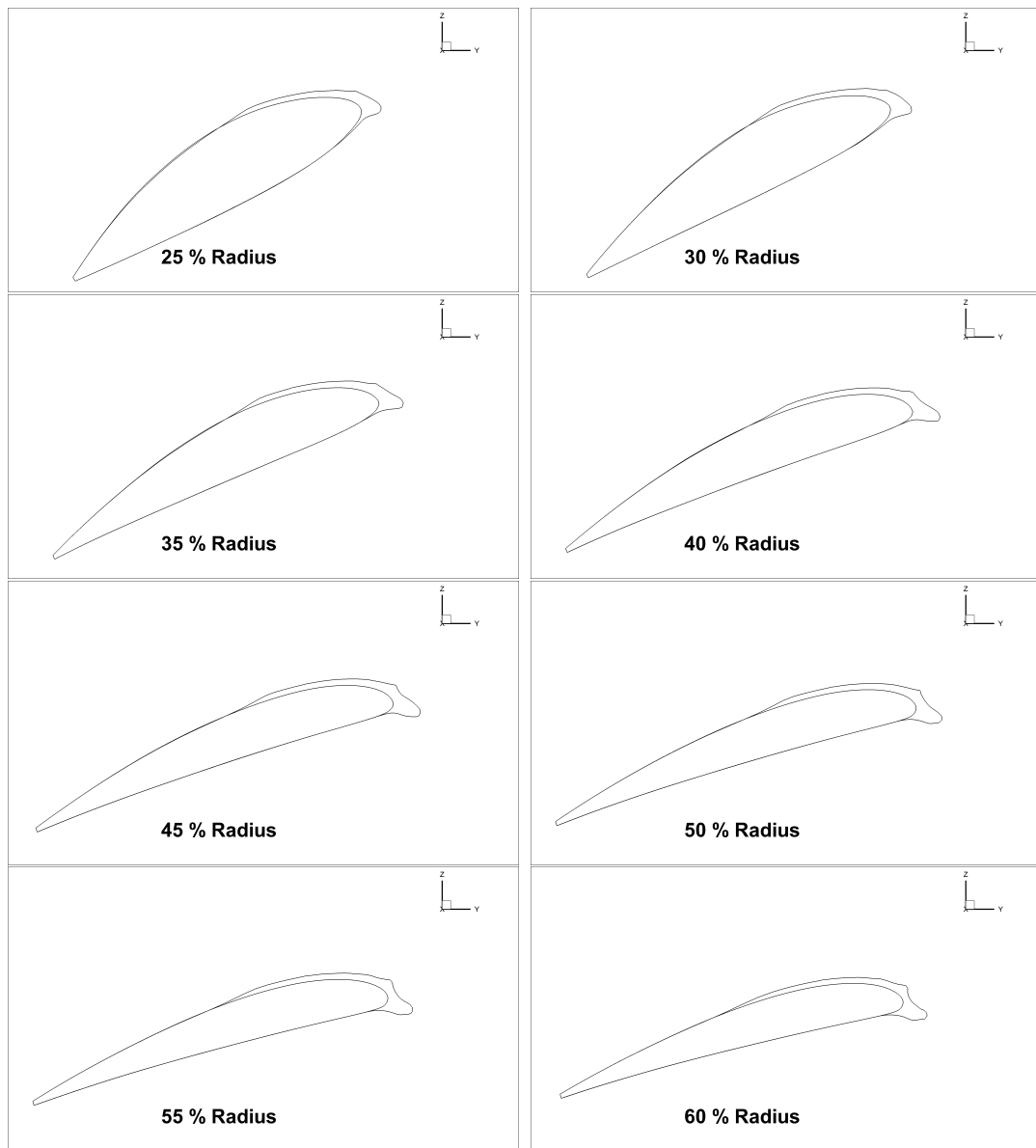
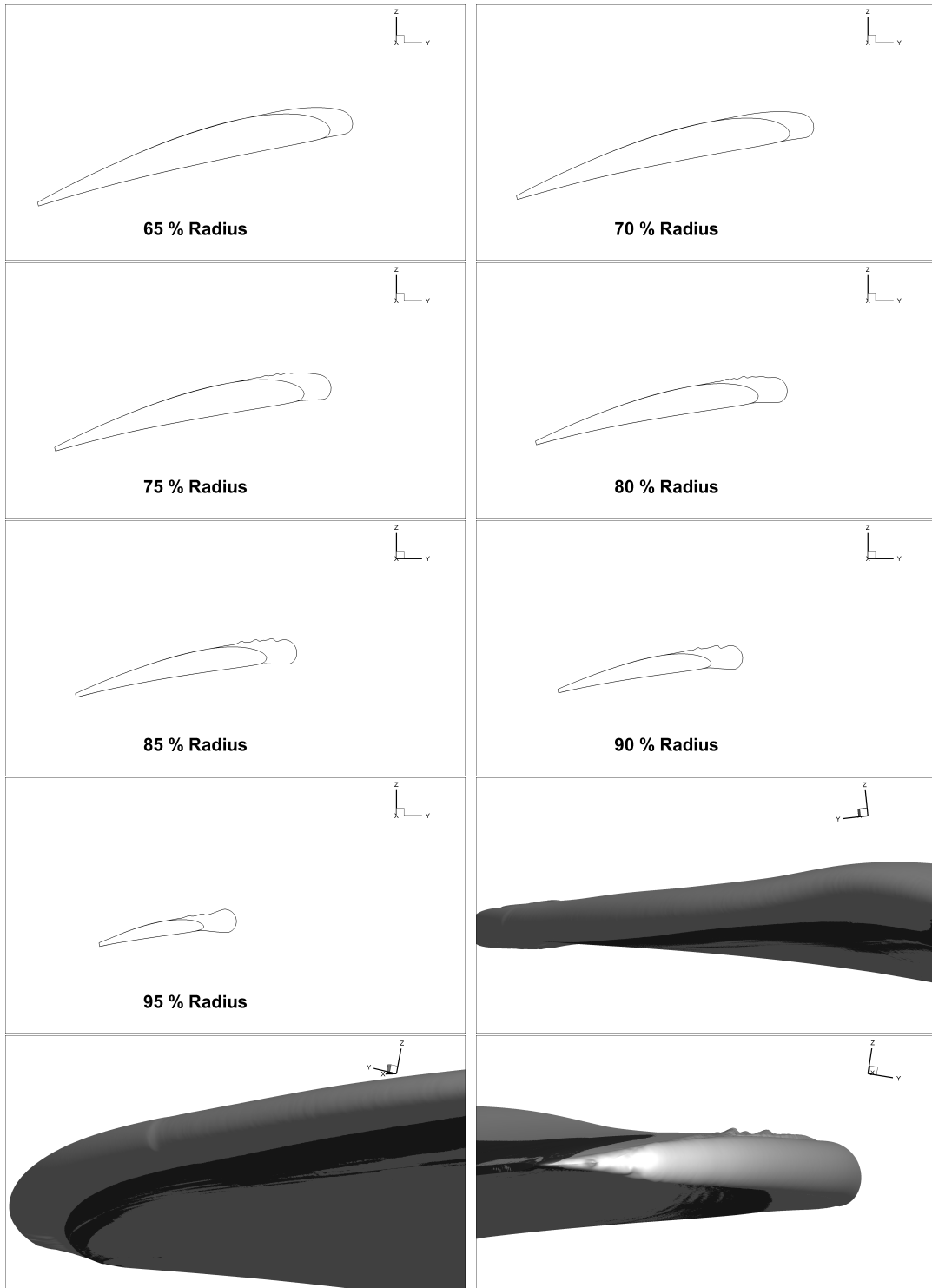**Figure B.3.:** Ice shapes at -5°C up to 60% of the radius.
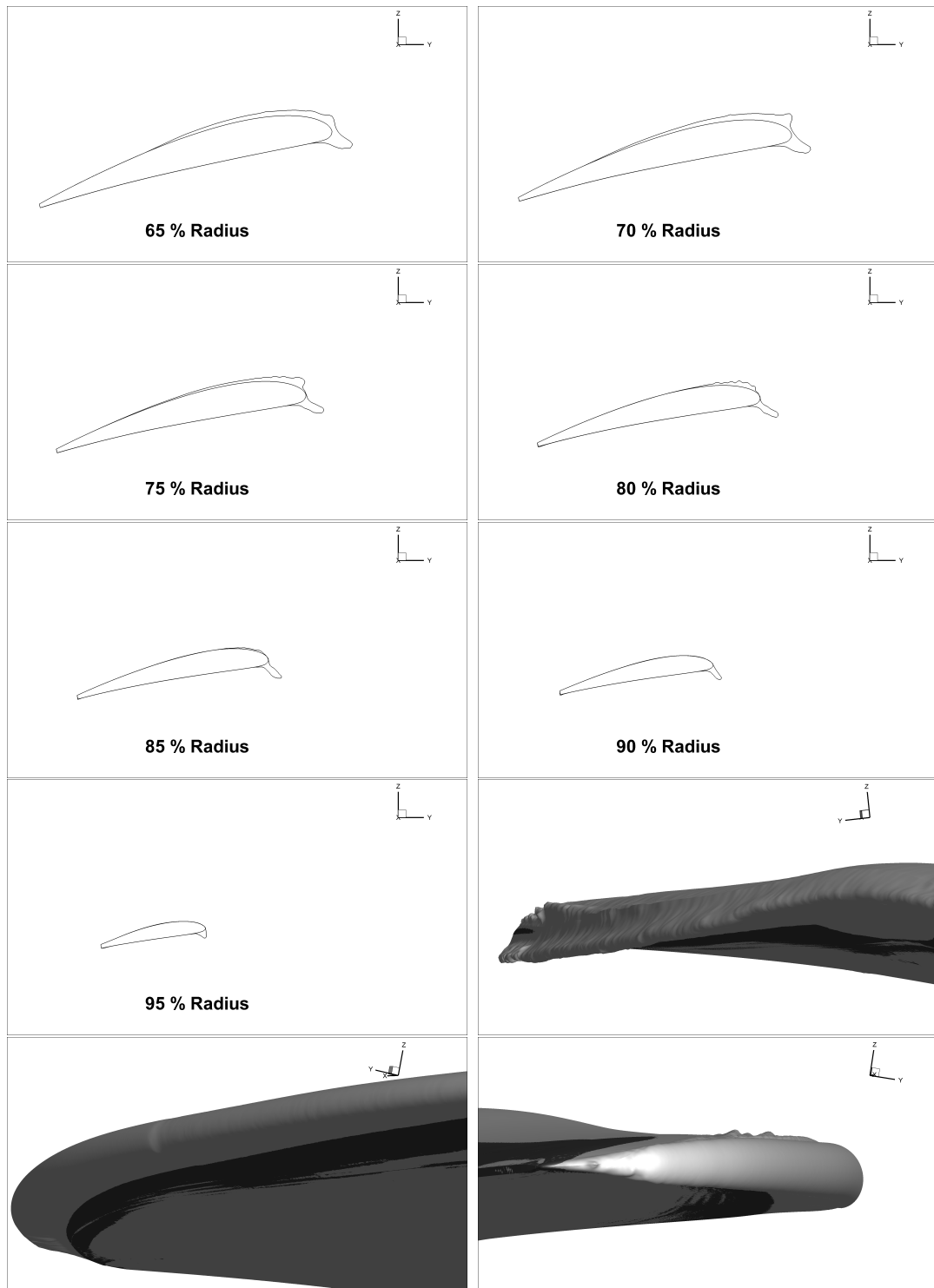
Figure B.4.: Ice Shapes at -5°C from 65 % of the radius.

B.3. Case 3
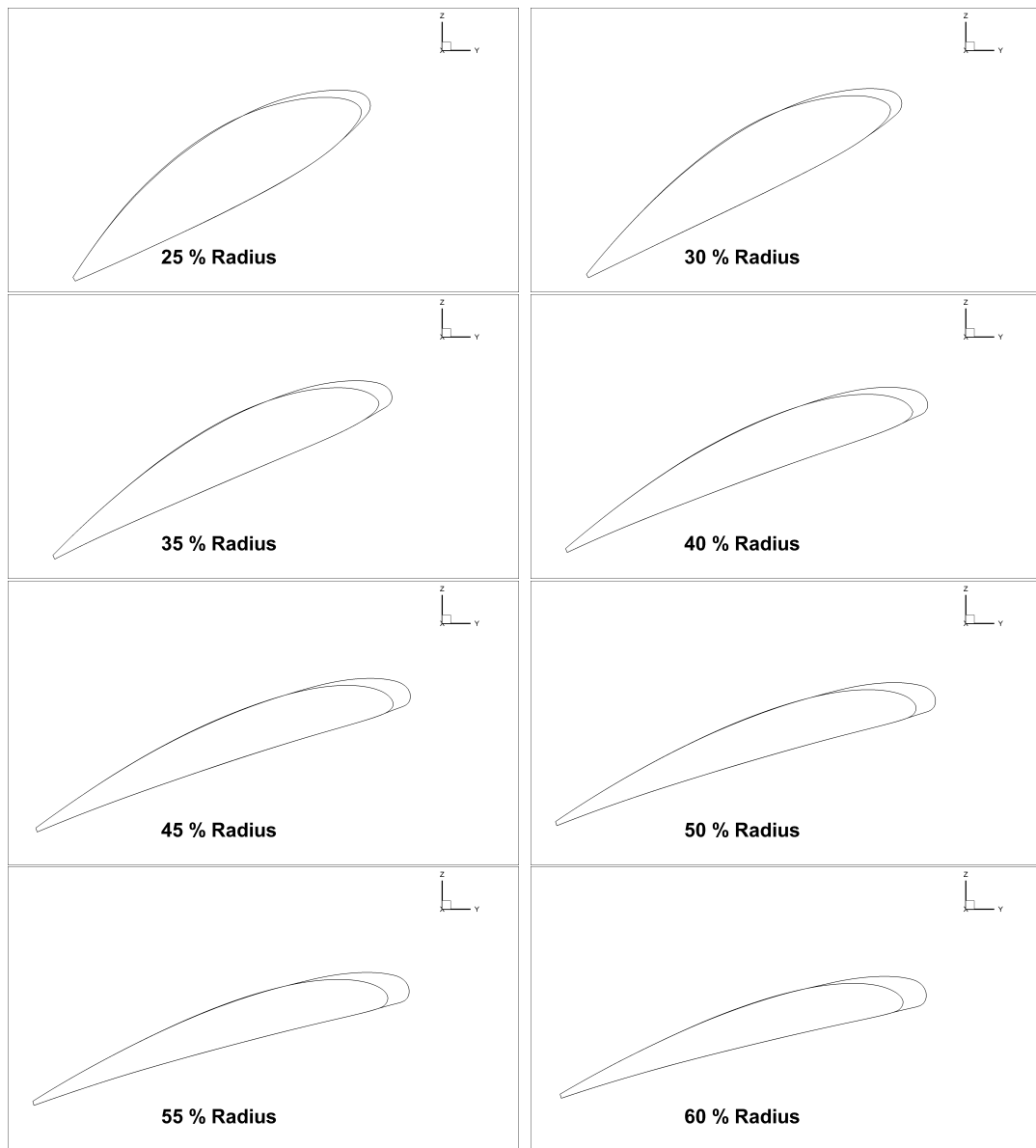
Figure B.5.: Ice shapes in the Case 3 at -15°C up to 60% of the radius.

Figure B.6.: Ice shapes in the Case 3 at -15°C from 65 % of the radius.

C. Performance degradation

C.1. Clean propeller
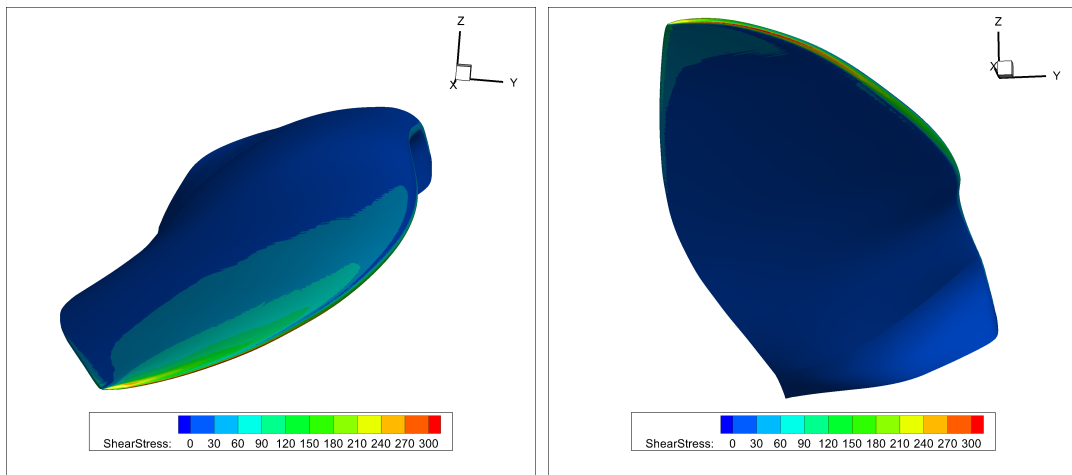
Figure C.1.: Shear stress on the surface of the clean propeller.
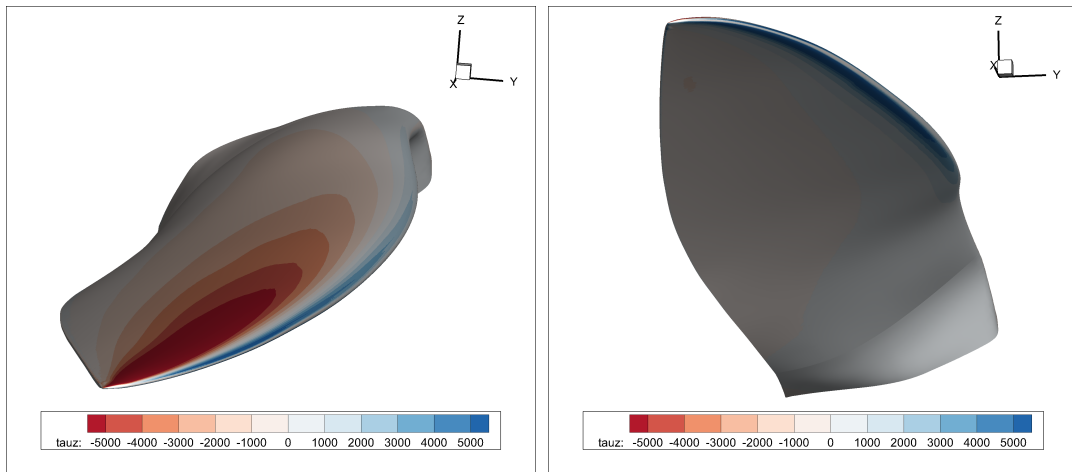
Figure C.2.: Force in Z direction f_Z on the clean propeller.
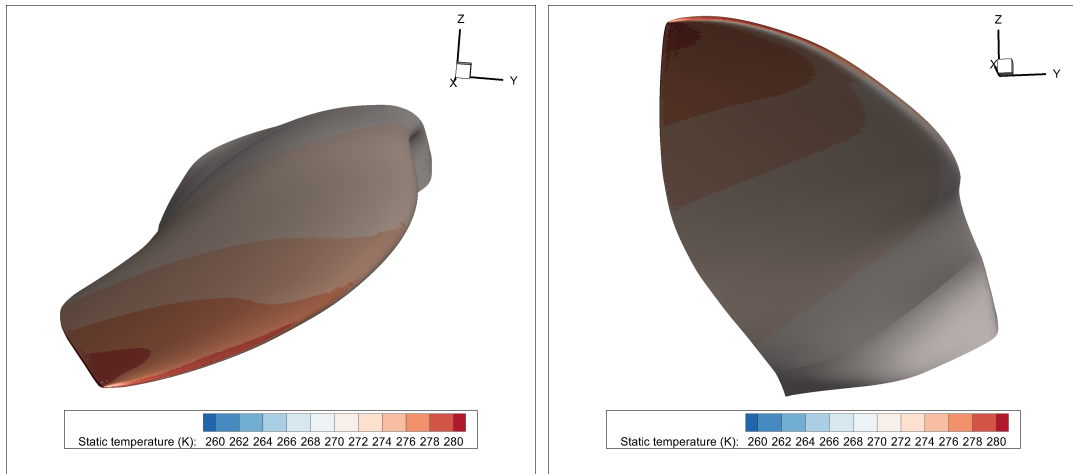
Figure C.3.: Surface temperatures on the ice shape on the clean propeller.
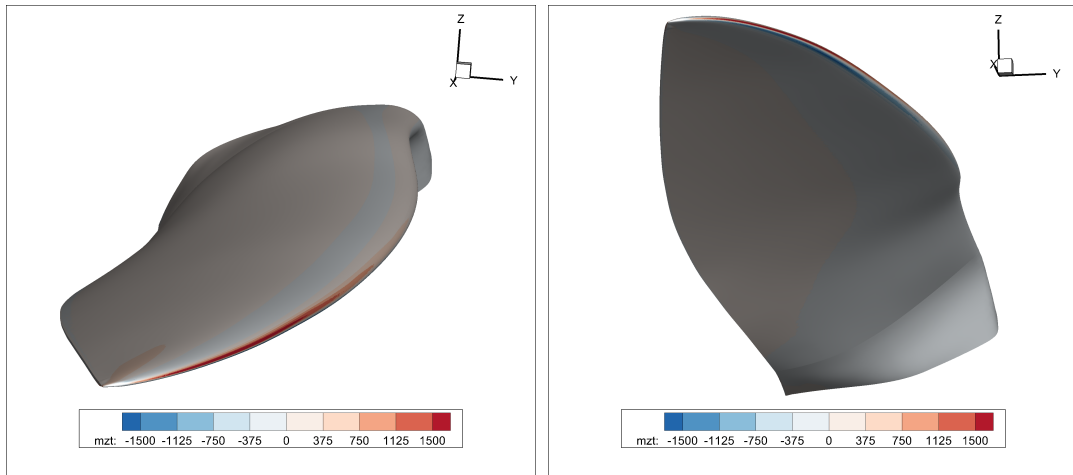
Figure C.4.: Momentum in the z axis m_Z on the clean propeller.

C.2. Case 1
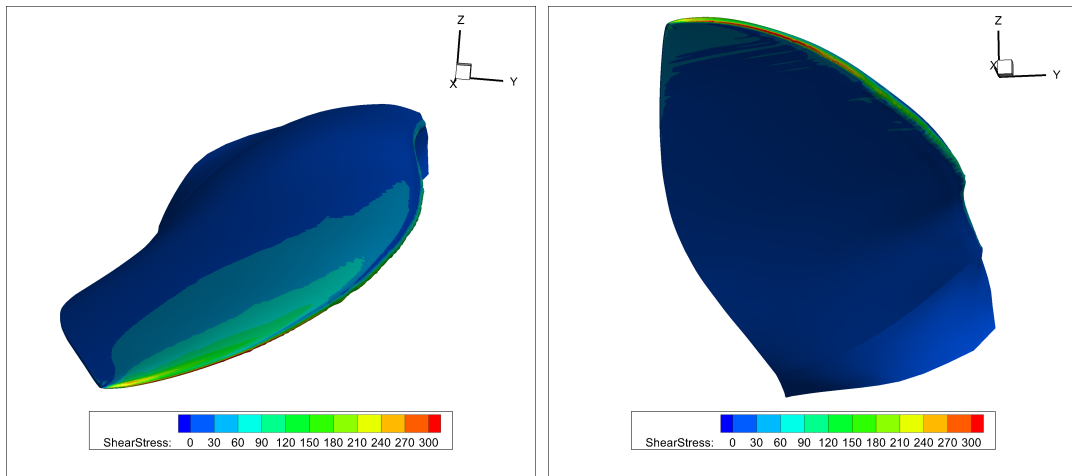
Figure C.5.: Shear stress on the surface of the ice shape at -2°C.
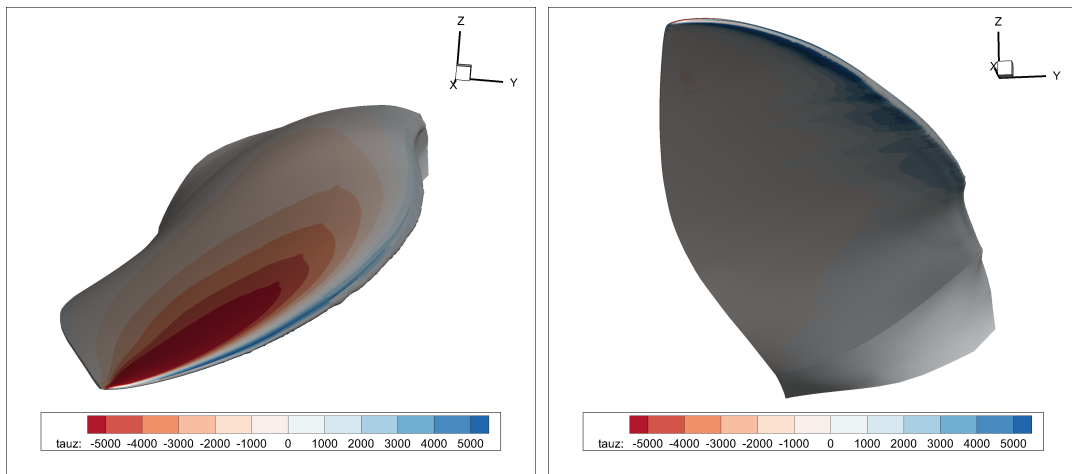
Figure C.6.: Force in Z direction f_Z on the ice shape at -2°C

O
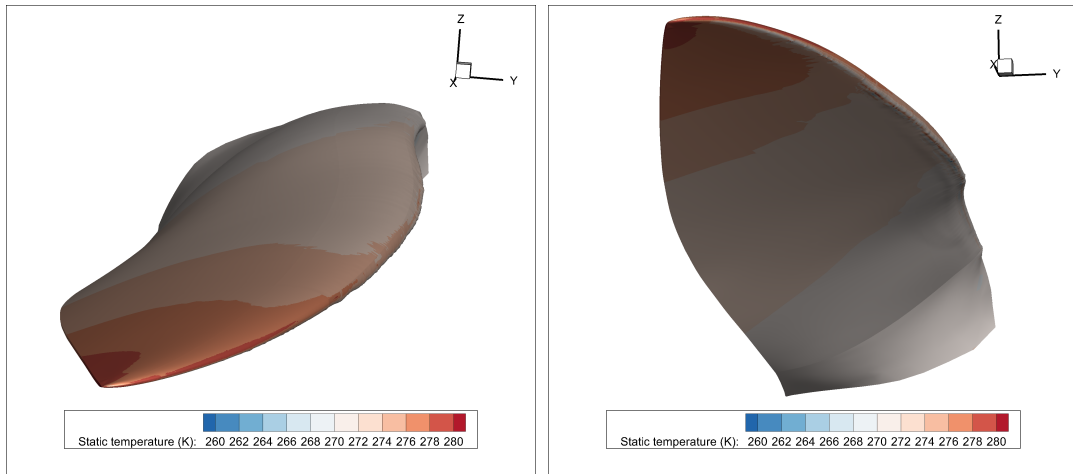
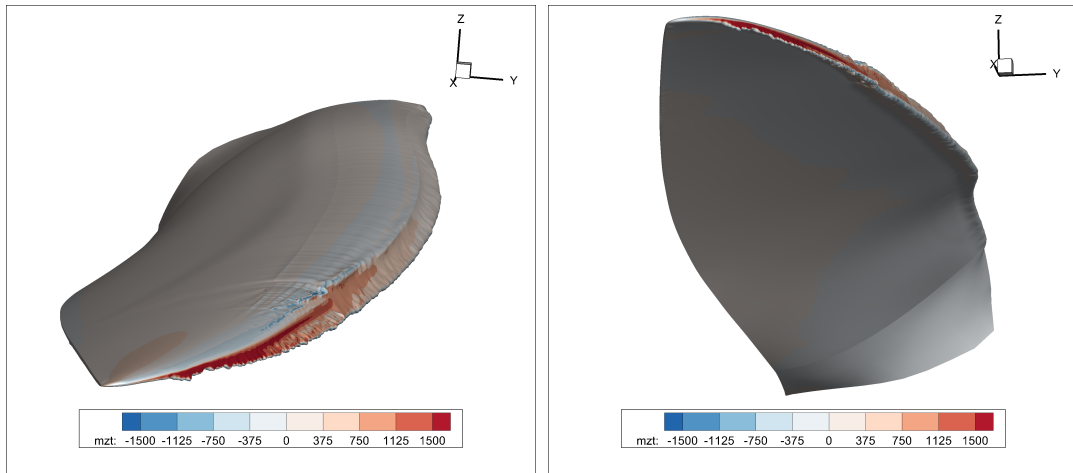**Figure C.7.:** Surface temperatures on the ice shape at -2°C.
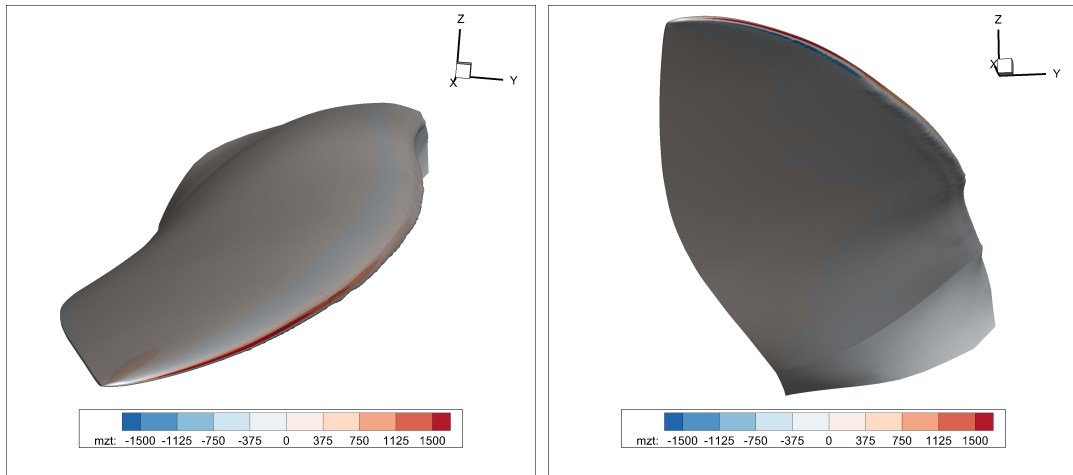
Figure C.8.: Momentum in the z axis m_{z} an the ice shape at -2°C.

C.3. Case 2
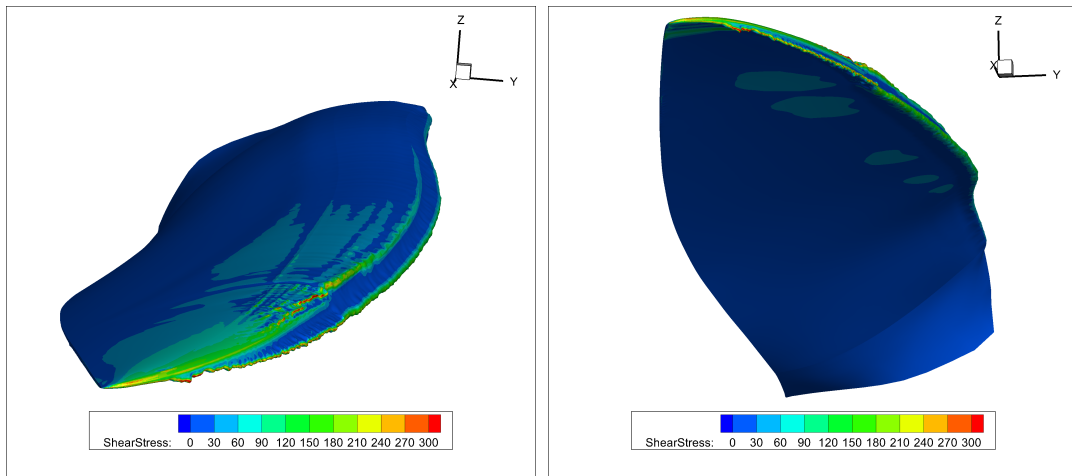
Figure C.9.: Shear stress on the surface of the ice shape at -5°C.
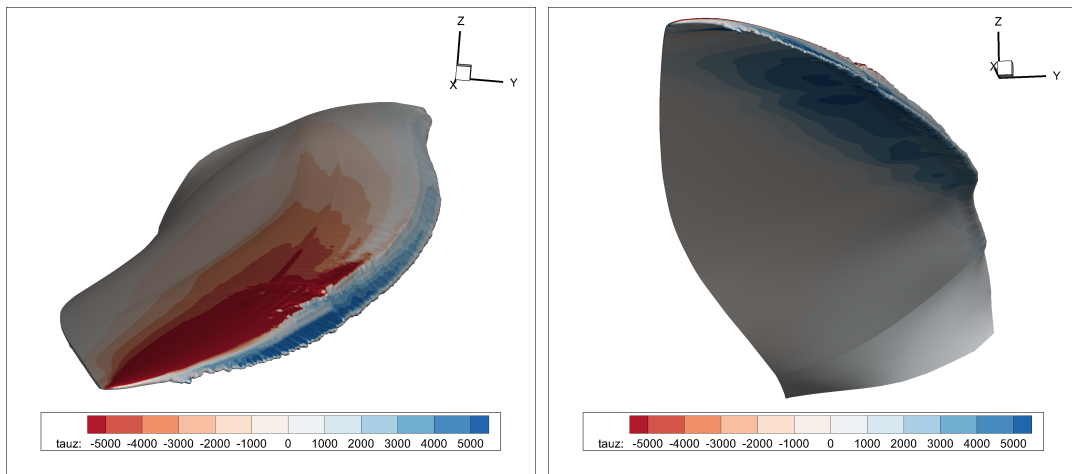
Figure C.10.: Force in Z direction f_Z on the ice shape at -5°C.

Q
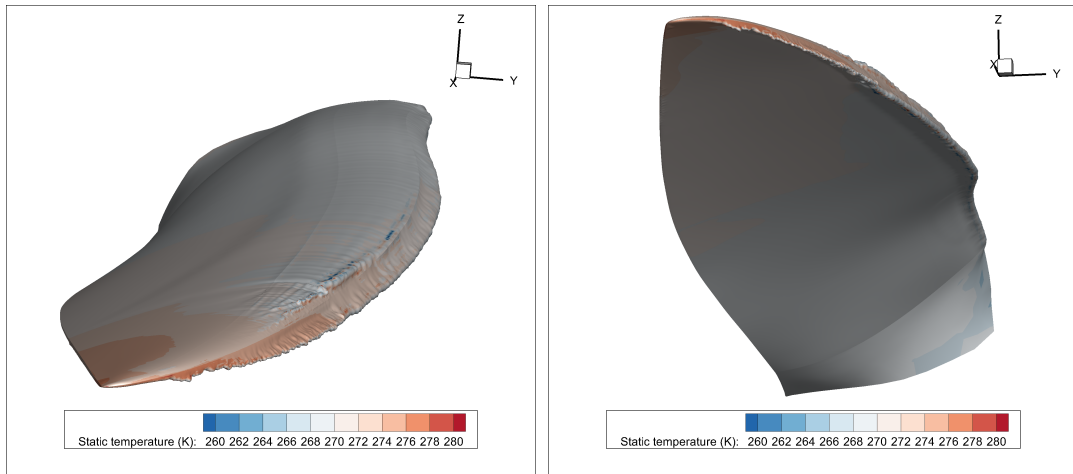
Figure C.11.: Surface temperatures on the ice shape at -5°C

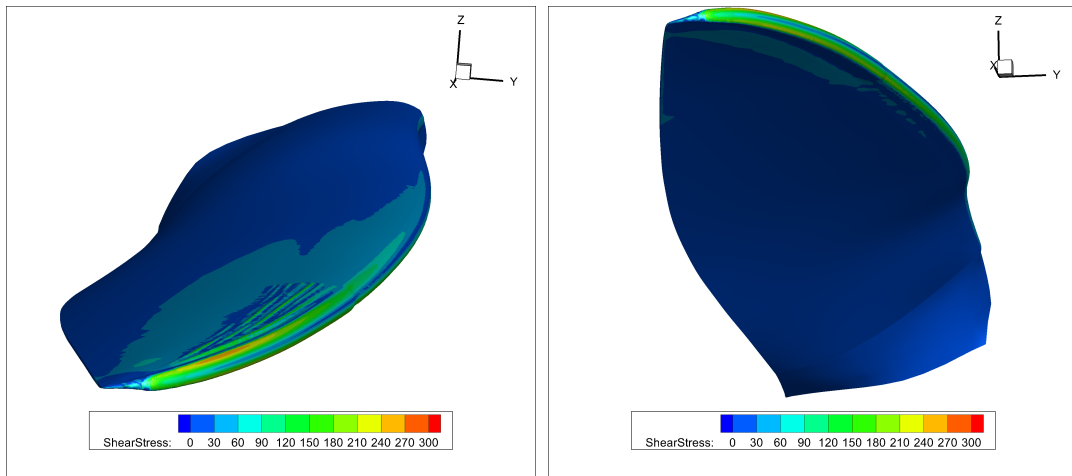**Figure C.12.:** Momentum in the z axis m_Z an the ice shape at -5°C.

R

C.4. Case 3

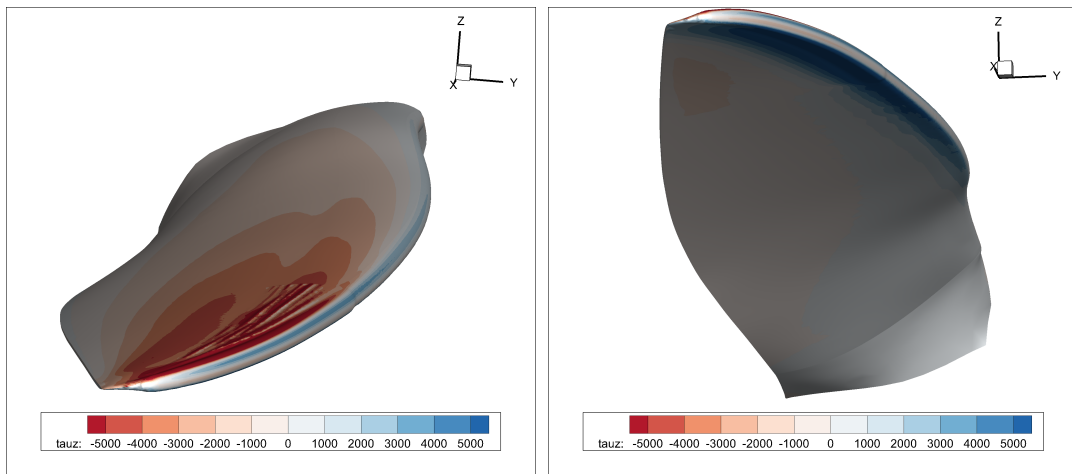**Figure C.13.:** Shear stress on the surface of the ice shape at -15°C.

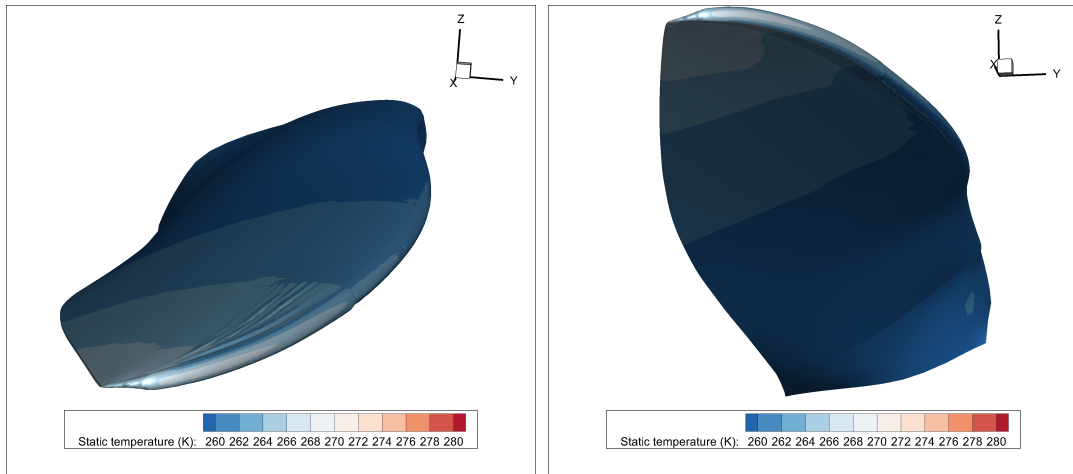**Figure C.14.:** Force in Z direction f_Z on the ice shape at -15°C.

S

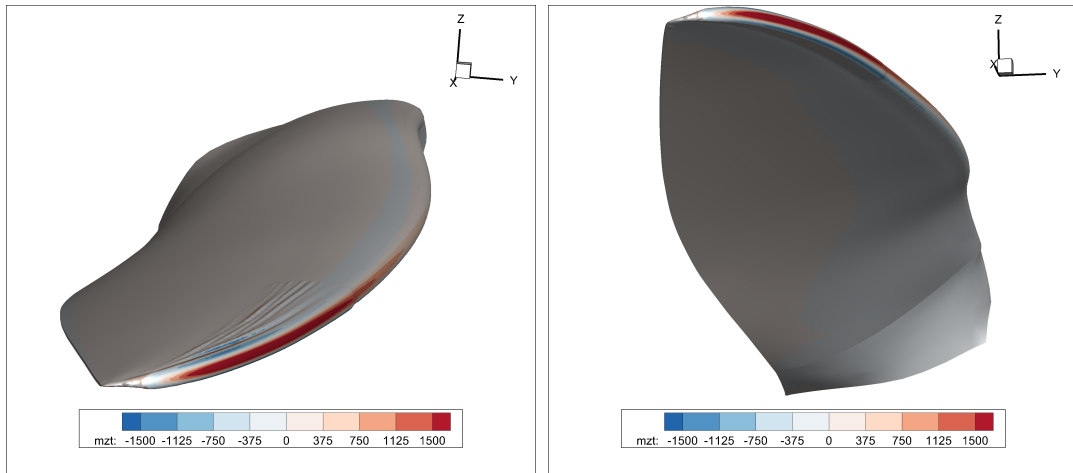**Figure C.15.:** Surface temperatures on the ice shape at -15°C.

Figure C.16.: Momentum in the z axis m_Z an the ice shape at -15°C.

T